PREPARATION AND CHARACTERIZATION OF SILICA NANOSPRINGS-SUPPORTED FISCHER-TROPSCH CATALYSTS FOR BIOFUEL PRODUCTION

A Dissertation

Presented in Partial Fulfillment of the Requirements for the

Degree of Doctor of Philosophy

with a

Major in Environmental Science/Renewable Materials

in the

College of Graduate Studies

University of Idaho

By

Abdulbaset. M. Alayat

Major Professor: Armando G. McDonald, Ph.D

Committee Members: David N. McIlroy, Ph.D.; Randall Brooks, Ph.D.; Dennis R. Becker, Ph.D.

Department Administrator: J.D. Wulfhorst, Ph.D.

May 2018

Authorization to Submit Dissertation

This dissertation of Abdulbaset. M. Alayat, submitted for the degree of Doctor of Philosophy with a major in Environmental Science and titled "Preparation and Characterization of Silica Nanosprings-Supported Fischer-Tropsch Catalysts for Biofuel Production," has been reviewed in final form. Permission, as indicated by the signatures and dated given below, is now granted to submit final copies to the College of Graduate Studies for approval.

Major Professor: ________________________________ Date: _____________
Armando G. McDonald, Ph.D.

Committee Members: ________________________________ Date: _____________
David N. McIlroy, Ph.D.

________________________________ Date: _____________
Randall Brooks, Ph.D.

________________________________ Date: _____________
Dennis R. Becker, Ph.D.

Department
Administrator: ________________________________ Date: _____________
J.D. Wulfhorst, Ph.D.

Abstract

This dissertation presents findings on the preparation and characterization of silica nanosprings (NS) supported Fe and Co catalysts for Fischer-Tropsch (FT) reactions. Silica NS with a high surface area of 400 m^2/g were chosen as a new 1-dimensional nanostructured support for Fe and Co based FT catalysts and divided into three sections. Section 1 involved the preparation and characterization of Co/NS catalysts as well as to examine the effects of two different reduction temperatures on the FT catalytic performance of this Co/NS catalyst. The prepared Co/NS catalysts were characterized before the FT reaction by various analytical techniques such as surface area, X-ray diffraction, transmission electron microscopy, energy dispersive X-ray spectroscopy, temperature programmed reduction (CO and H_2), X-ray photoelectron spectroscopy, fourier transform infrared spectroscopy and thermogravimetric analysis. The activity and selectivity of all catalysts were evaluated in a quartz fixed bed micro-reactor (H_2/CO of 2:1, 230-270 ^oC). The effect of reaction temperature on the catalytic performance of Co/NS catalyst was studied. The results showed that the catalyst reduced at a temperature of 609 ^oC had higher production rate of C_6-C_{17} hydrocarbons than the catalyst reduced at 409 ^oC. It also was found that the Co/NS catalyst resulted in more stability compared to with conventional catalysts.

Section 2 examined the effect of three preparation techniques (impregnation, precipitation and 2-step sol-gel) and activation conditions (H_2, CO or H_2+CO) on catalytic performance of these Fe/NS catalysts. It was found that the Fe/NS catalyst prepared by impregnation technique and activated with CO displayed the highest CO conversion (76.6%) and a wide distribution of light hydrocarbon (C_6 to C_{14}). Moreover, the XRD and XPS results of Fe/NS catalysts showed three different Fe crystalline phases with different particle sizes.

Section 3 examined the addition of Ru, Mo, Co and Cu as promoters on the Fe/NS catalysts. It was found that the promotion of the Fe catalyst supported on NS with Ru, Mo, Co and Cu increased the CO conversion, shifted the FTS product distributions and improved the selectivity towards C_6-C_{16} olefins instead of aromatics in unpromoted Fe/NS catalyst.

New types of Co and Fe catalysts were synthetized using silica nanosprings (NS) as a new 1-dimensional nanostructured support, and used in the Fischer-Tropsch synthesis. By using these catalysts, good activity, selectivity to C_6-C_{16} hydrocarbons (liquid fuels) and catalytic stability have been achieved. Furthermore, the incorporation of promoters, such as Ru, Mo, Co and Cu, into these catalysts can have effect leading to both high conversion and selectivity.

Acknowledgements

Alhamdulillah, first of all I would like to thank Allah for giving me strength and ability to complete this work. I would like to express my deep gratitude to my supervisor, Prof. Armando McDonald for his guidance, advice, motivation, encouragements and insight throughout my Ph.D. study and research. My thanks and appreciation goes to my thesis committee members, Drs. David McIlroy, Randy Brooks and Dennis. Becker for their continued participation and support, all of which I very much appreciate.

A special thanks to the Renewable Materials program, Department of Environmental Science, Department of Physic and Department of Chemical Engineering at the University of Idaho for providing some materials and analysis techniques used in this study.

My thanks to my mother (Fugra Alayat), my father (Emhamed Alayat), my uncle (Ali Alayat), my brothers(Muftah and Abdulmunem) and my sisters for their support and encouragement throughout the journey of my academic career in life. I also would like to thank Al jabal Al gharbi University and the Bob Stillinger fellowship for the financial support and giving me the opportunity to further my Ph.D. at the University of Idaho.

Last but not least, I would like to thank my wonderful wife, (Sana), my sons (Ali), (Hashem), (Mohamed) and my sweet daughter (Ragad) for their love, companionship, countless hours of care in good and bad time, in Libya and US. Thank you for always being there for me.

All the praise to Allah again.

Special Dedication

I like to dedicate this PhD work to my late mother, Fujra my late father, Emhamed and my late uncle Ali Alayat. I also dedicate this dissertation to my beloved family, wife Sana, sweet daughter Ragad, and sons Ali, Hashem and Mohamed for their endless pray, love, patience and support adhere for my academic and life. I thank you and I love you …

Abdulbaset Alayat

Table of Contents

List of Tables

List of Figures

INDEX

Abbreviations

ASF	Anderson-Schultz-Florey
BET	Brunauer, Emmet and Teller
BTL	Biomass to liquid process
CTL	Coal-to-liquid process
EDS	Energy Dispersive X-ray Spectrometry
FFB	Fixed fluidized bed reactor
FBR	Fixed bed reactor
FT	Fischer-Tropsch
FTIR	Fourier-transform infrared spectroscopy
FTS	Fischer-Tropsch synthesis
FWHM	Full width at half maximum
GC	Gas chromatograph
GC-MS	Gas chromatography mass spectrometer
GTL	Gas to Liquid process
HC	Hydrocarbons
HTFT	High temperature Fischer-Tropsch technology
JCPDS	Joint Committee on Powder Diffraction Standards
S_{BET}	The specific surface area
LTFT	Low temperature Fischer-Tropsch technology
LPG	liquefied petroleum gases
o/p	Olefin/Paraffin
SEM	Scanning electron microscopy
TCD	The thermal conductivity detector
TEM	Transmission electron microscopy

TGA	Thermogravimetric analysis
TPR	Temperature programmed reduction
WGS	Water-gas shift
XPS	X-ray photoelectron spectroscopic
XRD	X-Ray diffraction
Wt%	Weight percent (%)

Nomenclature

Co	Cobalt
CO	Carbon monoxide
CO_2	Carbon dioxide
Co_3O_4	Cobalt oxide
CH_4	Methane
Cu	Copper
Fe	Iron
FeO	Wüstite
Fe_3O_4	Magnetite
gHC	Gramme of hydrocarbons
GHSV	Gas hourly space velocity
H	Hydrogen
h	Hour
H_2/CO	the H_2/CO Ratio
H_2O	Water
KBr	Potassium bromide
n	Number of mole
N_A	Avogadros number

min	minute
Mo	Molybdenum
N_2	Nitrogen
Ni	Nickel
NS	Nanosprings
Ru	Ruthenium
SiO_2	Silica
syngas	Synthesis gas
t	Time
T	Temperature
X	Conversion in FT synthesis
X CO	Carbon monoxide conversion
XCO_2	Selective of carbon dioxide
X H_2	Hydrogen conversion
X CH_4	Selectivity of methane
SC_n	Selectivity of hydrogenation

Greek letters

α -Fe_2O_3	Hematite
γ-Fe_2O_3	Maghemite
α	Chain growth probability
β	line broadening at half the maximum intensity
λ	The average crystallite in nm
χ-Fe_5C_2	iron carbide
ΔH	Heat (enthalpy) of formation
Θ	The Bragg angle
θ-Fe_3C	iron carbide

CHAPTER 1: INTRODUCTION

1.1 History of Fischer-Tropsch Synthesis (FTS)

The Fischer- Tropsch (FT) process was first discovered in early 1923 by Franz Fischer (1877 - 1947) and Hans Tropsch (1889-1935) at the Kaiser Wilhelm Institute fur Kohlenforschung for Coal Research in Germany as a process to produce liquid transportation fuels prior and during World War II [1, 2]. At that time most of the research was conducted towards developing the FT process to produce fuels and chemicals from coal. By 1944, Germany's annual synthetic fuel production reached more than 124,000 barrels per day from 25 plants (approximately 6.5 million tons in 1944) [3]. Later Fischer-Tropsch synthesis (FTS) had grown as a promising alternative technology to produce alternative liquid fuel and feedstocks for the chemical industry from a mixture of CO and H_2 (synthesis gas or syngas), which is mostly derived from coal or natural gas, and it can also be produced from refinery residues, biomass or industrial gases. The first process (used to produce biofuel) was with Fe/ZnO and Co/Cr_2O_3 catalysts at relatively low temperatures and pressures [4]. The FT reaction is highly exothermic according to the following reaction:

$$CO + 2H \rightarrow \text{-CH}_2\text{-} + H2O \qquad \Delta H^\circ_{298} = -165\ kJ.\ mol^{-1} \qquad \text{(Eq.1-1)}$$

Where, methylene ($-CH_2-$) is the monomer building block of the FT reaction, which is produced in situ by reaction of CO and H_2 on the surface of a metal catalyst. The reaction above (Eq.1-1) is highly exothermic with a reaction enthalpy of 165 kJ.mol^{-1} converted CO.

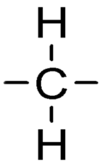

$$-CH_2-$$

1.2 Fischer-Tropsch Synthesis (FTS) Process

The first FTS commercial plant for the production of liquid hydrocarbons was inaugurated in 1936 in Germany and followed by plants in Japan, China, South Africa and the US after World II (~1940–1960) [5]. Due to South Africa having an abundance and low cost coal, the first commercial synthetic fuel plant from coal as the feedstock, called coal-to-liquids (CTL)-FT was (Sasol I plant) in 1955 in South Africa (~3,000 barrels per day (BPD)) [6]. In the late seventies and early eighties and after oil price increases dramatically, two new (CTL)-FT plants (Sasol II and III plants) were owned and operated by Sasol in South Africa. Over 90 years later the FT technology still sees great interest in the fuel and chemical industry with research and development to produce non-fossil fuels. Research is focused on improving FT efficiency to reduce its operating cost and the effects of fossil fuels on the environment [7]. In later years, Shell has also built major gas-to-liquids (GTL)-FT plants in Malaysia and Qatar using cobalt catalysts to make long-chain alkanes (Figures 1.1 and 1.2). Other small and large plants in South Africa, USA, China, Qatar and Malaysia are currently or have been involved in development of FTS technologies. Nowadays, there are many (GTL)-FT plants operating around the world, with main operations by Sasol in South Africa and by Shell in Malaysia and Qatar, Synfuels China and EGTL in Nigeria. Table 1-1, shows a summary of operating current commercial (GTL)-FT plants with their capacity for FTS across the world [5].

Figure 1.1. Shell's gas-to-liquids (GTL-FT) plant in Qatar. [www.shell.com].

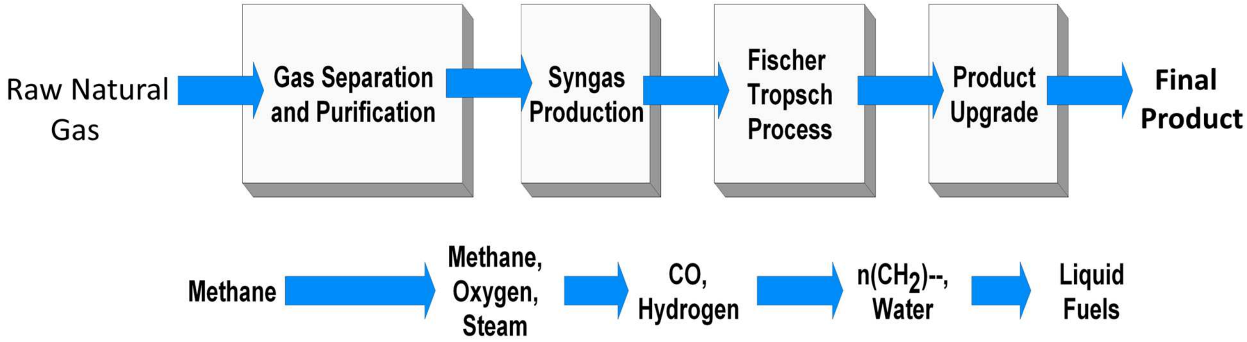

Figure 1.2. Schematic diagram of GTL production [Rahmim, 26th IAEE Annual International Conference Prague—June 2003]

Table 1.1. Fischer-Tropsch synthesis commercial plants across the world [8].

FT technology	Location	Carbon feedstock	Reactor/Catalyst utilized	Capacity (barrels/day)
Sasol	South Africa	Natural gas	Fixed bed (Fe/K)	5000
Sasol	South Africa	Coal & natural gas	Slurry (Fe/K)	160,000
ORYX GTL	Qatar	Natural gas	Slurry (Co/Al2O3)	34,000
EGTL	Nigeria	Natural gas	Slurry (Co/Al2O3)	34,000
Shell	Malaysia	Natural gas	Fixed bed (Co/SiO2, Co/TiO2)	14,500
Shell	Qatar	Natural gas	Fixed bed (Co/TiO2)	140,000
PetroSA	South Africa	Natural gas	Fe/K	22,000
Synfuels China	China	Coal	Fe/K	4000
Synfuels China	China	Coal	Fe/K	3200
Synfuels China	China	Coal	Fe/K	3200

1.3 Chemistry of Fischer-Tropsch Synthesis

FTS is still a promising alternative technology for catalytically converting mixtures of syngas (H_2 /CO in different ratios) derived from a variety of carbon sources, including biomass, coal and natural gas, to produce long-chained hydrocarbons, mainly alkanes (paraffins) and alkenes (olefins), which are used as clean transportation fuels and chemical products. Renewable fuels contain little contaminant compounds such as NO_x, CO, sulfur emissions and aromatic compounds [9]. The advantages of using biomass (wood, wood wastes, agricultural crops, municipal solid waste, animal wastes, algae, etc.) to convert into synthesis gas are their renewable character, thus yielding environmental fuels (Figure 1.3). The production of synthetic liquid fuels such as gasoline, diesel and jet fuel can be produced by various processes depending on the feedstock such as (GTL), (CTL) or biomass-to-liquid (BTL) [10]. In the BTL-FT processes, biomass, such as agricultural, forestry residues and wood is used to produce syngas by gasification with air, oxygen, and/or steam. However, syngas derived from biomass gasification contains CO, H_2, CO_2, CH_4, and N_2 in different proportions depending on the type of gasification process, gasification agent and the gasification temperature [11, 12]. In the upcoming years, sustainable energy from biomass derived carbon will be more feasible [13]. Coal and natural gas are currently a major source for industrial scale syngas. The GTL-FT technology plays an important role in industrial fuel production due to its lower sulfur dioxide, aromatic compounds and ability to reduce emissions of pollutants [14]. Additionally, natural gas (mainly methane) and coal are used as a primary feedstock to prepare a mixture of syngas (H_2/CO) to produce hydrocarbons by FTS. Since a major component of natural gas is methane and coal is rich in carbon, the partial oxidation (POX) or steam methane reforming (SMR) technologies are used to produce a syngas. [15, 16]. However, the GTL-FT technology can produce high quality diesel with a high cetane number of about >74, low sulfur content (≤ 1 ppm) and aromatics (<1%) [17]. In addition, the FTS can be operated at either low temperature (LTFT) or high-temperature (HTFT). The HTFT uses an iron (Fe) catalyst at around 350 ^{o}C with fluidized bed reactors to produce gasoline and linear low molecular mass olefins. Whereas, the LTFT process uses either an Fe or a cobalt (Co) catalyst at around 250 ^{o}C with either fixed bed or slurry phase reactors to produce heavy paraffinic hydrocarbons (wax) [18, 19]. The pressure can be either high (3 MPa) or low (0.1 MPa) depending on the type of catalyst used as well as the product desired [20]. Therefore, the distribution of FT hydrocarbons obtained from Co or Fe catalysts depend strongly on either the LTFT or HTFT used. For example, if the desired product is a liquid transportation fuel, such as gasoline, Fe-LTFT catalyst is the best possible choice due to the higher selectivity for light hydrocarbon (gasoline range). Table 1.2 shows the distribution of hydrocarbon products from Fe-LTFT, Fe-HTFT and Co-LTFT [21].

Table 1.1. FT product distribution in the LTFT and HTFT processes

Hydrocarbon products	**HTFT-Fe (Mass %)**	**LTFT-Fe (Mass %)**	**LTFT-Co (Mass %)**
C_1- methane	13	4	5
C_2	10	2	1
C_3-C_4 - LPG, olefins	25	8	5
C_5-C_{10} - naphtha/gasoline	33	12	20
C_{11}-C_{22} - distillate/diesel	7	20	22
C_{22}+ wax	3	50	45
Aqueous products	9	4	2
Paraffins (saturated hydrocarbons)	10	68	79
Olefins (unsaturated hydrocarbons)	53	20	12
Aromatics	3	Very low	Very low
Oxygenates	11	8	2

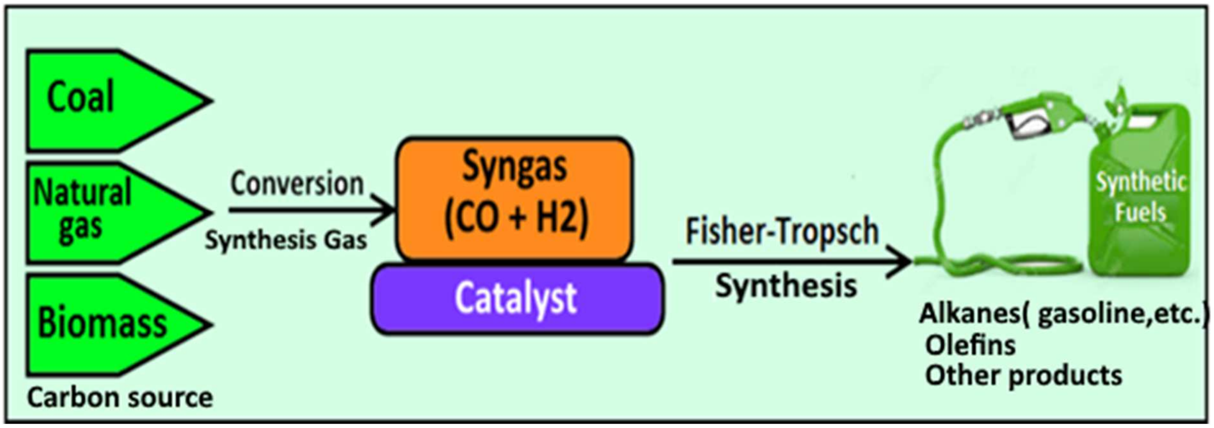

Figure 1.3. Schematic representation of Fischer-Tropsch catalysts for conversion of syngas derived from a variety of sources to produce biofuels.

The FTS is an exothermic surface polymerization reaction of CO hydrogenation adsorbed on heterogeneous catalysts to create the chain growth of products (Eq.1-1 and Figure 1.4) [10]. During nearly a century of FT mechanism studies, several mechanisms have been proposed to describe the FT reaction mechanism but it is still an issue of contention [22, 23]. Collectively, an overall FT reaction mechanism starts with the dissociation of CO and H_2 on open metal surface to form methylene (-CH_2-) species as the monomers in the polymerization process. The alkyl groups such as ethyl (4) or propyl (5) and the short and long chain hydrocarbon products that can be formed either undergo β-hydrogen abstraction to generate alkene products [e.g., ethylene or propylene] or by adding hydrogen to afford alkane products [e.g., ethane or propane] [24, 25]. In the following figure we will provide a brief review of some of the reaction pathways and mechanisms for hydrocarbon chain growth and chain termination in FTS.

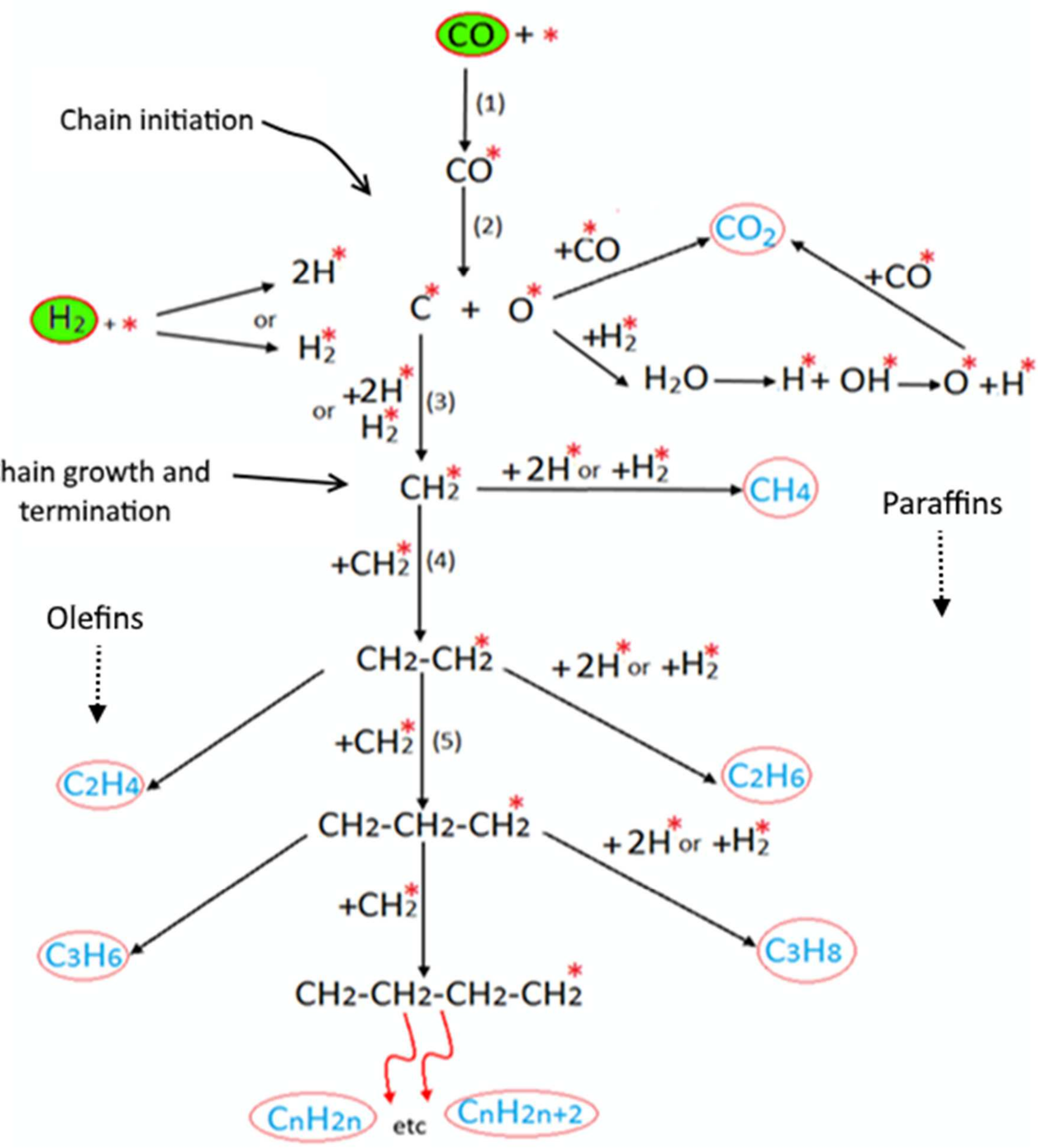

Figure 1.3. Simplified reaction mechanism as polymerization diagram for hydrocarbon chain growth and chain termination in Fisher –Tropsch synthesis[26, 27].

The hydrocarbon products created by the FT reaction consist of various hydrocarbon fractions depending on several factors, including type of catalyst, type of reactor, support, promoter and the FT reaction conditions (temperature, pressure) [28, 29].

However, when CO and H_2 (syngas) converted over a FT catalyst, the following reaction is generally formulated by FT reaction (n-paraffins) equation (1.2) [30, 31]:

Alkane (n-Paraffins) formation:

$$nCO + (2n+1)H_2 \rightarrow CnH_2n_{+2} + nH_2O \qquad \text{(Eq. 1-2)}$$

Where, n is the average carbon number. When n=, CnH_{2n+2}= (methane).

In addition to alkane (paraffins) formation reaction, there are other side reactions taking place in the FT process, among which the formation reaction of a wide range of alkene (olefins) and lesser amounts of some oxygenated products, such as alcohols and aldehydes in the case of Fe catalyzed FT reactions as follows by equation (1.3) and (1.4) [31]:

Alkene (olefin) formation:

$$nCO + 2nH_2 \rightarrow CnH_2n + nH_2O \qquad \text{(Eq. 1-3)}$$

Alcohol formation:

$$nCO + 2nH_2 \rightarrow CnH_2n{+}1OH + (n-1)\ H_2O \qquad \Delta H°298 < 0\ kJ.mol\text{-}1 \qquad \text{(Eq. 1-4)}$$

Another important reaction which takes place in FTS is the water gas shift reaction (WGSR), which is used to offset the loss of the H_2 to CO ratio when the ratio of H_2/CO is not available (< 2). The WGSR occurs during the FT process over Co and Fe catalysts that having high activity towards WGSR. However, Fe catalysts have higher WGSR activity than Co catalyst. The WGSR can be represented as follows by equation (4), which is valid over the temperature range 315–480 ^{o}C:[19]

$H_2O + CO \rightarrow H_2 + CO_2 \qquad \Delta H°_{298} = -41.8\ kJ.\ mol^{-1} \qquad \text{(Eq. 1-5)}$

Boudouard reaction (carbon deposition):

The Bouduard reaction is undesired as it produces CO_2 and coke; the latter covers the catalyst surface, leading to catalyst deactivation:

$2CO \rightarrow C + CO_2 \qquad \Delta H°_{298} = -171.5\ kJ.\ mol^{-1} \qquad \text{(Eq.1- 6)}$

Catalyst reduction and oxidation

$yH_2O + xM \Leftrightarrow MxOy + yH_2 \qquad \text{(Eq. 1-7)}$

$yCO_2 + xM \Leftrightarrow MxOy + yCO \qquad \text{(Eq. 1-8)}$

Coke formation

It has also been observed that the coke formation is likely to cause catalyst deactivation during FTS reaction as the following by equation (8):[4]

$H_2 + CO \rightarrow C + H_2O \qquad \Delta H°_{298} = -\ 132.6\ kJ.\ mol^{-1} \qquad \text{(Eq. 1-9)}$

1.4 FT Product distribution

A whole range of products fuels consists of various hydrocarbons of different lengths according to their boiling point, for example gasoline fraction (C_5-C_{11}), diesel fraction (C_{13}-C_{16}) and the liquefied petroleum gases (LPG) (C_1-C_4) which are the light hydrocarbons fraction of the paraffins. Most of hydrocarbons fuel in petroleum contain components that are gaseous C_1-C_4, liquids ranging from C_5 to C_{20}, and hydrocarbon chains above the C_{20} range are waxes (solid). FTS product distribution (gaseous and liquid) is dependent on type of catalyst (supported, unsupported), FTS operating conditions, and ranging from methane to high molecular weight waxes (C_1 - C_{60}) carbon atoms. The hydrocarbon type composition and names of the different fuels obtained from the petroleum refinery processes as are listed in Table 1.3 [32]. However, the controlling of product distribution is still the key technical problem in the FT process due to the sensitivity of FT reaction to many factors that can influence the hydrocarbon product distribution.

Table 1.3. Conventions of Fuel Names and their equivalent carbon chain lengths

Name	**Synonyms**	**Components**
Fuel Gas		C_1-C_2
LPG		C_3-C_4
Gasoline		C_5-C_{12}
Naphtha		C_8-C_{12}
Kerosene	Jet Fuel	C_{11}-C_{13}
Diesel	Fuel Oil	C_{13}-C_{17}
Middle Distillate	Light Oil	C_{10}-C_{20}
Soft Wax		C_{19}-C_{23}
Medium Wax		C_{24}-C_{35}
Hard Wax		C_{35+}

The product distributions of FTS depends not only on the selected catalyst but on the process operating conditions such as active metal, addition of promoter, support, catalyst preparation, reaction pressure, FT reaction temperature and syngas ratio[33].

Hydrocarbon distribution of the products from the FT process generally follows an Andersen-Schulz-Flory (ASF) equation, which is used for general polymerization reactions. Anderson was the first person to use this equation for FTS and expressed as

$$M_n = (1-\alpha)\,\alpha^{n-1} \qquad \text{(Eq. 1-10)}$$

Where, M_n is the molar fraction of a certain carbon number of n. FTS product distribution can be determined by the chain growth probability factor (α), as shown in Equation (1-11) below[34].

$$\alpha = \frac{Rp}{Rp+Rt} \qquad \text{(Eq. 1-11)}$$

Where, Rp and Rt are the rate of propagation and termination. Figure 1.6.displays the ASF distribution [35].The scheme presented in Figure 1.5 shows the relative probability of chain growth and termination reaction of the Anderson–Schulz–Flory equation [8, 36].

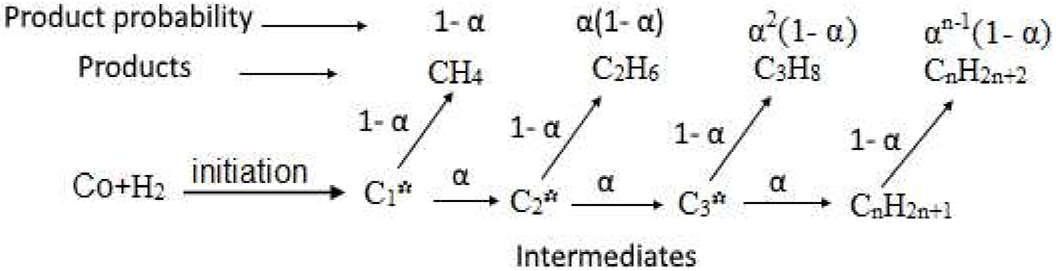

Figure 1.5. Carbon chain growth and termination scheme for the derivation of the Anderson–Schulz–Flory equation, with α the chain growth probability factor, C_n (n=1, 2, 3, etc.) the final products with n carbon atoms, and C_n* the intermediates with n carbon atoms.

Hence, the ASF distribution curve shows theoretical limits to the maximum possible yields of specific products. For example, the maximum yield is 100% weight for methane (n=1), about 45% by weight for gasoline (n=5-11) occurring at α = 0.75 and about 55% for diesel (n=12-18) occurring at α = 0.87 (Figure 1.6). The higher the α value, the higher the molecular weight of the product. The experimental results show that the ASF chain growth probability (α) can be effectively controlled by changing operating temperature, syngas composition, the ratio (CO:H_2) of syngas pressure, catalyst types, and presence of promoters [37, 38]. The effect of different temperature, pressure and H_2/CO ratio.

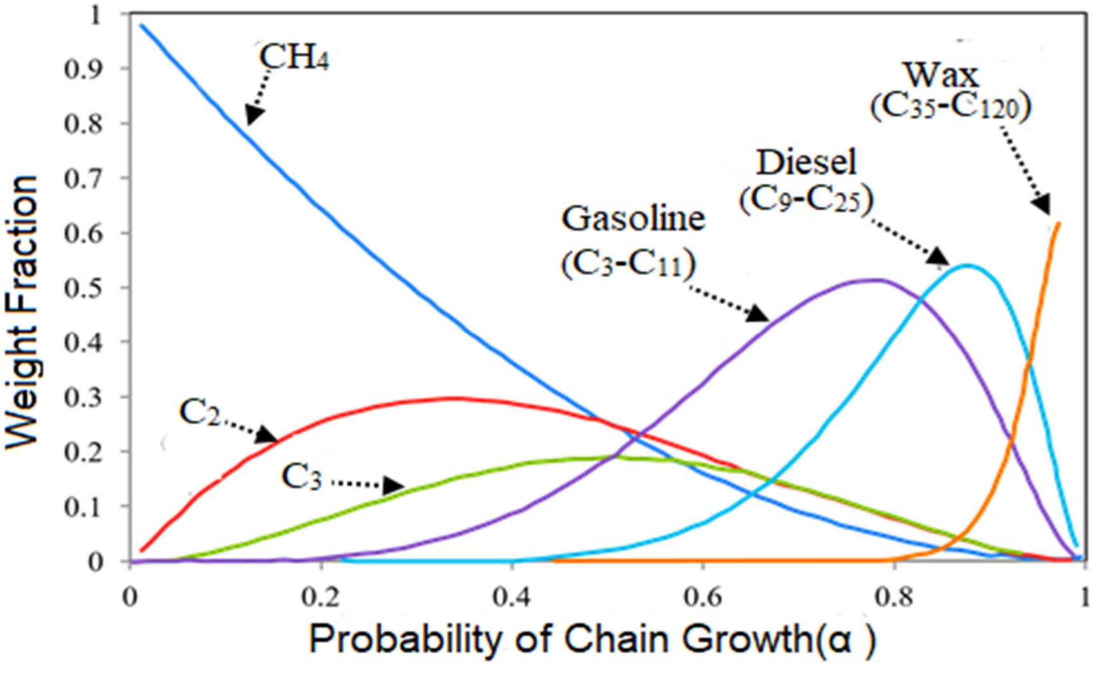

Figure 1.6. Anderson–Schulz–Flory distribution, showing FT product distribution as a function of chain growth probability (α).

1.5 Fischer-Tropsch catalysts

Catalysts have been the biggest success in the development and improvement of the commercial FTS process due to an increase in the rate of FT reaction and control the selectivity of hydrocarbons products. Typically, three different types of catalysts can be used in FTS reaction, including: (1) active component (bulk catalyst), (2) supported catalysts, (3) promoted catalysts. Figure 1.7 displays the three main parts of the FT catalysts. The oxides of transition metal (group VIII metals) are generally utilized as heterogeneous FTS catalysis to produce a wide distribution of hydrocarbons (fuels and chemicals) under typical reaction conditions. The most active FTS catalysts for carbon monoxide (CO) hydrogenation to hydrocarbons are ruthenium (Ru), Fe, Co and nickel (Ni) [39]. Despite Ru catalyst being the most active catalyst for producing higher molecular weight hydrocarbons, it is a precious metal with a high price and limited global supply, and therefore it is limited to research purpose in FTS. Moreover, Ru can also operate at low temperatures (<150 °C) as an active FT catalyst for CO hydrogenation, and without the need for any promoters [40][20]. Furthermore, Ru-based catalysts are also used in the FT technology to produce long chain hydrocarbons with low selectivity towards methane, and are very easy to reduce [41]. Commercially, the utilization of Ni as a FT catalyst become limited due to its high selectivity to methane, which is a not a desirable product in FTS [18, 41]. The choice of FTS catalyst is not a simple one as it is affected by several factors, such as the availability for large scale application, cost, activity, selectivity, feedstock for making syngas (i.e. the syngas H_2/CO ratio) and stability [8]. As a matter of fact, Fe and Co catalysts are the two most common industrial catalysts used in FTS due to their high activity, selectivity for FT and significantly lower cost and relative abundance [42, 43]. Due to the relatively high cost of Co, the Fe catalyst still has important uses as FT catalyst in liquid fuels production. In fact, Fe is a cheap catalyst and is, on average, 250 times less expensive than cobalt, and is 50,000 times less expensive than ruthenium (see Table1-4) [44, 45]. The relative activity for FTS catalysts was reported to decrease in the following order: Ru > Fe > Co > Ni > Rh > Pd > Pt > Ir [19, 46], and their order correspondent to activity in CO hydrogenation is displayed in Figure 1.8. Thus, only Ru, Fe, Co and Ni have good catalytic properties that allow considering them for commercial-scale production of renewable hydrocarbon biofuels. However, bimetallic iron/cobalt catalysts promoted with ruthenium have been shown to improve the properties of bimetallic catalysts[34]. However, generally due to the catalyst cost and technical challenges that that accompany some FT catalysts (i.e., Ru and Ni), iron and cobalt catalysts are still a viable option for the development of industrial FT catalysts.

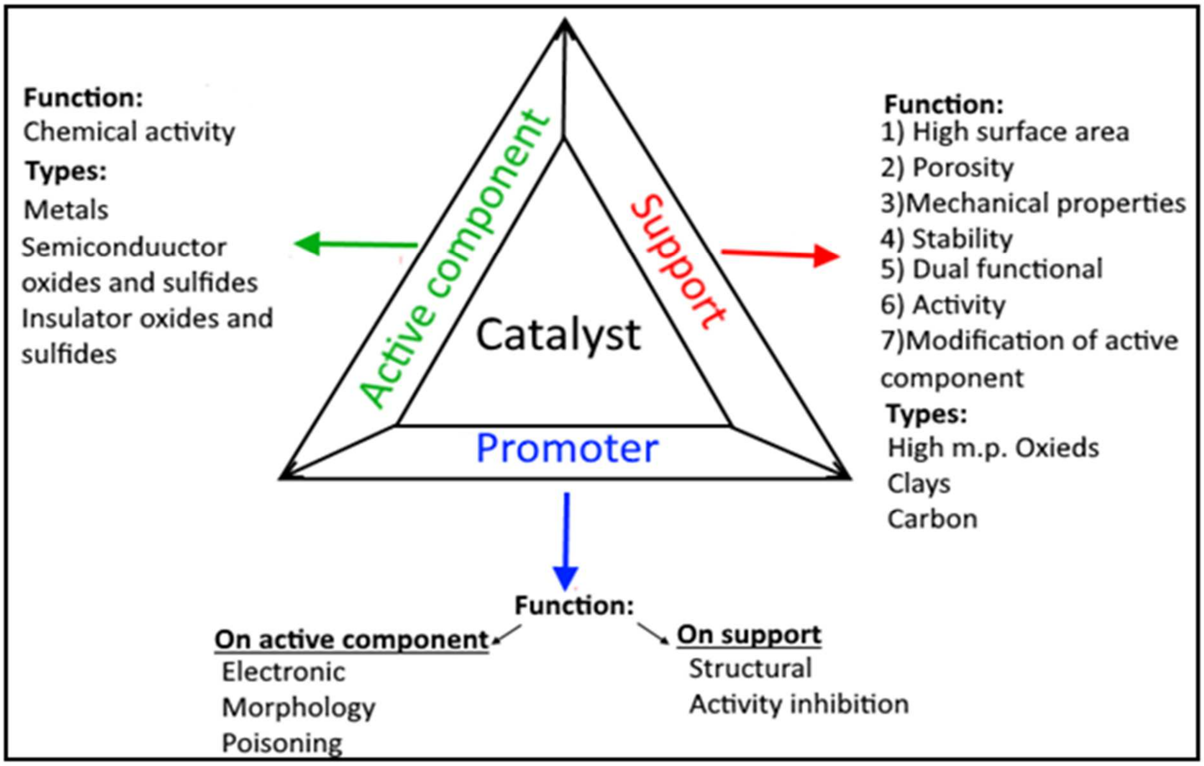

Figure 1.7. Three main parts of the catalyst [47].

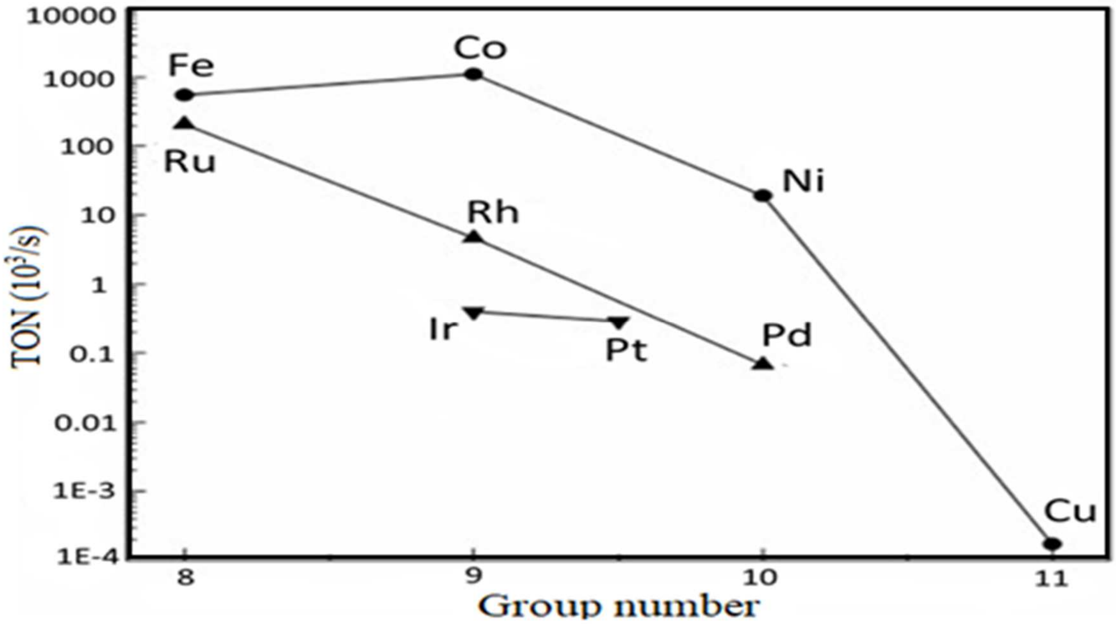

Figure 1.8. The activity order of various transition metals for CO hydrogenation [48].

Table 1.4. Comparative relative prices of different catalysts based on Fe [Exchange, L.M., London Metal Exchange. 2016].

Catalyst type	Price index	Price (US$ per ton)
Fe	1	42
Ni	250	8,450
Co	1000	22,600
Ru	50000	1,800,000

1.5.1 Cobalt catalyst

Cobalt based catalysts have been successfully applied to produce liquid hydrocarbon fuels since the 1923, giving the highest selectivity yields towards linear alkanes (paraffins) [4]. Although Co-based catalyst is not affect significantly the water gas shift reaction (WGSR), it is still plays a pivotal role in converting syngas to liquid fuel and chemicals, especially in the case when GTL technology based on natural gas feedstock is used for syngas generation with $H_2/CO = 2$, which is optimal for FT [49]. Previous studies have found that Co catalysts are active at LTFT (200-230 ^oC) to produce higher molecular weight hydrocarbons (diesel) and have a longer lifetime up to five years (time on stream) when compared to iron catalysts which have six months [32, 34]. Lifetimes of the cobalt catalyst may be due to its insusceptible to deactivation by carbide or oxide formation compared to Fe catalysts. However, Co catalysts are about three times more reactive than Fe catalysts in FTS [50]. Cobalt loading is always 10-40 % used in FTS, depending on the type support that is used. It has been shown that the optimal loading of Co on carbon nanotubes (CNTs) and mesoporous silica SBA-15 were 40% and 30%, respectively [33].

1.5.2 Iron catalyst

Historically, Fe based catalysts have been extensively used in industrial applications to convert syngas to liquid hydrocarbons since the discovery of the FTS in 1923 [4]. Fe-based catalysts are not only used because of their low cost and high natural abundance when compared to Co and Ru, but also exhibit more selectivity for olefin and gasoline range (C_5–C_{12}) and high activity for the water gas shift (WGS) reaction, which tends to re-equilibrate the H_2/CO ratio to the stoichiometric value needed for FT reaction [8]. The (WGS) is an important industrial process not only in the manufacture of hydrocarbon via FTS, but also in the industry to manufacture ammonia, methanol and H_2 [51]. The WGS makes Fe catalyst the choice for syngas obtained from biomass/coal gasification as feedstocks (hydrogen-poor) which has a low (H_2:CO = 1) [35, 37]. Fe catalysts can be used successfully for both LTFT and HTFT processes. HTFT processes with Fe catalysts are used to produce alkanes and low molecular weight alkenes, while LTFT processes are used to produce long chain hydrocarbons (diesel and linear waxes)[51]. A brief comparison of Co and Fe catalysts is given in Table 1.5 [26, 46].

Table 1.5. Comparison of Cobalt and Iron FT catalysts

Parameter	**Iron Catalyst**	**Cobalt Catalyst**
Cost	Less expensive	More expensive
Lifetime	Less resistant to deactivation (coking, carbon deposit, iron carbide)	Resistant to deactivation
Activity at low conversion	High	High
Productivity at high CO conversion	Lower, strong negative effect of water on the rate of carbon monoxide conversion	Higher, less significant effect of water on the rate of carbon monoxide conversion
Maximal chain growth probability	0.95	0.94
Water gas shift reaction	Significant	Not very significant; more noticeable at high conversion
$CO + H_2O \text{-->} CO_2 + H_2$		At high conversion
Maximal sulfur content	<0.2 ppm	<0.1 ppm
Flexibility (temperature and pressure)	Flexible; methane selectivity is relatively low even at 613 K	Less flexible; significant influence of temperature and pressure on hydrocarbon selectivity
H_2/CO ratio	0.5-2.5	~2
Attrition resistance	Not very resistant if not supported	Good (always supported)
Selectivity for olefins	Low	High
Selectivity for methane	Medium	Low

The active metals in the FTS catalysts are normally on a support to reduce the cost of metals and to maximize the metal dispersion (i.e. the active phase FT catalyst). Therefore, there is a need to minimize the amount of the metal used. Typical support materials generally are low cost and have high surface area, such as alumina (Al_2O_3), silica (SiO_2) and titania (TiO_2), to increase in the dispersion of the catalytic metals species [25]. Furthermore, promoters (e.g. Re, Rh, Pt and Pd) and oxide promoter (e.g. ZrO_2, MgO, MnO, La_2O_3, alkalis,etc) and are used to improve the activity, selectivity and stability [52].

1.6 Traditional FTS Catalyst Supports

The metal oxides and other support materials, which are stable materials with high surface area can play a major role in improving the FT catalytic performance, i.e., providing higher surface area to obtain high metal dispersion and reducing the cost of catalyst [53]. It also increases the number of active metal sites, decreases the deactivation rate and improve the product selectivity, reducibility and mechanical strength and thermal stability [23, 29, 54, 55]. The most popular conventional supports for the FT catalysts are SiO_2 (silica), TiO_2 (titania), Al_2O_3 (alumina) , MnO_2 (manganese dioxide) and ZrO_2 (zirconia) [56, 57]. Furthermore, various materials such as zeolites (e.g., HZSM-5 and SZ) [58, 59], mesoporous silica materials (e.g., MCM-41, FSM-16 and SBA-15) [60], nanoparticle supports (e.g., carbon nanofibers (CNFs) and carbon nanotubes (CNTs)) [61], have recently attracted considerable attention as potential supports in FTS catalysts due to their properties and ability to improve the performance of the FTS catalyst. Despite all the efforts so far to improve FT catalysts, these traditional supports still have some disadvantages. The addition of some these traditional supports to catalyst may react with metal catalyst/promoter, which leads to the formation oxide complexes such as silicates, aluminates and titanates causes an increase in temperature of reduction and influence activity, selectivity, and stability [34, 57]. This has been attributed to a strong interaction between oxide supports and catalytic metal particles [57, 62]. For instance, Al_2O_3 has a strong metal-support interaction with Co, TiO_2 has a moderate metal-support interaction with Co, and SiO_2 has a weak metal-support interaction with Co, which is why SiO_2 is often used in Co-based FT [62]. Although, SiO_2 is more easily modified than Al_2O_3 to have certain surface properties, it has poor hydrothermal stability at relatively low temperature. SiO_2 supports can form bulk cobalt silicate which are inactive in the FTS. In some cases, it is necessary to modify SiO_2 support by adding some stabilizers such as ZrO_2, TiO_2, CeO_2 or K [33]. Wherefore, these stabilizers have been used as Co-supports to try to control metal support interactions and the relative adsorptions of CO and H_2. In recent years, in order to overcome problems caused by the use of traditional supports, non-traditional one dimensional (1D) nano- structure supports such as: nanosprings, nanofibers, nanorods, nanotubes and nanobelts have been investigated as a promising new materials support for FT active catalysts based on their unique properties [63, 64].

1.7 Silica nanospring (NS) background

The use of metal nanoparticles oxides as supports for FT catalysts is a relatively new topic. Among these nanoparticles oxides, silica nanosprongs (NS) are a new family of 1D nanostructure materials, which can be can be synthesized on a large scale with low cost by using the vapor-liquid-solid (VLS) growth technique [63]. The surface structure and morphology of NS are shown in Figure 1.9.

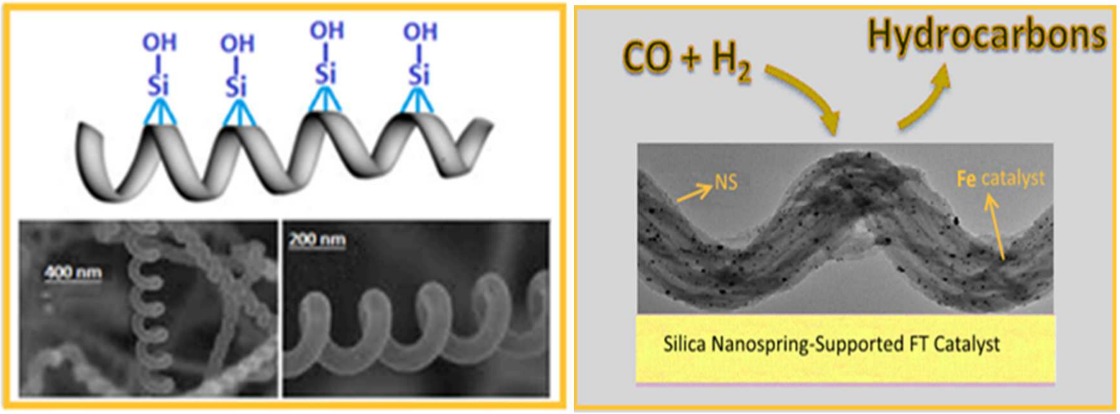

Figure 1. 4: The schematics illustration SEM and TEM micrographs of silica nanosprings.

NS are grown on a wide variety of substrates including glass, quartz, aluminum foil, stainless steel and even some high temperature plastics such as polyimide [24, 65], and this opens up the use of NS support for use in micro-reactors. In general, the NS process uses a thin gold layer (liquid) as a catalyst, which is sputtered onto aluminum foil substrate (solid), then exposed to constant flows of proprietary silicon precursor and O_2 in a N_2 atmosphere (vapors) during the deposition process. The conditions for

NS synthesis are modest at 350^{o}C and atmospheric pressure and this lends itself for large scale production [66].

NS have been used in various applications in nanotechnology including biological and chemical applications such as enzyme catalyst, biosensor applications, FTS and medium for hydrogen storage [63, 66, 67]. One of main advantages of using silica NS is the FTS catalyst supports application due to their corresponding with catalyst support criteria such as (i) high surface area (300 m^2/g), (ii) high thermal stability (up to 1000 ^{o}C), (iii) easy to grow, and (iv) can be grown in various surfaces [68]. NS are relatively new to FTS, thus there are three papers and chapters 2 and 3 reporting their use as catalyst. The first use of NS as a new high surface area support for Co-FTS catalyst was shown to produce hydrocarbons from the hydrogenation of CO as a proof of principal study [69]. A subsequent study showed that the Co-NS catalyst was not fully activated/reduced at 400^{o}C under H_2 prior to FTS evaluation and this was overcome by activating the Co-oxide at 609^{o}C, based on H_2-TPR and XPS studies, to improve CO conversion [70]. There are opportunities to improve the performance of these NS-FTS catalysts by selectively modifying the active metal particle size, using promoters to enhance their activity, and characterize their properties.

1.8 Fischer -Tropsch Reactors

There are basically three types of commercial reactors employed for FTS: the tubular fixed bed reactor (TFBR), fluidized bed reactor (FBR), and slurry phase reactor (SPR). Schematic of each type of reactor is presented in Figure 1.10. The first commercial use of tubular fixed bed reactor (TFBR) was at SASOL I in 1955s [21]. Each of these reactors is employed to produce a certain type of products and has its own advantages and disadvantages, and can be considered as nono-ptimal performance in commercial FT operation. Therefore, the reactors used should be designed with sufficient heat transfer area to avoid undesirable side-products like carbon monoxide, methane, light hydrocarbons, coking and sintering due to the high amount of heat (approximately 60,000 kJ/kmol of syngas) generated from the exothermic FT synthesis reactions [49, 52]. Thus, the designing of FT reactors need a lot of experience and long-period small test before the industrialization. However, there are two commercial FT processes, LTFT and HTFT. The slurry phase reactor (SPR) is one of the earliest FT reactor designs and has been used since the1950s [21] . Both SPR and tubular fixed bed reactor (TFBR) are usually used for LTFT (220 -250 ^{o}C) with either Fe or Co catalysts to produce chain hydrocarbons (e.g., middle distillates, gasoline, diesel and heavy waxes).The operating pressure in the LTFT is in the range of 2.0 -2.5 MPa, and the conversion is about 60% [71]. The SPR and TFBR reactors are a three phase reactor with a gas phase (gaseous reactants), solid phase (wax products and catalyst particles) and liquid phase (liquid products). Fluidized bed reactor (FBR) which also named as Synthol reactor was first developed and commercially used in the 1950s by Sasol [21]. They operated at a temperature (HTFT) (320-350 ^{o}C) with Fe catalyst to produce gasoline and linear, low molecular mass olefins. The operating pressure in HTFT is about 2.5MPa, and the conversion is more than 85% [71]. The key difference between HTFT and LTFT reactors is the absence of liquid phase in the HTFT reactors outside the catalyst bed, and any wax or liquid phase products deposits on the catalyst may cause potential problems such as catalyst solid agglomeration and a loss of fluidization[37]. There are two types of fluidized bed HTFT reactors: circulating-fluidized-bed reactors (CFB) and Fixed-Fluidized-Bed Reactors (FFB). The distinguishing feature between the two types of reactors is that these reactors can only be used with Fe based catalysts only for the production of gasoline and diesel fuels, and they cannot be used for higher hydrocarbon formation primarily due to the agglomeration of the catalyst in the presence of waxy products that can result to de-fluidization [49]. The selection of FT reactor type will depend on the desired final products (e.g. chemicals, gasoline, diesel, or jet fuel), the reaction temperature range, the purity chemical of the syngas and other economic reasons [9, 72]. Comparisons were made between SPR, FBR and TFBR reactors and summarized in Table 1.6.

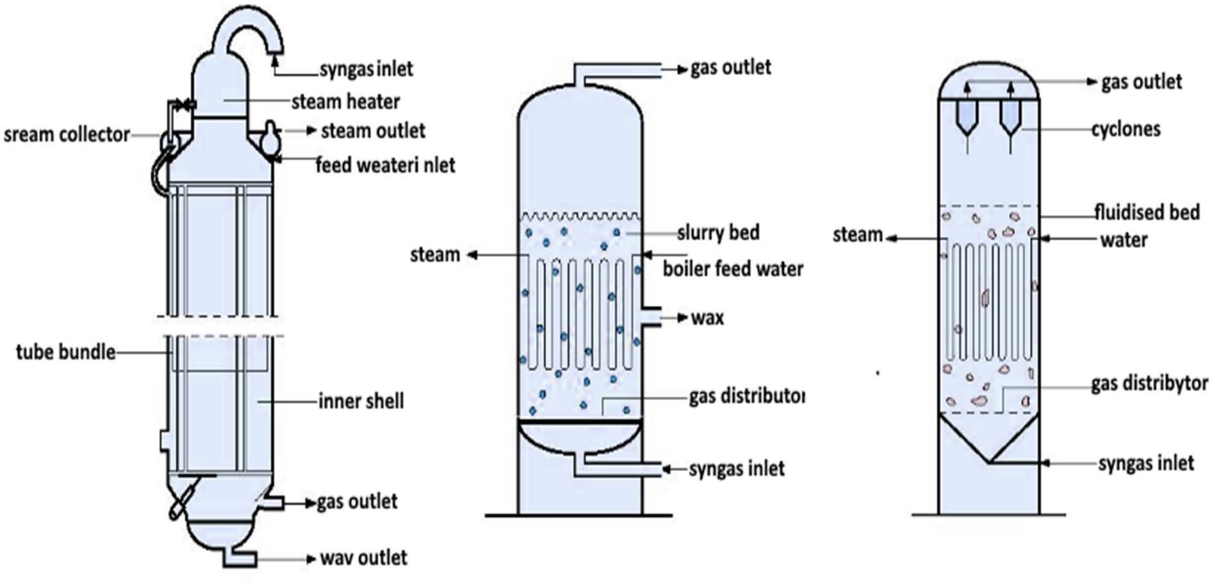

Figure 1.10. Schematic of a tubular fixed bed (left), a slurry phase (middle), and a fluidized bed (right) FT reactor [8, 73].

Table 1.6. Summary of cited parameter of FT reactors (Fe catalyst)

Parameter	**Fixed bed**	**Fluidized bed**	**Slurry phase**
Operation	Simple	Complex	Intermediate
Temperature control	Poor	Good	Good
Reaction phase	G or G+L	G	G+L
Catalyst type	Fe/Co	Fe	Co/F
Catalyst size	1-3 mm	40-150 μm	10-150 μm
Heat exchanger	240m^2 per 1000m^3	15-30m^2 per 2000m^3	50m^2 per 1000m^3
Surface	feed	feed	feed
Max. reactor size	<80mm	large	large
CH_4 formation	low	high	as fixed bed or lower
Flexibility	high	little	intermediate
Product	full range	low mol. Weight	full range
Space-time yield(C2+)	>1000kg/m3 day	4000-12000kg/m3 day	1000kg/m3 day
Catalyst affectivity	lowest	highest	intermediate
Back mixing	little	intermediate	large
Minimum H_2/CO feed	as slurry or higher (1.7-1.8)	Highest (2.5-3)	Lowest ($\geq$ 0.7)
Pressure (bar)	27	22	15
Inlet T (K)	496	593	533
Outlet T (K)	509	598	538

1.9 Promoters for Fischer –Tropsch Synthesis

For further improvement of FT process through the catalyst promoters (alkalis, noble metals, and metal oxides) are often incorporated into the catalyst structure to increase the rate of catalyst activation and retain stability over time [51]. Promoters are small amount of a substance which comprises transition metals and elements from groups IA–VIIIA that enhance the activity, the reduction, selectivity, lifetime and stability of the catalyst [34, 48]. However, researchers have been classified promoters depending on their effect: structural or structure promoters, electronic promoters, textural promoters, stabilizers and catalyst-poison-resistant promoters [74]. Promoter elements such as K ,B ,Mg, Ti, V, Cr, Mn, Zr, Mo, LA, Ce, Gd and Th have been widely applied as electronic promoters to enhance the activity, selectivity and stability of Co catalysts [75]. This is due to the fact that promoters can donate their electrons to the metal enhancing dissociation of CO, metal/carbide phase formation and lowering H/C surface concentration. Copper has also been used as a promoter in iron FT catalysts. Cu promotion affects the reduction of Fe catalyst, hydrocarbon selectivity, product distribution to diesel and slightly increases the selectivity towards alcohols and oxygenates [76]. On the contrary, it is also noted that alkali promoters in some cases can lead to decreased activity [33].

Metals such as Cu, Ru, and Mo are typically added as promoters in order to enhance the catalytic performance of Fe catalyst. Other promoters such as Zn and Mg have other advantages and can produce a different hydrocarbons product range [77]. Numerous studies have shown that Ru has a strong effect on the structure and dispersion of cobalt catalyst, FT reaction, selectivities and deactivation [48].

1.10 Catalyst Preparation

There are several different preparation techniques are used for preparation of supported catalysts and each catalyst may be produced via different methods. Some of the common traditional methods are: incipient wetness impregnation, precipitation and sol-gel (solution-gelation) methods [62].In all these preparation methods, a metal precursor, mostly an inorganic salt (nitrates, chlorides, citrates, etc.) because of the dispersion of inorganic salts provide metal dispersion onto the support [78]. This variety of different preparation methods are important for FT catalysts as they can greatly effect on their catalytic properties such as the structure of the active metal dispersion, the interactions of the promoters with the active phase and/or, the support, and the dispersion of the active metal, all of which can influence the catalytic activity and selectivity [33]. The incipient wetness impregnation method is a commonly used method for preparing Co and Fe catalysts. This method involves three main steps: (i) impregnating metal solution with support, (ii) drying to remove the imbibed liquid and (iii) using the calcination and activation methods to remove the residual organic solvents [79]. The precipitation method is used for preparation of bulk catalysts (unsupported) and supported catalysts. Whereas, Co-precipitation method is used for simultaneous precipitation of more than one metal (bimetallic catalysts). Moreover, precipitation method involves two distinct steps: (i) nucleation and (ii) growth. The nucleation is the first step of the formation of solid partials phase and the precipitation will begin. The growth process depends on precipitation conditions such as concentration, temperature, pH and ripening. Then crystal growth continues until the formation of solid precursor of the active metal and support as primary products [78, 79]. The reaction process in precipitation method can be simplified as the following:

$$\underset{\text{(nitrates, chlorides, citrates, etc.)}}{\text{Metal Salt Soiution}} + \text{Support} \xrightarrow[\text{(NaOH, KOH,etc.)}]{} \text{Metal htdroxide on support}$$

(Eq. 1-12)

Also sol-gel preparation methods have been successfully used to prepare supported FT catalysts. I this technique, supported FT catalysts can be prepared from a homogeneous solution containing both the metal precursor in the organic solvent and the support followed by formation of a gel. Furthermore, the sol-gel transformation, which is a solid matrix encapsulating a solvent, needs to be dried to remove the remaining liquid (solvent) phase [80]. The chemical reactions of sol-gel polymerization can be simplified as the following [81]:

$$\text{M-O-R} + H_2O \xrightarrow{H^+ \text{ or } OH^-} \text{M-OH} + \text{ROH} \quad \text{(hydrolysis)}$$

$$\text{M-OH} + \text{XO-M} \xrightarrow{H^+ \text{ or } OH^-} \text{M-O-M} + \text{XOH} \quad \text{(condensation)} \qquad \text{(Eq. 1-13)}$$

The support, precursor/solvent pairing, drying, calcinations, and reduction conditions are necessary and required to control the catalytic properties of catalyst prepared such as metal-support interactions and phase composition [33]. Figure 1.11 is a simplified diagram which summarizes the traditional methods as example used in this study for the preparation of FT catalysts (Fe/NS catalysts).

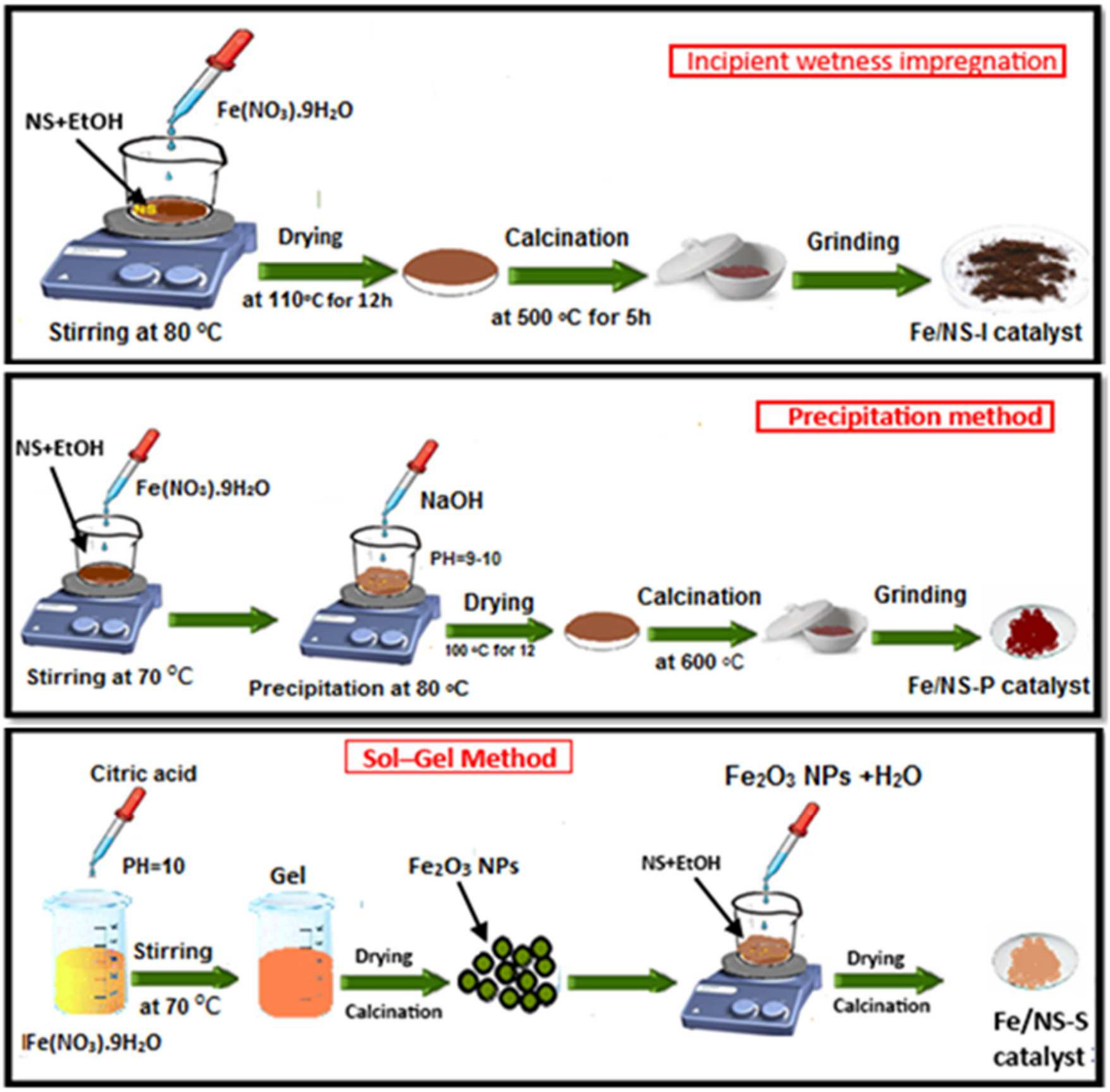

Figure 1.11. Simplified diagram summarizing Fe/NS catalyst preparation with different methods

1.11 Fischer–Tropsch Catalyst Deactivation

Unfortunately, FTS catalysts, like all other heterogeneous catalysts, lose catalytic activity and/or selectivity over time. Catalyst deactivation is one of the great challenges in FT industry that causes loss of catalytic activity (productivity) and lifetime, thereby increasing the cost FT industry because of catalyst replacement. However, causes of FT catalyst deactivation may depend on some the factors, such as the nature and properties of the catalyst, e.g., support, promoters, dispersion, reduction, type of reactor and operating conditions [82] The loss of catalytic activity due to chemical , mechanical or thermal processes that may occur separately or in combination, leading to the loss of active sites on the catalyst's surface. Results of previous review on FT catalyst deactivation have shown that there are many possible mechanisms suggested for FT catalyst deactivation; nevertheless, they can be grounded into six intrinsic mechanisms: (i) poisoning by sulfur and nitrogen, (ii) re-oxidation, (iii) fouling, (iv) thermal degradation and (v) chemical reaction and phase transformations (vi) mechanical degradation [83, 84]. Schematic of each type of deactivation phenomena inside a catalyst particle is presented in Figure 1.12, and each of the six intrinsic mechanisms is defined briefly in Table 1.7.

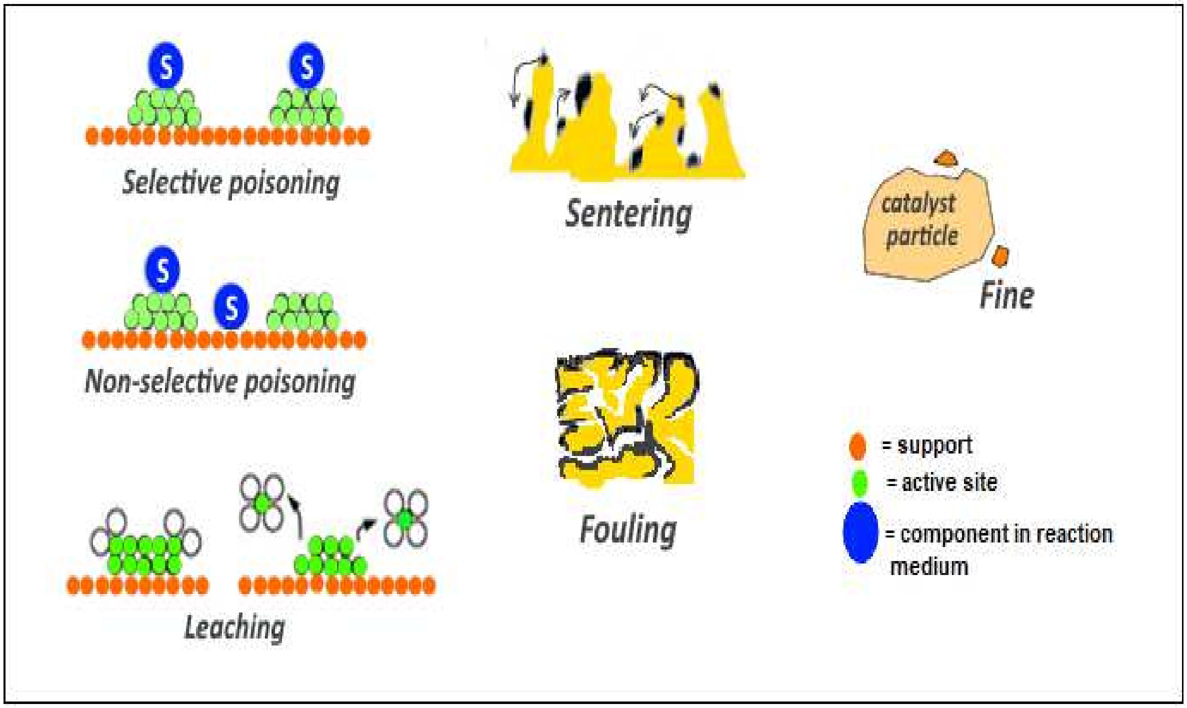

Figure 1.12. A simplified schematic to demonstrate the major types of deactivation in heterogeneous catalysis [85]

Table 1.7. Mechanisms of catalyst deactivation [84].

Mechanism	Deactivation types	Brief definition /description
Poisoning	Chemical	A strong chemisorption of species(reactants, products, or impurities e.g., sulfur and nitrogen) on catalytic sites that inhibit catalytic interaction sites
Fouling	Mechanical	Physical deposition of species from fluid phase (waxes or carbon deposition) onto the catalytic surface and in catalyst pore which inhibit adsorption and slow down diffusion rate
Thermal degradation and sintering	Thermal Thermal/chemical	Thermally can either be by sintering (loss of catalytic surface area and support area) or by the chemical transformation of catalytically active phases to inactive phases
Mechanical degradation	Mechanical	Mechanical degradation of the catalyst particle due to attrition; loss of internal surface area due to mechanical-induced crushing of the catalyst particle
Chemical reaction and phase transformations	Chemical	Chemical reaction and phase transformations can either be by reaction of gas with catalyst phase to produce volatile compound or reaction of vapor, support material, or promoter with catalytic phase to produce inactive phase
Re-oxidation	Chemical	Active iron carbide phase (ε-Fe2C, έ-Fe2.2C and χ-Fe2.5C) can change to a more stable carbide phase (θ-Fe3C) or can be re-oxidized to form Fe3O4

1.12 Catalyst Activation

The iron and cobalt catalysts prepared actually exist in inactive oxide phases as Fe_2O_3 and Co_3O_4 on the surface of calcined catalysts, thus requiring reduction prior to the FT reaction by reducing agents (typically using hydrogen, carbon monoxide or syngas), as they both need to be reduced to generate a high metallic surface (α-Fe or Co) with H_2 or iron carbide (χ-Fe_5C_2) phases with CO or syngas, which are considered the active phases for FTS. Catalyst activation with H_2, CO or syngas often have significant effects on catalytic properties and selectivity for Fe-based catalysts. A Co catalyst is usually reduced by H_2 to metallic cobalt which is believed to be the active phase for FTS in these catalysts[50]. However, several iron phases exist on the surface of the catalyst in FTS, including Fe_2O_3, Fe_3O_4 and O-carbides (Fe_xC_y) [86]. In addition, the reduction conditions of FT catalyst influence on its activity and selectivity. Iron has three oxides, namely hematite (Fe_2O_3), magnetite (Fe_3O_4), and wustite (FeO). The iron and cobalt oxides reduced to α-Fe with and Co metal, respectively as shown in the following reaction:

Reduction of iron catalyst with H_2: the iron catalysts (Fe_2O_3) are always reduced to magnetite Fe_3O_4 at first and then to metallic iron:

The first stage reduction: $3Fe_2O_3 + H_2 \rightarrow 2Fe_3O_4 + H_2O$ (Eq. 1-14)

The second stage reduction: $Fe_3O_4 + H_2 \rightarrow 2FeO + H_2O$ (Eq. 1-15)

The third stage reduction: $FeO + H_2 \rightarrow Fe + H_2O$ (Eq. 1-16)

Overall reaction: $Fe_2O_3 + 3H_2 \rightarrow 2\ Fe + 3H_2O$ (Eq. 1-17)

Reduction of cobalt catalyst with H_2:

The first stage reduction: $Co_3O_4 + H_2 \rightarrow 3CoO + H_2O$ (Eq. 1-18)

The second stage reduction: $CoO + 2H_2 \rightarrow Co + 2H_2O$ (Eq. 1-19)

Reduction of iron catalyst with CO [87]:

$$3Fe_2O_3 + CO \rightarrow 2Fe_3O_4 + CO_2 \qquad \text{(Eq. 1-20)}$$

Fe_3O_4 is then carburized to form ε-Fe_2C, έ-$Fe_{2.2}C$, χ-$Fe_{2.5}C$ and CO_2

Carburizing reactions: $Fe_xO + 2CO \rightarrow Fe_xC + CO_2$ (Eq. 1-21)

Several studies have reported that the CO activated iron catalysts showed a higher initial activity than the H2 and syngas activated catalysts [88]. Figure 1.13 shows the schematic summary of the activation of iron and cobalt oxides using H_2 or CO.

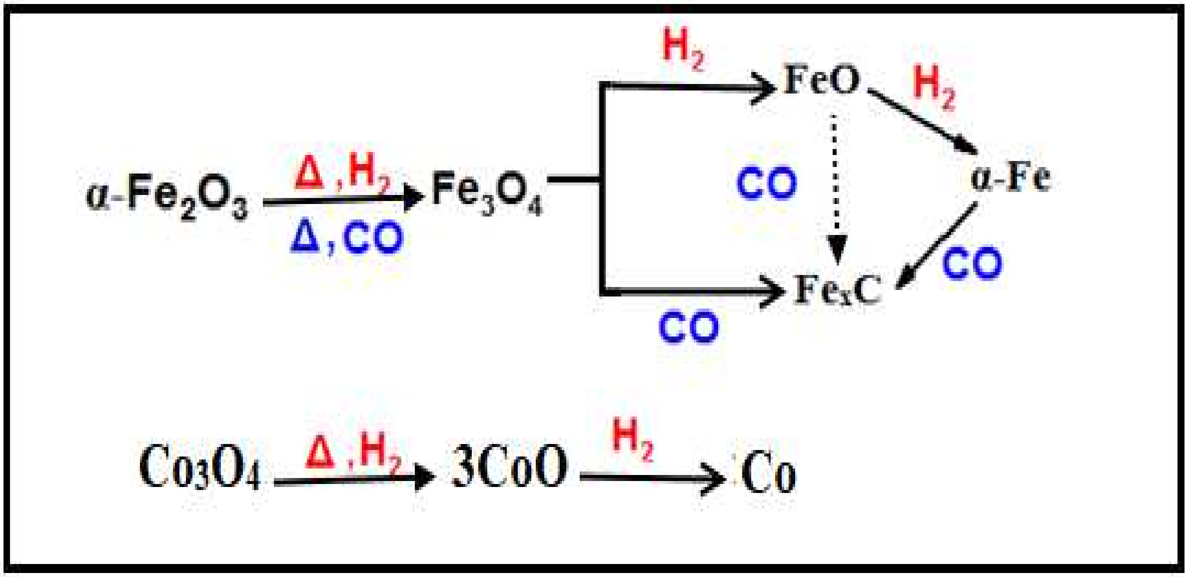

Figure 1.5. Schematic illustration of the activation of iron oxides using H_2 or CO.

1.13 Project Aims

This dissertation is focused on assessing new catalysts on NS supports for producing hydrocarbons by FTS. The major aim of this work is to prepare, characterize and evaluate the physicochemical properties of silica nanospring (NS) as a new support for Fe and Co (FT) catalysts for biofuel production, combined with the use of promoters (i.e. Cu, Mo and Ru addition). Silica NS were chosen in this study as a new nanostructured support for FTS due to their unique properties (accessible surface, large surface area, etc.) that qualify them as good support for FT catalysts. These catalysts were also characterized before the FT reaction by several techniques in order to draw meaningful correlations between physicochemical properties of Fe and/or Co catalysts with silica NS.

The project goals are to develop catalysts for FTS that have improved performance through the following research questions:

1. Will the reduction temperature have a significant influence on the activity and selectivity of silica NS -supported cobalt catalyst for FTS?
2. Will the FT process parameters such as synthesis and activation methods have significant influence on the activity and selectivity of silica NS-supported iron catalyst for FTS?
3. Will the addition of Cu, Mo, Co and Ru promoters to silica NS-supported iron catalyst improve their CO conversion and selectivity during FTS?

1.14 Outline of the Dissertation

This dissertation focuses on understanding the physicochemical properties of Co/NS and Fe/NS catalysts for FTS. It is divided into four main chapters, as follows:

- Chapter 1 introduces the process of FTS as an alternative technic towards cleaner liquid fuels and chemicals from alternative feedstocks, and the pertinent literature on FT catalysts, reactors, supports, FT promoters, etc. Provide the project aims and the methodology to achieve them.
- Chapter 2 is the experimental chapter which discusses the synthesis of silica NS as a new support in cobalt catalyst for FTS. Structure and catalytic performance of Co/NS catalyst were investigated and compared to the conventional Co/SiO_2 catalyst with hydrogen reduction at two different temperatures.
- Chapter 3 deals with a study on the effect of synthesis method and activation conditions on catalytic performance of 1D Fe/NS catalysts for FTS. This is achieved using three different preparation techniques (incipient wetness impregnation, precipitation and modified sol-gel) and H_2, CO and H_2/CO as activation agents in FTS.
- Chapter 4 focuses on the enhancement of the catalytic performance of Fe/NS catalyst with the addition of promoters such as copper, molybdenum, cobalt and ruthenium for FTS.

- Chapter 5 summarizes briefly results and conclusions obtained for the individual chapters, along with perspectives for future works. Appendices are then annexed to provide further details, additional results and supplementary information.
- Finally, all obtained results are prepared in a journal article format for three papers and presented in Chapters 2, 3, and 4.

CHAPTER 2: EFFECT OF REDUCTION TEMPERATURE ON THE ACTIVIYT AND SEIECTIVITY OF SILICA NANOSPRING (SN)-SUPPORTED COBALT CATALYST FOR FISCHER-TROPSCH SYNTHESIS

2.1 Abstract

The Co/NS catalyst was prepared using incipient wetness impregnation method and reduced by H_2 at low (409 ^{o}C) and high temperature (609 ^{o}C) for 24h. The catalytic performance of Co/NS catalyst was evaluated in a quartz fixed-bed micro-reactor (H_2/CO of 2:1, 230 ^{o}C) and the products trapped and analyzed by GC-TCD and GC-MS to determine CO conversion and reaction selectivity. The prepared Co/NS catalyst was characterized before the FT reaction by BET surface area, X-ray diffraction (XRD), transmission electron microscopy (TEM), temperature programmed reduction (TPR), X-ray photoelectron spectroscopy (XPS) and thermogravimetric analysis (TGA) in order to find correlations between physico-chemical properties of catalysts and catalytic performance. The results showed that the catalyst reduced at a temperature of 609 ^{o}C had higher production rate of C_6-C_{17} hydrocarbons than the catalyst reduced at 409 ^{o}C.

2.2 Introduction

Fischer-Tropsch synthesis (FTS) is a heterogeneous catalytic reaction for conversion of syngas (CO, H_2) into liquid hydrocarbons (fuels) and other valuable chemicals[9]. Several metals, such as ruthenium (Ru), iron (Fe), nickel (Ni), Co, rhodium (Rh), palladium (Pd), and platinum (Pt) have been demonstrated to be effective catalysts for the FTS process. From an economic standpoint, Fe and Co catalysts are the most viable FTS catalysts [44]. The choice of Fe or Co depends on the desired operating conditions and products of the FTS process. Generally, Co catalysts are used only at low temperatures (200–240 °C) because at high temperatures a significant amount of methane is produced [89]. Low temperature FTS yields high molecular weight linear hydrocarbons, while high temperatures (300–350 °C) produce gasoline and low molecular weight olefins. If maximizing the gasoline product fraction is desired, then it is best to use Fe catalyst at high temperature. However, if maximizing diesel product fraction is preferred, then Co catalyst is once again the best choice [89]. FTS product selectivity depends on the reaction conditions, on the promoter, or on the nature of the support. While FTS performances of Fe based catalyst are improved by the addition of promoters, those of Co catalysts are not very sensitive to promoters. Moreover, Co catalysts lead to the formation of water and not CO_2 (a loss of carbon from the process) and their carburization is low compared to that of Fe based catalysts [90]. While Co is orders of magnitude more expensive than Fe, it is still a viable alternative to Fe because its demonstrated activity at lower synthesis pressures, reduces operating costs, thereby offsetting its higher cost [89].

Due to the cost of Co, the Co metal is generally accepted to be the active phase during FTS [46] and is dispersed onto a support in order to reduce catalysts costs while stabilizing and maintaining the strength of the active phase. An optimal support should be chemically inert, mechanically and thermally stable, with high specific solvent-accessible surface area, and have a balanced metal–support interaction[91, 92]. This last requirement implies that the dispersed metal should not alloy with the support because with such structures the metal is difficult to reduce and therefore remains inactive in FTS. Oxides of support materials, particularly SiO_2, Al_2O_3, and TiO_2 are the most extensively investigated supports for Co catalysts [93-95]. Silica nanosprings (NS) can meet and exceed the above support criteria. In fact, recently, FTS catalytic performances of cobalt decorated silica nanosprings (Co/NS) were evaluated and the results compared with those of conventional silica gel supported Co catalysts [96]. Even though Co/NS catalysts had 75 times less gravimetric Co content than the sol–gel catalysts, both catalysts showed similar selectivity to C_{5+} hydrocarbons and Co/NS showed higher FTS activity. However, there was an early drop in the CO conversion for Co/NS catalysts [96]. There are many factors that can influence the CO conversion. For example, unreduced Co species are reported to give lower CO conversion rates [40]. Other causes of catalyst deactivation include coking, sintering of Co nanoparticles and poisoning.

The focus of any catalyst development is to improve key properties, which are lifetime, activity and selectivity. In order to understand low CO conversion of Co/NS catalysts during FTS, H_2-programmed temperature reduction (H_2-TPR) was carried out to assess the reducibility of the catalysts. H_2-TPR analysis revealed an incomplete reduction, which was confirmed by X-ray photoelectron spectroscopy (XPS) analysis of the spent catalysts. To improve FTS performances of the NS supported catalyst, it is very important to thoroughly characterize the reduced state. The goal of this work is to determine the reduction state of Fischer-Tropsch Co/NS catalysts during activation. The reduction state has been characterized using in situ X-ray photoelectron spectroscopy (XPS), H_2-TPR, and transmission electron microscopy (TEM). Furthermore, the Co/NS catalyst FTS performance has been evaluated at two different reduction temperatures.

2.3 Experimental methods

2.3.1 Catalyst Preparation

NS were prepared in 0.5 g batches according to Wang et al. [66]. The Co/NS and Co/SiO_2 catalysts were prepared by incipient wetness impregnation of NS and SiO_2, respectively. NS (50 mg) were dried in air at 120 °C for 12h. Then were dispersed in ethanol (10 mL) by sonication and then a $Co(NO_3)_2$ solution (10 mL, 4.4 mg/mL) was added drop wise (3 h, 50 °C), oven dried at 120 °C, and then the obtained catalyst was calcined in air at 550 °C for 5 h. The process was repeated to obtain 15 (wt%) loading of Co. The Co/NS catalyst (20 mg) was loaded in a horizontal quartz tube furnace and reduced at either 409 or 609 ^{O}C under the flow of 5:95 H_2:N_2 mixture for 24h.

2.3.2 Catalyst Characterization

H_2-TPR spectra of the catalysts were was carried out in a ChemiSorb 2720 instrument (Micrometrics, USA) equipped with a TCD detector. The TCD was calibrated by the reduction of CuO (20 mg, 99.99%) between 25 and 500 ^{o}C. Before running each TPR experiment, the catalyst was flushed with N_2 (30 mL/min) at 150 ^{o}C for 1 h to remove the surface impurities and then cooled to 25 ^{o}C. The sample (50 mg) was loaded in a U-shape quartz reactor and first purged in a flow of He (50 mL/ min) at 250 °C for 1 h to remove water, cooled to 50 °C, then a 10% H_2 in Ar (50 mL/ min) was purged and heated to 800 °C at heating rate was 10 °C /min. The specific surface area (S_{BET}) of all degassed (220 ^{o}C for 30 min) catalysts (60-80 mg) were determined using an N_2 adsorption-desorption isotherm at -196 ^{o}C on a Micromeritics ChemiSorb 2720 instrument. The FT-IR spectroscopic analysis of the catalysts (10% mixed with KBr) was obtained in the diffuse reflectance mode using a Thermo Nicolet Avatar 370 DTGS spectrometer.

Morphologies of the catalysts were characterized by TEM (Jeol JEM-2010 TEM). The acceleration potential was 200 kV. Sample specimens for TEM analysis were prepared by dispersion of the catalysts in ethanol. One drop of the suspension was deposited onto a holey copper grid coated with a fine carbon film (FCF-150-Cu). Several micrographs were recorded for each sample to measure the Co particle size by using ImageJ software. Thermogravimetric analysis (TGA) of the sample (5 mg) was performed on a Perkin Elmer TGA-7 instrument from 25 to 800 ^{o}C at 20 ^{o}C /min under N_2 (30 ml/ min). The crystallographic information of the calcined catalysts was studied by XRD on a Siemens D500 powder diffractometer with Cu/kα (λ= 0.154 nm) radiation. Diffraction intensities were recorded from 10^{o}- 80^{o} (2θ value) with 0.01^{o} step using a 1 s acquisition time per step. The average crystallite size of iron oxides was calculated using the diffraction peaks according to the Scherrer equation[97]:

$$D = \frac{k\lambda}{\beta \cos \theta} \qquad \text{(Eq. 2-1)}$$

Where D is the average crystallite in nm, k is shape factor (for spherical shape particles, k = 0.9), λ is the wavelength of X-ray (λ = 1.54 Å), β is line broadening at half the maximum intensity (FWHM) in radians, θ is the Bragg angle.

XPS was carried out in a custom built ultra-high vacuum (UHV) chamber with a base pressure of 1.5×10^{-10} Torr. The chamber is equipped with an Omicron EA 125 hemispherical electron energy analyzer and a dual anode X-ray source. The Mg Kα emission line (1253.6 eV) was used for XPS data acquisition and the combined resolution of the X-ray/hemispherical energy analyzer was 300 meV. The sample was grounded and exposed to a 400 eV electron beam to avoid spurious charging. The chamber is also equipped with leak valves for gas (H_2) admission. In situ heating of the sample utilized a boron nitride heater and remotely monitored with an optical pyrometer. In situ reduction consisted of timed exposures of the sample to

1.0×10^{-6} Torr of H_2 at 385 °C and XPS spectra acquired after each exposure. For the reduction at 680 °C and 10 Torr of H_2, the sample was reduced in a separate chamber for 10 h and then transferred under vacuum to the UHV chamber for XPS analysis. Note, the reduction time of 10 h was only chosen to ensure full reduction. The photoelectron binding energy was referenced to the C 1s peak (284.7 eV) of adventitious carbon. The spectra were fitted using Igor Pro v6 (WaveMetrics) software using a Shirley background and Voigt functions. The same full width at half maximum (FWHM) was used for the two Co 2p spin states with a branching ratio of 2:1 (Co 2p3/2/ Co 2p1/2), and the spin-orbit splitting was held at 15.1 eV.

2.3.3 Catalyst Activation and evaluation

The FTS performance of Co/NS (20 mg) catalysts were evaluated in a quartz tube (10 mm Ø × 300 mm with a "0" quartz frit connected 180 mm from the top to support the catalyst), fixed-bed micro-reactor. The reactor was heated using a small tube furnace (Supelco) and regulated with a digital temperature controller. Reactant gases (CO (30 mL/min) and H_2 (60 mL/min)) and inert gas (N_2, 10 mL/min) were introduced from the top of the reactor, and the flow rates controlled with digital mass flow controllers (GC1, Dakota Instruments). The reactor was operated at 238 °C. Products were collected every 10 h in a three-stage impinger trap placed in a liquid nitrogen bath. Condensed liquid products were analyzed by gas chromatography-mass spectrometry (GC–MS, Focus-ISQ, ThermoScientific). Separation was achieved on an ZB-5ms (30 m × 0.25 mm) with a temperature program of 40–250 °C at 5 °C min^{-1}. 1,2,4-Trichlorobenzene was used as an internal standard. Compounds were identified by their mass spectra, library mass spectral matching (NIST 2008) and retention times of known standard n-alkanes (C_6–C_{44}).

2.4 Results and discussion

2.4.1 Catalyst preparation and characterization

Figure 2-1.shows a TEM micrographs of the calcined cobalt oxide nanoparticles on a NS. A NS is formed by five to eight coherently coiled silica nanowires. Moreover, the micrograph also shows the nano-helical structure of the NS. The Co nanoparticles are observed to be uniformly dispersed with some agglomerates on the NS support. The average Co particle size for Co/NS was 9.4 nm.

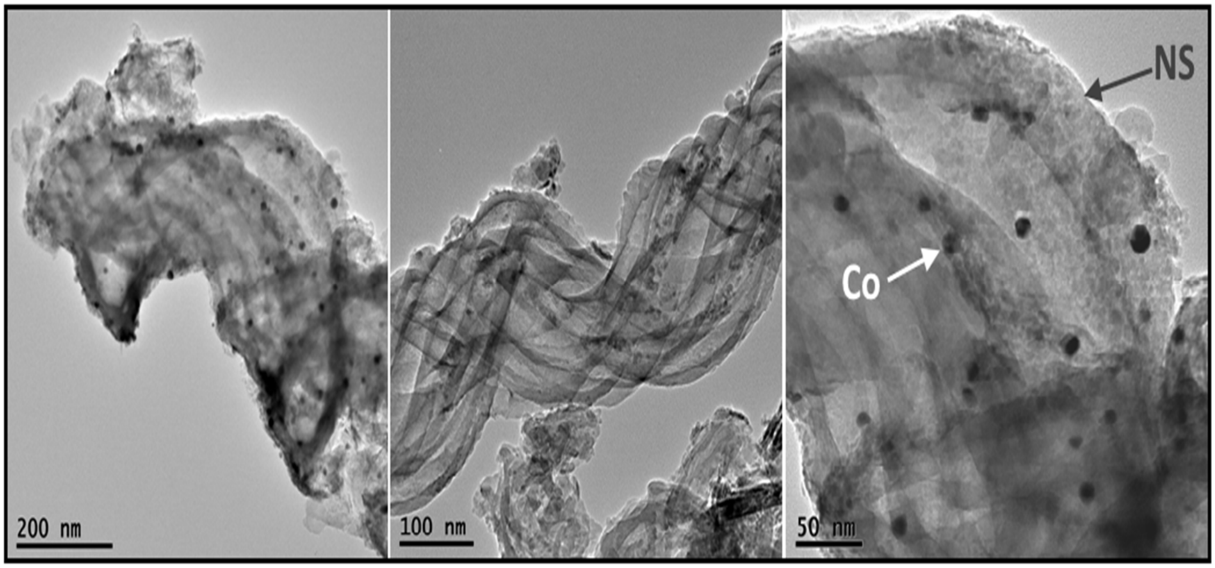

Figure 2.1. Transmission electron microscopy images of Co/NS catalysts

The (S_{BET}) specific surface area of virgin NS and calcined Co/NS catalyst were determined. The surface area of virgin NS was 302 m^2/g, while the calcined Co/NS catalyst had surface area of 213 m^2/g. The incorporation of Co on NS significantly decreases the surface area by 29.4%. This suggests that the Co nanoparticles nucleate within the pores of the NS.

The composition of the cobalt surface for Co/NS catalyst was analyzed by XPS. Figure 2.2 shows the Co 2p XPS spectra of the Co/NS catalyst. Characteristic metallic Co 2p peaks were observed at binding energies of 779.9 and 782 eV [2, 14–16]. Within experimental error, this composition is consistent with the Co3O4 spinel phase. The strong and broad features at higher binding energies correspond to the shake-up satellites of the Co^{2+} state [2, 14–16]. XPS was also used to attain information about the dispersion of Co_3O_4 spinel. For this purpose, XPS core levels states were integrated and corrected with atomic sensitivity factors obtained from the literature [17,18], thus allowing us to estimate the Co/Si ratio of 0.07. This value implies a high dispersion of small Co_3O_4 particles over the surface of the silica NS support, in good agreement with the TEM analyses.

H_2-TPR was carried out to evaluate the reduction behavior of the cobalt species in catalysts. Figure 2.3 shows the H_2-TPR profiles of the calcined Fe/NS catalyst and Co/SiO_2 as reference catalyst. Two peaks at were observed on the H_2-TPR profile of the Fe/NS and Co/SiO_2 calcined catalysts at 271 and 325 °C, and at 386 and 603 °C respectively. For the Co/NS catalyst, the first peak centered at 386 ^{o}C is attributed to the reduction of Co_3O_4 to CoO, whereas the second peak at 603 ^{o}C is assigned to the reduction of CoO to Co metal. Assuming this assignment holds for Co/SiO_2-gel, for Co/NS the large separation between the two maxima (more than 100 °C) suggests that they are a consequence of the reduction of cobalt oxides, which have stronger interaction strengths with the NS relative to the Co/SiO_2-gel [2]. Note, this interaction depends on the size of the metal oxide particle. Larger particles, which interact less with the support, will be reduced first during the low-temperature stage of the reduction process. The second reduction stage at higher temperature is associated either with the presence of small cobalt oxide particles on the surface of the support that have strong particle–support interaction strengths, or small particles deposited in small diameter pores, which are harder to reduce because of poor diffusion of hydrogen into the pores and the inability of water to diffuse from the pores [2]. Peaks in the range of 477–727 °C are typically attributed to reduction of a highly dispersed CoO_x surface phase, referred to as cobalt surface spinel which contains mainly Co^{2+} and possibly Co^{3+} ions [19], with a much stronger interaction with the support, which further supports the conclusion of a stronger interaction strength between the cobalt oxide nanoparticles and the silica NS surface relative to the silica sol–gel. H_2-TPR provides the temperature range for the reduction of Co_3O_4 to metallic Co. The TPR profile for the Co/NS clearly shows that the, 400 °C activation temperature for the Co/NS catalysts was insufficient for full reduction to metallic Co [9].

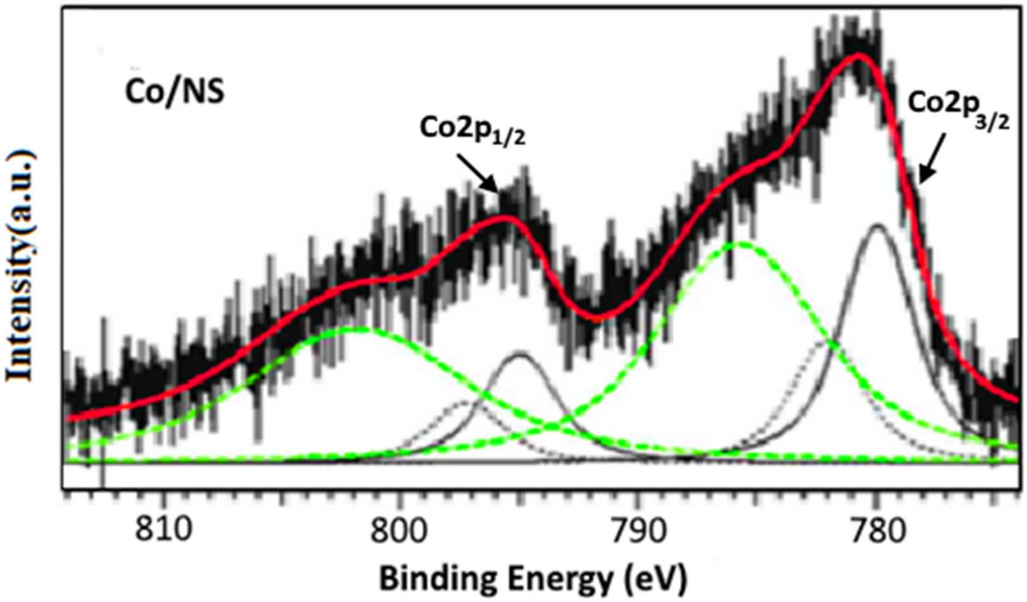

Figure 2.2. X-ray photoelectron spectra (XPS) of Co/NS catalyst

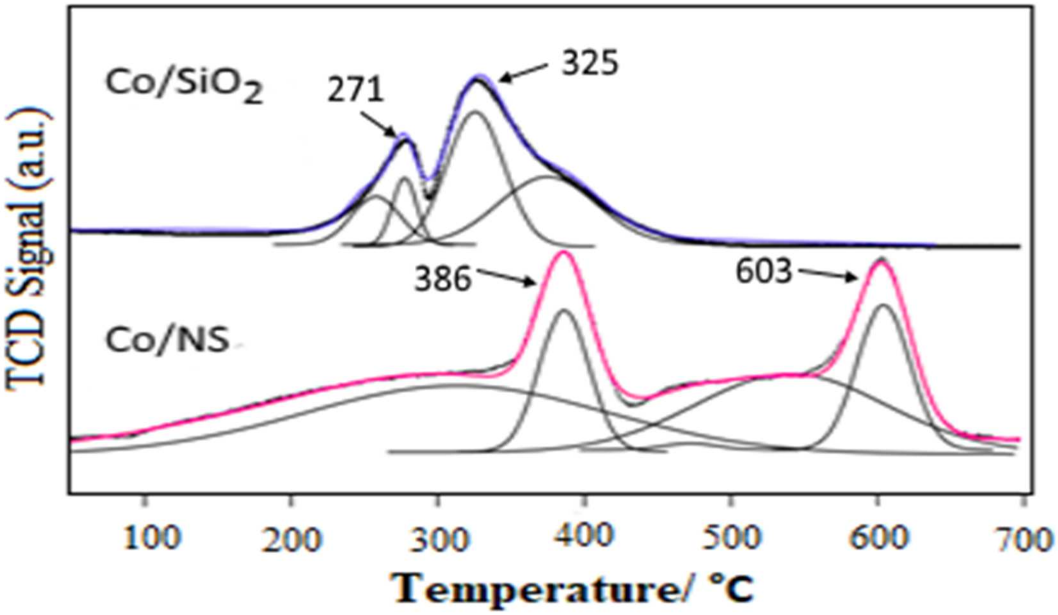

Figure 2.3. H_2-TPR profiles of calcined Co/SiO$_2$ and Co/NS catalysts.

XRD analysis of the cobalt oxide NS was used to determine cobalt oxide phase and particle size for the Co/SN catalyst. The XRD results of the Co/NS catalyst was compared with the Co/SiO_2 catalyst. The diffractograms are shown in Figure 2.3. The peak around 23˚ in both diffractograms of Co/SN and Co/SiO_2 catalysts is assigned to crystal planes of the silica NS and SiO_2, respectively [98, 99]. The Co/SiO_2 catalyst has six major diffraction peaks centered at $2\theta = 22.°$, 30.9°, 38.2°, 44.8°, 59.3°and 65.2°, which correspond to the (111), (220), (311), (400), (511), and (440) diffraction planes, respectively, of Co_3O_4, respectively [100, 101]. The average crystallite size (d_{XRD}) of Co_3O_4 for Co/SiO_2 catalyst was calculated to be 14.3 nm from the (311) diffraction peak at $2\theta = 38.2$ °using the Scherrer's formula. The Co/NS catalyst had diffraction peaks at $2\theta = 21.3°$, 31.7°, 38.5°, 44.6°, 59.4°and 65.2°, which correspond to diffraction planes of (111), (220), (311), (400), (511), and (440) planes, respectively. The diffraction peaks are in good agreement with the reference data for the Co_3O_4 structure [100, 101]. The average crystallite size of Co_3O_4 for Co/NS catalyst was 12.3 nm based on the peak at 38.4°. XRD results indicate the formation of Co_3O_4 on both SiO_2 and NS supports.

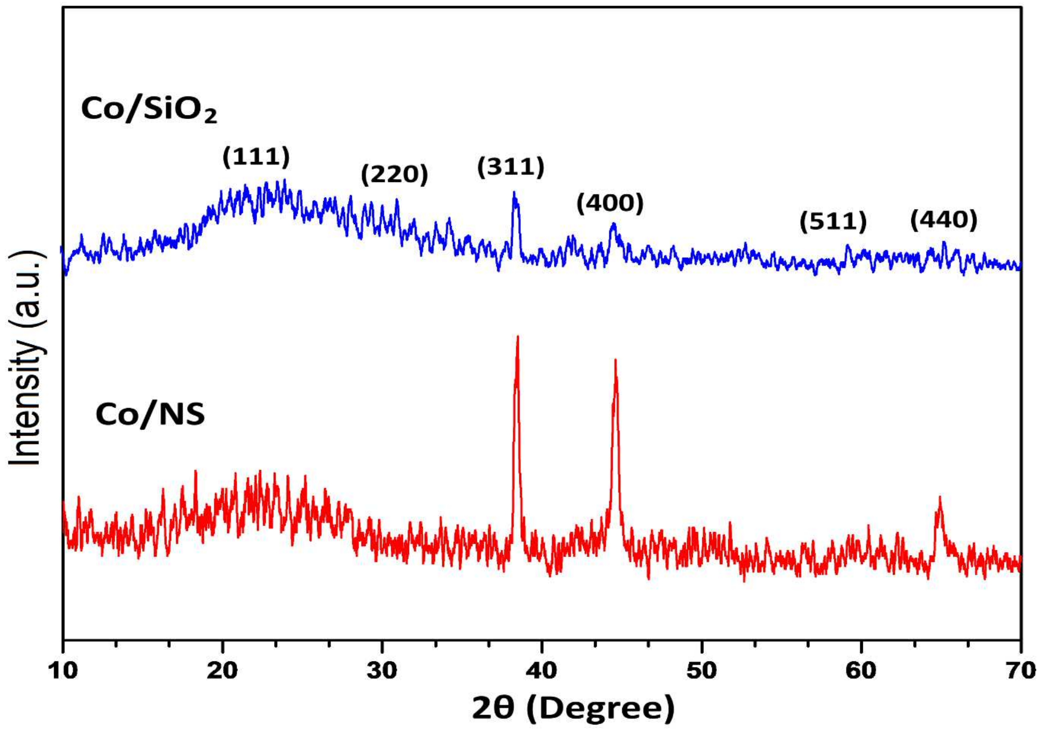

Figure 2. 4. X-ray diffractograms of calcined Co/NS and Co/Sio$_2$ catalysts

FTIR spectroscopy was recorded to determine the characteristic bonding with the NS and the Co_3O_4 nanoparticles, as well as the presence of molecular species bonded to the surfaces of the catalysts NS (Figure 2.5). It was found that both catalysts had characteristic peaks of SiO_2 bonds at approximately 1090 cm^{-1} and 813 cm^{-1}, which can be attributed to Si–O–Si stretching and Si–O bending vibrations, respectively, which is in good agreement with the literature [101-104]. In addition, the FTIR spectrum shows characteristic peaks at approximately 2950 cm^{-1} and between 1411 - 1461 cm^{-1} are related to C-H stretching and bending vibrations, respectively. The bands at approximately 3430 and 1627 cm^{-1} can be attributed to the H-O-H stretching and vibration of hydrogen bonded surface silanol groups and physically adsorbed water, respectively [101, 104-106]. For the Co/SiO_2 catalyst sample, a shoulder of weak peak at around 960 cm^{-1} also can be attributed to OH bending of the Si-OH groups [101]. The absorption bands of Co–O bond were observed in both catalysts at approximately 586 cm^{-1} and 664 cm^{-1} ,and are in good agreement with the literature [101]. Compared with that of Co/SiO_2, the intensity of this band apparently declined in the FT-IR spectra of the Co/NS. This indicates that some strong interaction occurs between Co and NS.

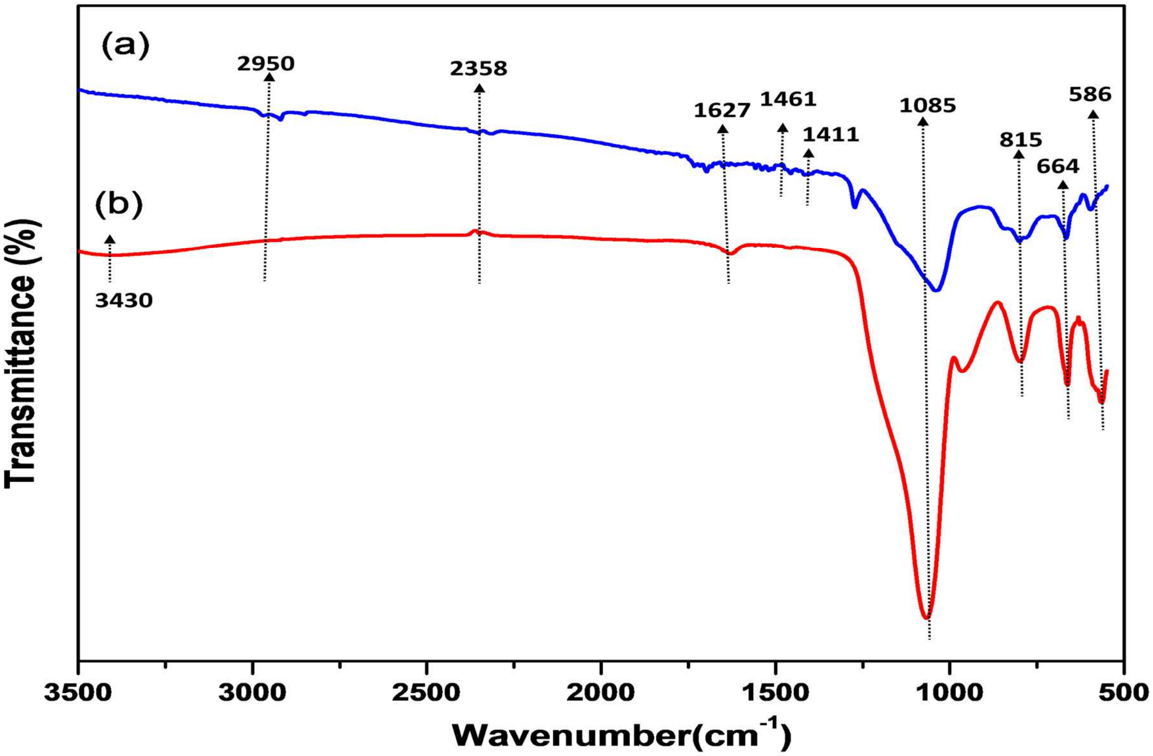

Figure 2.5. FTIR spectra of calcined (a) Co/NS and (b) Co/SiO_2 catalysts

The thermal stability of the calcined catalysts was determined by TGA. Figure 2.6 shows the TGA thermograms of the calcined Co/NS and Co/SiO_2 catalysts. The calcined Co/NS and Co/SiO_2 catalysts showed a total weight loss of approximately 9.0 % and 9.8%, respectively at 900 ^oC. This weight loss is probably due to evaporation of adsorbed material on catalysts. The TGA of Co/SiO_2 catalyst were in good agreement with the literature [8]. The calcined Co/SiO_2 catalyst showed about 5 % loss below 100 ^oC, which can be attributed the loss of moisture. Additionally, the weight loss was observed above 600 ^oC in the calcined Co/NS catalyst can be attributed to the incomplete removal of material during calcination. The TGA of the calcined Co/NS and Co/Sio_2 catalysts showed no significant decomposition until 900 ^oC, which clearly implies that both catalysts have good thermal stability.

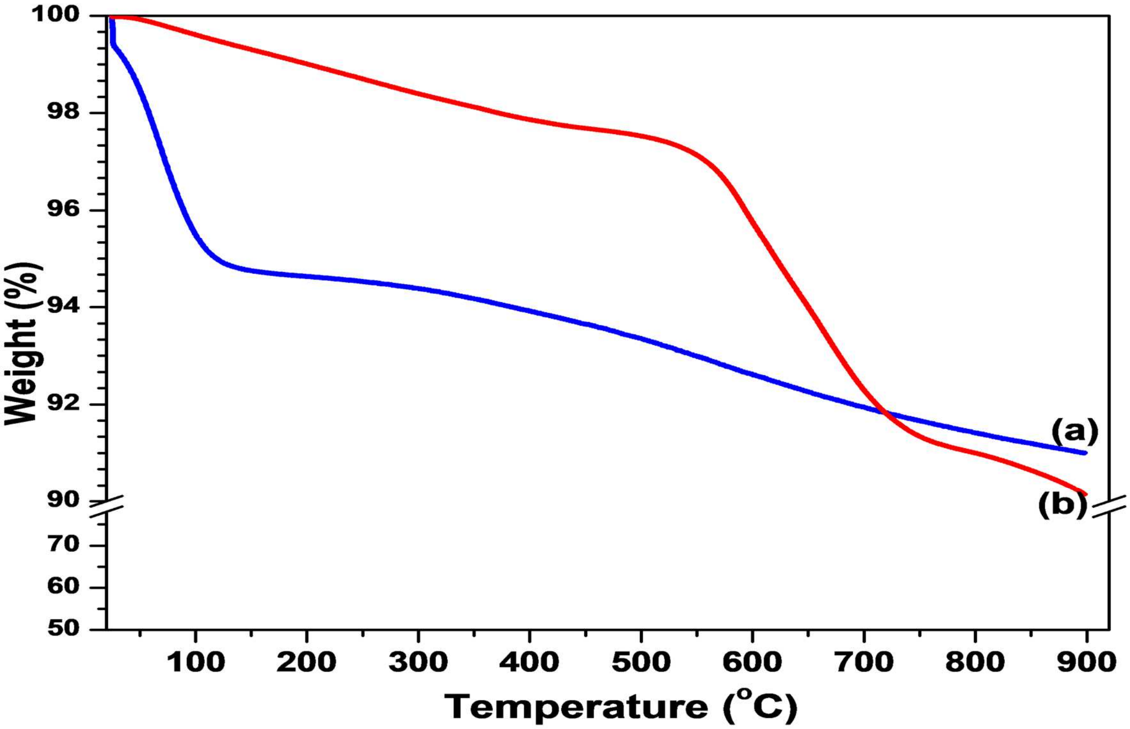

Figure 2.6. TGA thermograms of calcined (a) Co/SiO_2, (b) Co/NS catalysts.

2.4.2 Catalyst Evaluation

The Co/NS catalysts were reduced with H_2 under two different reduction temperature to look at their effects of FTS efficiency. The catalytic performances of the Co/NS catalysts reduced at 409 and 609 °C were carried out in a quartz fixed-bed micro-reactor at 238 °C with a H_2/CO ratio of 2 for 10 h. The condensable liquid products were analyzed by GC-MS and the non-condensable gases (CO, CO_2, H_2, N_2 and CH_4) were analyzed by GC. The FTS activity measured by CO conversion and hydrocarbons distribution results were calculated. GC–MS analysis of the FTS performance of Co/NS catalyst reduced at 409 and 609 °C (Figure 2.7) reveal slightly different product profiles (hydrocarbons (HC) ranging from C_6 to C_{17}) between the catalysts (Figure 2.8) and similar to previous work [9] and the literature [25,4]. The main HC produced were C_7, C_8, and C_9, which comprised 67–77% of the product and fall within the JP-4 jet fuel (C_5–C_{14}) and gasoline (C_5–C_{12}) range. However, the C_6–C_{17} HC production rate for the fully reduced catalyst (609°C) was 3.4-fold higher (1.37 g HC/g-catalyst/h) than the partially reduced catalyst (0.40 g HC/g catalyst/h). Furthermore, a higher proportion of alkenes to alkanes were produced with the fully reduced catalyst (alkene/alkane = 2.4) than the partially reduced catalyst (alkene/alkane = 1.4). The peak CO conversion obtained for the fully reduced Co/NS catalyst was 88%, as compared to 69% for the partially reduced catalyst. These results support the findings described in the previous sections and that the Co/NS catalyst needs to be fully reduced at or above 600°C to optimize its performance.

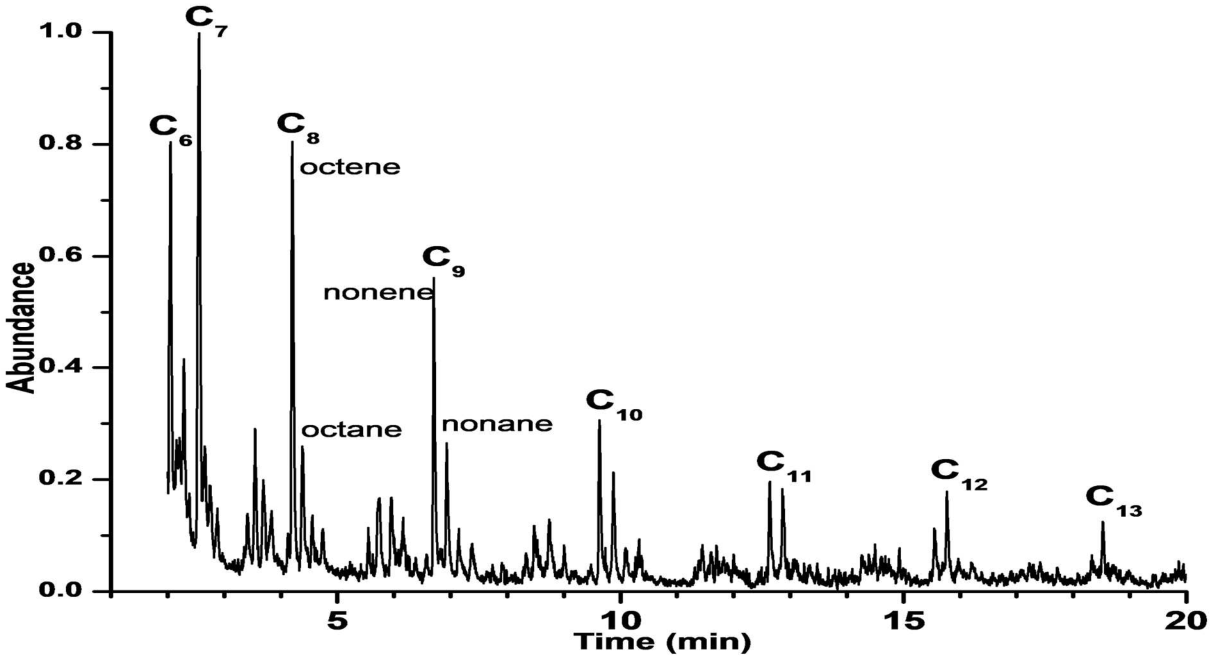

Figure 2.7. Overall FTS product spectrum obtained using GC-MS analysis, for Co/NS reduced at 609°C, at 238°C and atmospheric pressure with a H_2/CO ratio of 2 for 10 h.

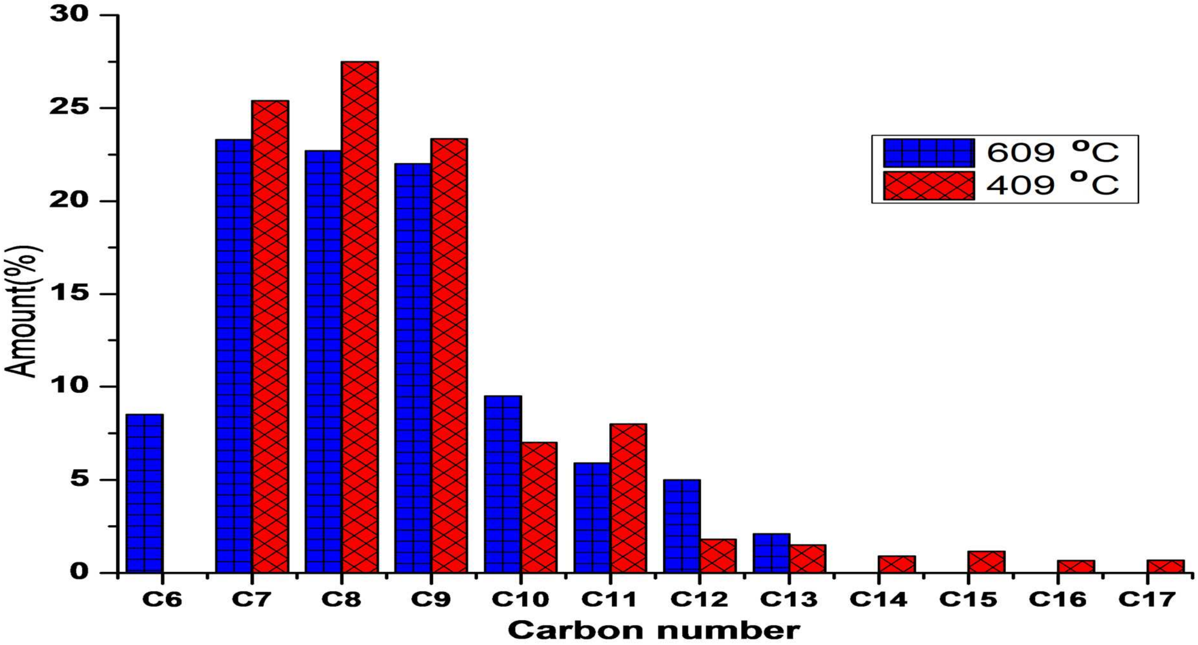

Figure 2.8. Distribution of FT hydrocarbons (C_6-C_{17}) products from Co/NS catalyst reduced at 409 and 609 °C.

2.4.3 Conclusion

The observed hydrogen reduction of a Fischer-Tropsch Co catalyst supported on silica nanosprings (NS) by XPS and TPR indicated a larger interfacial interaction between the Co nanoparticles and the silica surface of the NS relative to a tradition sol–gel supported Co catalyst. This significantly higher reduction temperature for the Co/NS catalyst (∼600 ^{o}C) is attributed to heat loss by convection and radiation due to the high surface to volume ratio of the NS and a large interfacial interaction between the Co nanoparticles and the silica surface of the NS. Increasing the catalyst reduction temperature to just above 600 ^{o}C significantly increased the FTS activity and hydrocarbon production, in agreement with the XPS and TPR data. Finally, evaluation of the fully reduced FTS Co/NS catalyst demonstrated that it can produce drop in JP-4 and gasoline fuels.

CHAPTER 3: EFFECT OF SYNTHESIS AND ACTIVATION METHODS ON THE CATALYTIC PROPERTIES OF SILICA NANOSPRING (SN)-SUPPORTED IRON CATALYST FOR FISCHER-TROPSCH SYNTHESIS

3.1 Abstract

A nanostructured iron (Fe) catalyst for Fischer-Tropsch synthesis (FTS) was prepared and evaluated using a silica nanospring (NS) support. FTS offers an approach of producing biofuels from synthesis gas (syngas) produced via biomass gasification. The Fe/NS catalysts were prepared using three different methods: (i) incipient wetness impregnation, (ii) precipitation and (iii) modified sol-gel, in order to obtain different sizes of deposited Fe nanoparticles on the NS support and investigate the influence of particle size on FTS. The Fe decorated catalysts were calcined and then activated with either H_2, CO or H_2+CO mixture. The prepared Fe/NS catalysts were characterized before the FT reaction by BET surface area, X-ray diffraction (XRD), transmission electron microscopy (TEM), temperature programmed reduction (TPR), X-ray photoelectron spectroscopy (XPS) and thermogravimetric analysis (TGA) in order to find correlations between physico-chemical properties of catalysts and catalytic performance. The decoration of Fe nanoparticles of different sizes onto NS using the various methods ranged from 1.7 to 10 nm. The FTS performance was also evaluated in a quartz fixed-bed microreactor (H_2/CO of 2:1, 270 ^{o}C) and the products trapped and

analyzed by GC-TCD and GC-MS to determine CO conversion and reaction selectivity. These results show that the highest CO conversion (76.6%) and a wide distribution of light hydrocarbon (C_6 to C_{14}) were obtained for Fe/NS catalyst prepared by impregnation and activated with CO after 12 h of the FT reaction.

3.2 Introduction

Fischer-Tropsch synthesis (FTS) has been recognized as one of the most promising alternative technologies in converting syngas derived from coal, natural gas and biomass into liquid transportation hydrocarbon fuels and chemicals. Over the years, the FTS process is still subject to further research and development to improve the efficiency of FTS technology in order to produce a wide variety of hydrocarbons products [107]. In order to improve the catalytic performance of FTS catalysts, active metal catalysts such as iron (Fe) and cobalt (Co) are generally supported on conventional support materials such as SiO_2, Al_2O_3, and TiO_2 gels [108, 109]. Although there are many positive sides of FT catalysts supported on conventional substrates, there are also some technical and economic challenges that still need to be overcome, including strong metal oxide–support interaction, the price of the active metal (Ru and Co), catalyst lifetime and catalyst deactivation [55, 110]. All these limitations will either inhibit the FT catalytic activity or increase the cost of fuel production. It is therefore necessary to find efficient ways to overcome these obstacles and challenges. Approaches for overcoming these limitations are to change the support, addition of promoters, synthesis and activation methods. These will have a significant influence on the metal dispersion, particle size, minimizing the cost of the catalyst, reduction behavior, catalytic activity and FT selectivity [55, 111].

Although a number of studies were carried out on the effect of synthesis and activation methods of different Fe catalyst on the FTS performance [112, 113], further research is still needed to develop new FT catalysts that improve the quality and value of FTS products. The synthesis of the Fe catalysts have been studied extensively and many synthesis catalyst methods such as sol-gel (-S), precipitation (-P) and incipient wetness impregnation (-I) have been successfully applied in the synthesis of Fe-based catalysts [112, 114-117]. However, the synthesis methodology plays a key role in controlling the morphology, catalyst particle size, size distribution and surface area [106, 118]. For example, Tasfy et al. [112] reported that the average Fe nanoparticle size over SiO_2 was smaller when prepared by the impregnation catalyst synthesis method, as compared to the precipitation method. Sarkari et al. [115, 116] investigated the effect of impregnation and co-precipitation methods of $Fe/Ni/Al_2O_3$ catalyst on the FTS performance. They found that the impregnated catalyst had higher activity and higher selectivity to light olefin and C_5+ products than the co-precipitated catalyst.

Catalyst activation methods of supported and unsupported iron oxide catalysts have been investigated in order to improve the performance of FTS [119]. The phases of the iron catalysts are typically present as metallic iron (α-Fe), Fe oxides, and Fe carbides (Fe_xC_y) during the FT reaction [86]. In FTS, the iron oxide catalyst is inactive, so it is necessary to change the oxidation state of iron into an active phase (metallic Fe or iron carbides) for the FT reaction to occur [86, 88], and depending on the activation agents used. The activation of an iron-based catalyst by common activation agents (i.e., H_2, CO or H_2+CO mixture) has a significant influence on the FTS activity, selectivity, and the surface phase composition [88, 119, 120]. Several studies have reported that activation of iron oxide catalyst with CO showed a superior FTS activity compared to H_2 and H_2+CO mixture. For example, Luo et al. [88] studied the activation of low α-iron catalyst with three different activation agents (i.e., H_2, CO or H_2+CO mixture). They found that higher CO conversion was obtained when activation with CO and syngas. Bian and co-workers [86] studied the activation effect of CO and H_2 on precipitated Fe_2O_3 catalyst and concluded that the CO activation produced higher catalytic activity for FT synthesis than the H_2-activated iron catalyst. They also found that the surface area of the H_2-activated iron catalyst showed a small decrease compared with that of the CO-activated iron catalyst. Similar results were obtained by Ding et al. [121] with a Fe-Mn-K-SiO_2 catalyst. Furthermore, they reported that the CO activated catalyst presented the highest initial activity compared to the H_2 and syngas activated catalysts. Several conventional catalyst support materials (SiO_2, Al_2O_3, and TiO_2) have been extensively used and investigated as supports for FTS catalysts. However, unconventional catalyst support materials such as 1-dimensional (1D) nanomaterials (e.g., carbon nanotubes (CNTs), tin oxide nanowires (SnO_2) and carbon nanofibers (CNFs)) have recently attracted considerable attention as potential supports in FTS catalysts [113]. This is mainly due to their unique structure, properties (e.g, high surface area and high thermal stability) and ability to improve the performance of the FTS catalyst.

Silica (NS) is a new 1D support material and has been recognized as meeting the criteria of supports because they have (i) high surface area (300 m^2/g), (ii) high thermal stability (up to 1000 ^oC), (iii) easy to grow, and (iv) can be grown in various surfaces [68]. Up to now, NS is a relatively new support material for FTS, hence, only two studies have used NS as a FT support [21, 22]. The first proof of principle study of NS as a new high surface area support for Co-FTS catalyst was to produce hydrocarbons from the hydrogenation of [69]. A subsequent study showed that the Co-NS catalyst was not fully activated/reduced at 409^oC under H_2 prior to FTS evaluation and , where H_2-TPR and XPS studies showed that full activation required H_2 reduction at 609^oC, which subsequently improved CO conversion [70].

In the present study, three different 1D iron-NS catalysts were prepared to obtain differing Fe particle size distributions using three different methods: incipient wetness impregnation, precipitation and modified sol-gel. The catalysts were calcined and then activated with either H_2, CO or H_2+CO mixture. The catalysts were characterized by a combination of XRD, XPS, TGA, TEM, H_2 and CO temperature programed reduction (H_2-TPR, CO-TPR, FT-IR spectroscopy and surface area measurements. The effect of synthesis method and activation conditions on catalytic performance of 1D Fe/NS catalysts for FTS were studied.

3.3 Experimental methods

3.3.1 Catalyst Preparation

NS were prepared in 0.5 g batches according to Wang et al. [66]. Fe/NS catalysts with total Fe loading of 15% were prepared using three different methods: (a) incipient wetness impregnation; (b) precipitation and (c) modified sol-gel.

(a) Incipient wetness impregnation:

NS (75 mg) were dispersed in ethanol (15 mL) to which a solution of Fe $(NO_3).9H_2O$ (100 mg in 15 mL water) was added drop-wise under ultrasonication for 15 min. The mixture was stirred at 80 ^oC for 24 h, air dried at 110 ^oC for 24 h, and then calcined in air at 500 ^oC for 5 h and called Fe/NS-I [112, 122].

(b) Precipitation method:

NS (75 mg) were dispersed in ethanol (15 mL), mixed with Fe $(NO_3).9H_2O$ solution (100 mg in 15 mL water), and heated to 70 ^oC. The mixture was precipitated using 0.2M sodium hydroxide to obtain a pH of 9-10 at 80 ^oC. The precipitate was aged for 2 h, filtered and washed with water until neutral. The precipitated solid was dried at 110 ^oC

overnight, calcined in air at 600 ^oC for 5 h, ground and sieved, and called Fe/NS-P [112].

(c) 2-Step sol–gel method:

Fe nanoparticles without NS were prepared by sol-gel method using Fe $(NO_3).9H_2O$ (1.5 g in 60 mL water) to which citric acid (3 g) was added under ultrasonication for 2 h. The solution pH was adjusted to 10 using 1M NaOH solution. The mixture was heated overnight at 70 ^oC resulting in a viscous brown gel being formed. The gel was then dried at 110 ^oC for 8h and calcined in air atmosphere at 400 ^oC for 5 h [3]. The second step was to disperse the magnetite nanoparticles (20.4 mg) in water (10 mL) and then mixed overnight with a suspension of NS (50 mg) in ethanol (10 mL). The mixture was dried at 110 ^oC for 12 h and then calcined at 600 ^oC in air atmosphere for 4 h and called Fe/NS-S [4].

3.3.2 Catalyst Characterization

The reduction and carburization behavior of the calcined catalysts (30 mg) were performed by H_2-TPR and CO-TPR using a ChemiSorb 2720 instrument (Micrometrics, USA) equipped with a TCD detector. The TCD was calibrated by the reduction of CuO (20 mg, 99.99%) between 25 and 500 ^oC. Before running each TPR experiment, the catalyst was flushed with N_2 (30 mL/min) at 150 ^oC for 1 h to remove the surface impurities and then cooled to 25 ^oC. H_2-TPR and CO-TPR experiments were conducted in a 10 vol. % H_2 or 5 vol. % CO, respectively in N_2 atmosphere with a total flow rate of

30 mL/min. The temperature was ramped from 25 to 1000 ^oC for H_2-TPR and from 65 to 700 ^oC for CO-TPR both at a heating rate of 10 $^oC\cdot min^{-1}$.The specific surface area (S_{BET}) of all degassed (220 ^oC for 30 min) catalysts (60-80 mg) were measured using an N_2 adsorption-desorption isotherm at -196 ^oC on a Micromeritics ChemiSorb 2720 instrument. The FT-IR spectroscopic analysis of the catalysts (10% mixed with KBr) was obtained in the diffuse reflectance mode using a Thermo Nicolet Avatar 370 DTGS spectrometer.

The crystallographic information of the calcined catalysts was studied by XRD on a Siemens D500 powder diffractometer with Cu/kα (λ= 0.154 nm) radiation. Diffraction intensities were recorded from 10^o- 80^o (2θ value) with 0.01^o step using a 1 s acquisition time per step. The average crystallite size of iron oxides was calculated using the diffraction peaks according to the Scherrer equation[97]:

$$D = \frac{k\lambda}{\beta \cos\theta} \qquad \text{(Eq. 3-1)}$$

Where D is the average crystallite in nm, k is shape factor (for spherical shape particles, k = 0.9), λ is the wavelength of X-ray (λ = 1.54 Å), β is line broadening at half the maximum intensity (FWHM) in radians, θ is the Bragg angle. The morphology of the catalysts (dispersed in ethanol and applied to a copper grid coated with carbon support film) was observed by TEM (Jeol JEM-2010 TEM) operated at 200 kV. Several micrographs were recorded for each sample to measure the Fe particle size by using ImageJ software.

TGA of the sample (5 mg) was performed on a Perkin Elmer TGA-7 instrument from 25 to 800 °C at 20 °C/min under N_2 (30 ml/min). XPS experiments were performed on a custom built ultrahigh vacuum (UHV) chamber using the Al Kα radiation (hν = 1486.6 eV) and kinetic energy of the photoelectrons was measured with an electron energy analyzer, with a net resolution of 25 meV.

3.3.3 Catalyst Activation and evaluation

To create a more uniform bed temperature, approximately 20 mg of each calcined Fe/NS catalyst with 40 mg quartz sand was loaded into a quartz fix-bed micro-reactor (10 mm Ø x 300 mm with a “0” quartz frit connected 180 mm from the top to support the catalyst) housed in a tube furnace (25 mm ID x 150 mm) , and then reduced in either H_2 (43 mL/min), CO (40 mL/min), or CO + H_2 (55 mL/min) using mass flow controllers (Figure 3.1). The reactor temperature was increased from room temperature to 750 °C for 24 h at atmospheric pressure. The activation of unsupported Fe_2O_3 catalyst with H_2, CO, CO+H_2 mixture can be described by following three reduction steps:

$$\alpha\text{-}Fe_2O_3 \xrightarrow{\text{Step 1}} Fe_3O_4 \xrightarrow{\text{Step 2}} FeO \xrightarrow{\text{Step 3}} \alpha\text{-}Fe \text{ or } Fe_xC \quad \text{(Eq. 3-2)}$$

The activated/reduced catalyst was cooled to 175 ^{o}C and subsequently used for *in situ* FTS reactions. Figure 3.1 shows the FTS reactor set up. H_2 (55 mL/min), CO (35 mL/min) and N_2 (10 mL/min) were introduced at the top of the reactor using mass flow controllers. The FTS reactor was operated at 270 ^{o}C. The FTS reaction products were collected in a three-stage impinger trap placed in a liquid nitrogen bath. The uncondensed vapor stream was collected in a TedlarTM PVF (300 × 300 mm^2) gas-sampling bag. FTS reaction was maintained for 12 h at temperature. Unreacted gases and gaseous reaction products (CO, CO_2, H_2, N_2 and C_xH_y ($x \leq$ C4)) were determined by GC-TCD (GOW-MAC, Series 350) with a packed HaySep DB stainless steel column (3.3 mm ID x 9.1 m) at room temperature on elution with He. The liquid products C_xH_y ($x \geq C_5$) collected were then identified by GC-MS (Fous-ISQ, ThermoScientific). Separation was achieved on a ZB5ms (0.25 mm ID x 30m, Phenomenex) capillary column with a temperature program of 40 ^{o}C (1 min) ramped to 250 ^{o}C at 5 ^{o}C/min. Data was analyzed using the Xcalibur v2 software. The CO conversion, CO_2 selectivity and hydrocarbon selectivity were calculated using following Eqs. ((3-3), (3-4) and (3-5)), respectively,

$$\text{CO conversion (\%)} = \frac{(moles\ of\ CO)in-(moles\ of CO)out}{\text{(moles of CO) in}} x100 \qquad \text{(Eq. 3-3)}$$

$$\text{CO2 selectivity (\%)} = \frac{(moles\ of CO2)out}{(moles\ CO\ )\ in-(moles\ CO\ )out} x100 \qquad \text{(Eq. 3-4)}$$

$$HC\ selectivity\ (\%) = \frac{(moles\ of HCproduced)}{(moles\ CO\ in)-(moles\ CO\ out)} x100 \qquad \text{(Eq. 3-5)}$$

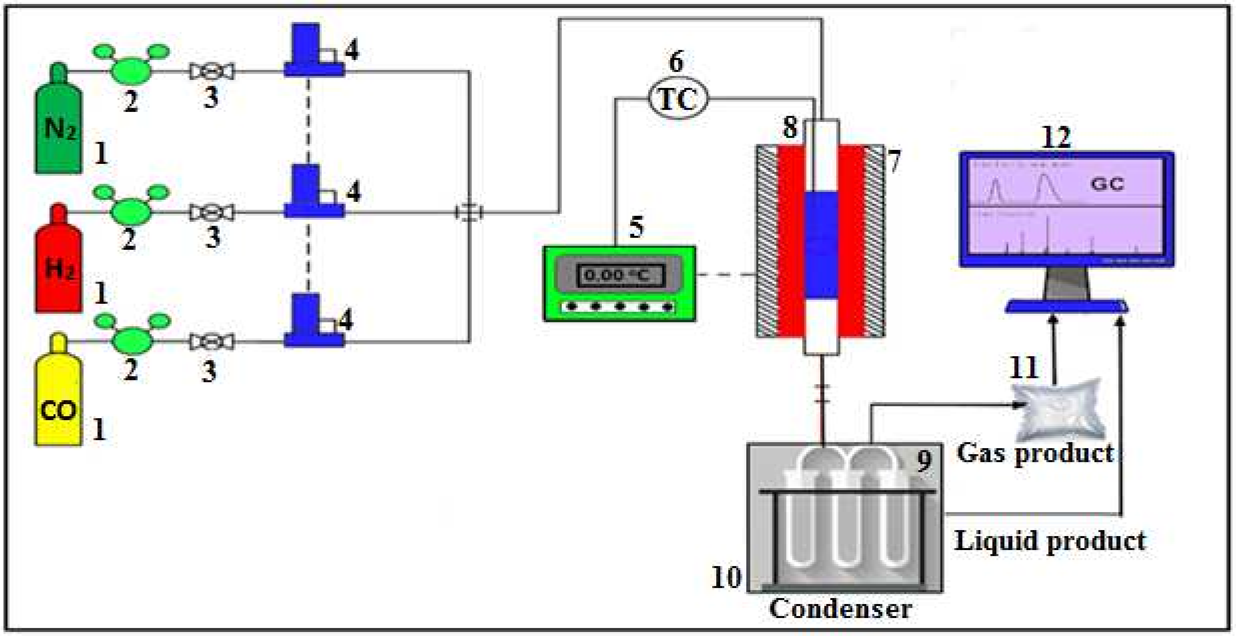

Figure 3.1. Schematic diagram of FTS apparatus used. (1) gas cylinders (H_2, CO and N_2), (2) pressure regulators, (3) ball valves, (4) mass flow controllers, (5) temperature controller, (6) thermocouple (Type-K) (7) furnace, (8) quartz tubular reactor, (9) 3-stage condenser-impinger, (10) liquid nitrogen bath, (11) gas sampling bag, (12) gas chromatograph.

3.4 Results and discussion

3.4.1 Catalyst preparation and characterization

Incipient wetness impregnation, precipitation and modified sol-gel produced Fe nanoparticles of different size ranges. TEM has been employed to determine the particle size distribution of calcined Fe/NS-I, Fe/NS-P and Fe/NS-S catalysts (Figure 3.2). In the micrographs the dark spots are Fe particles on the of NS surface. The micrograph also shows the nano-helical structure of the NS. Figure 3.2c shows that Fe nanoparticles are more dispersed on the surface of Fe/NS-I than that of Fe/NS-S

(Figure 3.2a), whereas Fe nanoparticles of Fe/NS-P are observed to be heterogeneously dispersed with some agglomerates on the surface (Figure 3.2b). The average Fe particle size for Fe/NS-S, Fe/NS-I and Fe/NS-P arewere 1.7 ± 0.1 nm, 4.1 ± 0.5 nm and 10.1 ± 0.4 nm, respectively (Table 3.1). These results show that we can control Fe nanoparticle size on the NS substrate by using different deposition methods and thereby influence FTS performance.

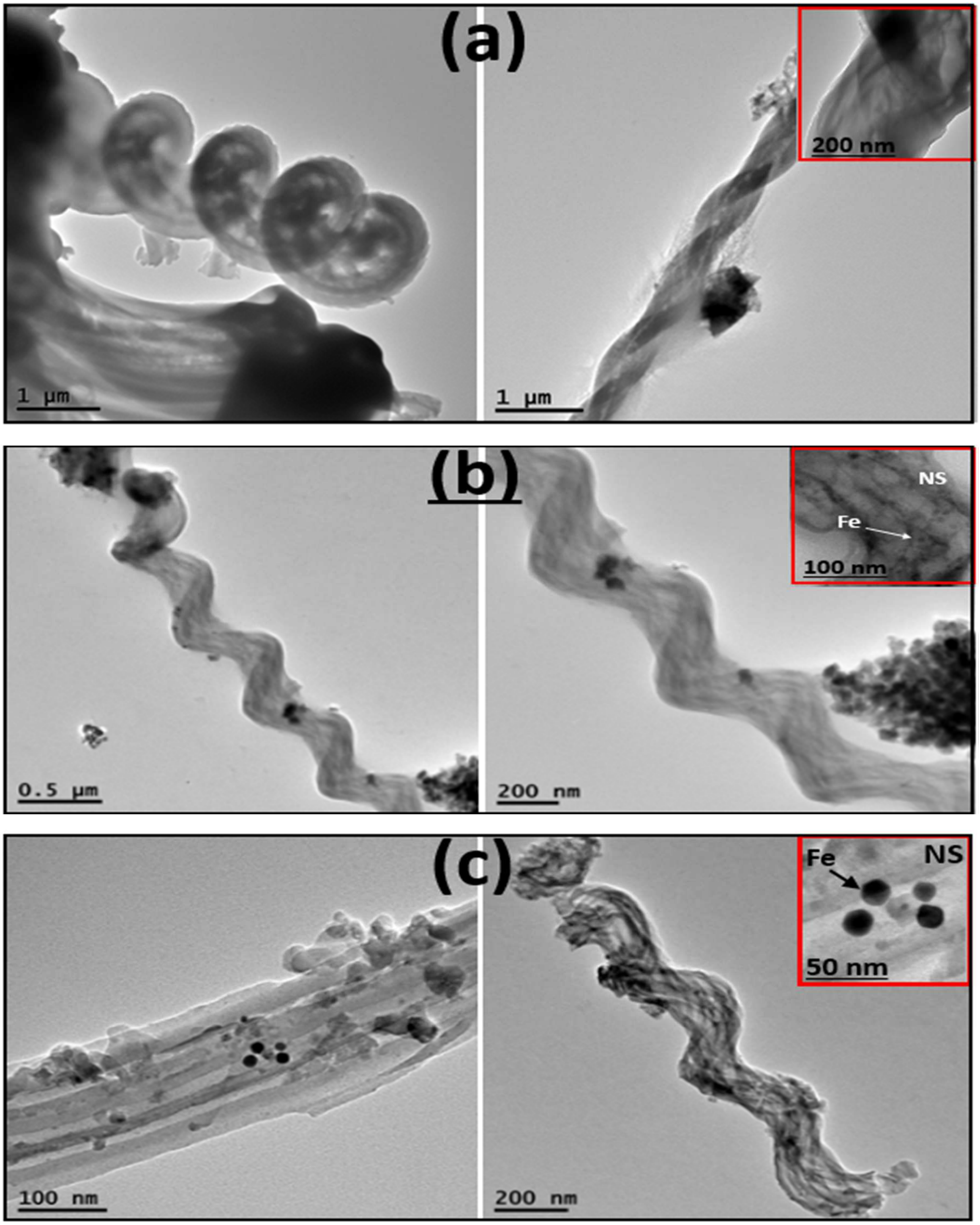

Figure 3.2. Transmission electron microscopy images and particle size distributions of Fe/NS-S (a), Fe/NS-P (b) and Fe/NS-I (c) catalysts

Table 3.1. Fe nanoparticle crystallographic data and average diameter determined by TEM and XRD analyses.

Catalyst	Phases present	d_{TEM} (nm)	d_{XRD} (nm)
Fe/NS-S	Fe_3O_4	1.7	2.6
Fe/NS-I	γ-Fe_2O_3	4.1	7.1
Fe/NS-P	α -Fe_2O_3	10.1	8.8

XRD analysis of the iron oxide NS was used to determine iron oxide phase and particle size for the three calcined catalyst preparations. The diffractograms are shown in Figure 3.3 and summarized data is given in Table 3.1. The peak at 2θ = 24˚ in all three Fe/NS diffractograms is assigned to crystal planes of the silica NS [98, 99]. The diffractograms of the calcined Fe/NS-I, Fe/NS-P and Fe/NS-S catalysts identify the presence of three different iron oxide phases. The Fe/NS-I sample has seven major diffraction peaks centered at 2θ = 33.2°, 35.7°, 44.2°, 44.4°, and 77.4°, which correspond to the (220), (311), (400), (422), (511), and (533) diffraction planes, respectively, of maghemite (γ-Fe_2O_3; JCPDS card 39-1346) [97, 117] [123-125]. The average crystallite size (d_{XRD}) of γ-Fe_2O_3 for Fe/NS-I catalyst was calculated to be 7.1 nm from the (311) diffraction peak at 2θ = 35.37°using the Scherrer's formula. The Fe/NS-S catalyst had diffraction peaks at 2θ = 30.3°, 35.6°, 38.3°, 40.1°, 44.6°, 57.2°, 64.8° and 77.5°, which correspond to diffraction planes of (220), (311), (222), (400), (422), (511), (440), and (533) planes, respectively. The diffraction peaks are in good agreement with the reference data for the magnetite structure (Fe_3O_4 ; PDF#19-0629)[125-128]. The average crystallite size (d_{XRD}) of Fe_3O_4 for Fe/NS-S catalyst was 2.6 nm. The Fe/NS-P catalyst has diffraction peaks at 2θ = 24.1°, 33.2°, 35.4°, 38.2°, 49.4°, 53.8°, 57.5°, 62.3°, 64.1°and 75.2°, which correspond to diffraction planes of (012), (104), (110), (113), (024), (116), (018), (214), (300) and (220) planes, respectively. The diffraction peaks are consistent with a hematite structure (α-Fe_2O_3; JCPDS card 33-0664) [124, 125, 129]. The average crystallite size of α-Fe_2O_3 for Fe/NS-P catalyst was 8.8 nm based on the peak at 33.24°.

The average iron oxides particle size for the three catalysts determined by XRD and TEM were comparable (Table 3.1). XRD results show that iron oxide was formed as α-Fe_2O_3, γ-Fe_2O_3 and Fe_3O_4 on the surface of Fe/NS-P, Fe/NS-I and Fe/NS-S catalysts, respectively, which have no activation for FTS. It is difficult to distinguish between the γ-Fe_2O_3 and Fe_3O_4 with XRD analysis due to their similar crystal structures and/or poor dispersion of iron on the support [125, 130] [99, 131]. Therefore, the catalysts were analyzed by XPS to further ascertain the composition of the surface of calcined Fe/NS catalysts.

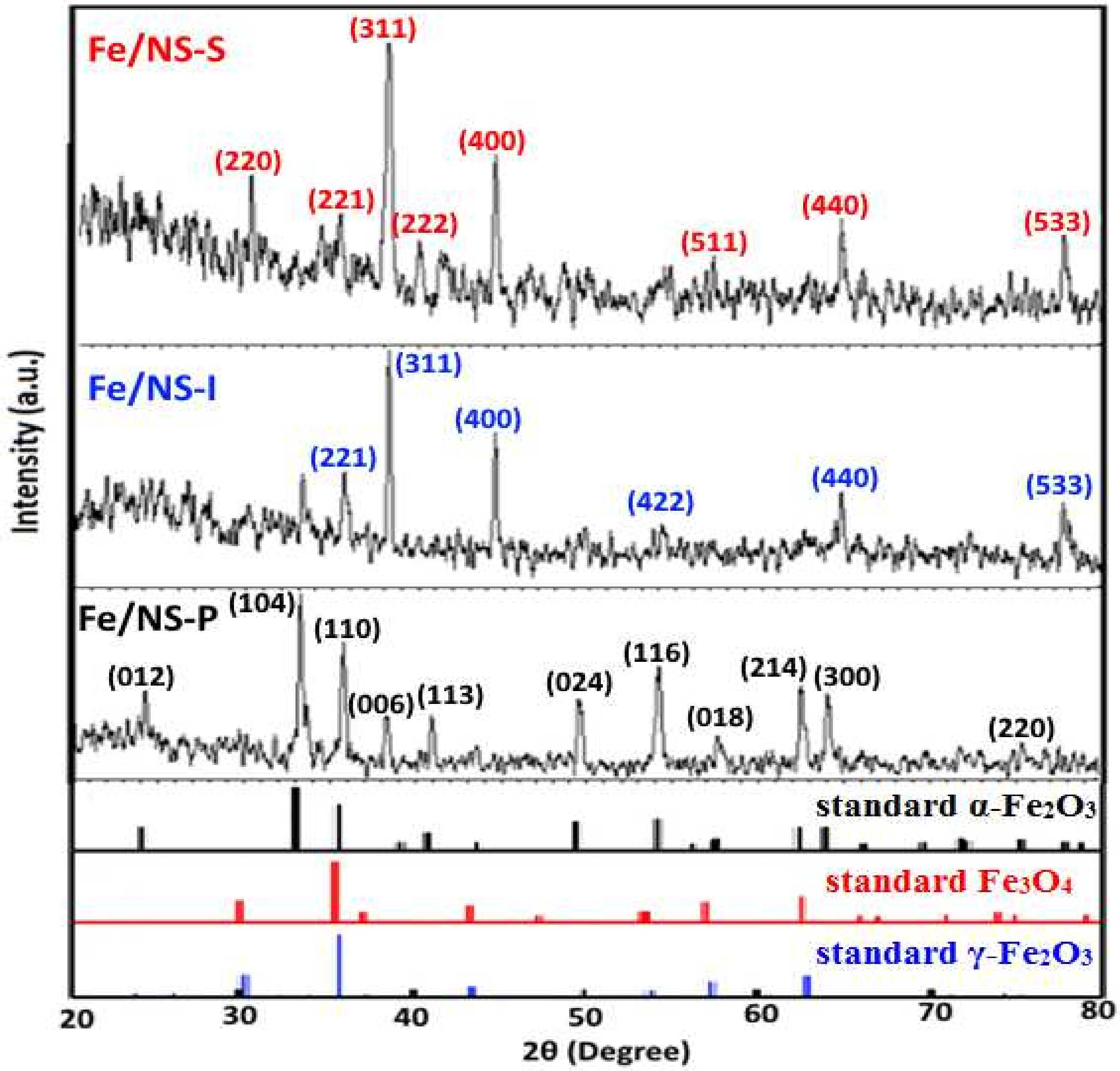

Figure 3.3. X-ray diffractograms of calcined Fe/NS-S, Fe/NS-I and Fe/NS-P catalysts, as well as iron oxide standards.

The survey XPS spectra of Fe/NS catalysts is shown in Figure3.4a. The elements C, O, Fe, and Si were detected on all catalysts, except for the XPS of Fe/NS-S catalyst which does not where the Fe 2p (710 eV) is absent (Figure 3.4a). The absence of Fe 2p spectra confirms that iron oxide nanoparticles are confined within the NS support and not at the surface [104]. The core level states at binding energies at approximately 285, 532, 710 and 103 eV are attributed to C1s, O 1s, Fe 2p and Si 2p, respectively [132]. Figure 3.4(b-c) show high resolution scans of the Fe $2p_{3/2}$ and Fe $2p_{1/2}$ peaks of the Fe/NS catalysts. One can see upon comparison of Figure 3.4b and Figure 3.4c for Fe/NS-I and Fe/NS-P catalysts have similar binding energies. The binding energies of the Fe $2p_{3/2}$ and Fe $2p_{1/2}$ core level state of the Fe/NS-P catalyst are 709.8 eV and 722.2 eV, respectively, and 709.2 and 722.2 eV for the Fe/NS-I catalyst [124, 133, 134]. Previous studies of Fe_3O_4 have reported that the Fe is characterized by the absence of a satellite peak between the Fe $2p_{3/2}$ and $2p_{1/2}$ core level states [127, 135, 136]. Therefore, the satellite peaks observed for Fe/NS-I and Fe/NS-P catalysts indicates that at the phase of the catalysts are either γ-Fe_2O_3 or α-Fe_2O_3 [127, 137].

Since the binding energies of the Fe $2p_{3/2}$ and Fe $2p_{1/2}$ of the Fe/NS-I and Fe/NS-P catalysts are essentially identical, satellite peaks are useful to distinguish between different iron oxide phases [129]. The satellite peaks between the Fe $2p_{3/2}$ and $2p_{1/2}$ in Fe/NS-P and Fe/NS-I were observed at 718 and 715 eV, respectively. These findings indicate that the iron oxides in the Fe/NS-I and Fe/NS-P catalysts are t γ-Fe_2O_3 and α-Fe_2O_3 phases, respectively, which is in good agreement with the literature [125, 138, 139]. The XPS analysis is in excellent agreement with the XRD analysis. We therefore have drawn the following conclusions as to the phase composition of Fe/NS catalysts prepared by the three methods as α-Fe_2O_3 /NS-P, Fe_3O_4/NS-S and γ-Fe_2O_3/NS-I.

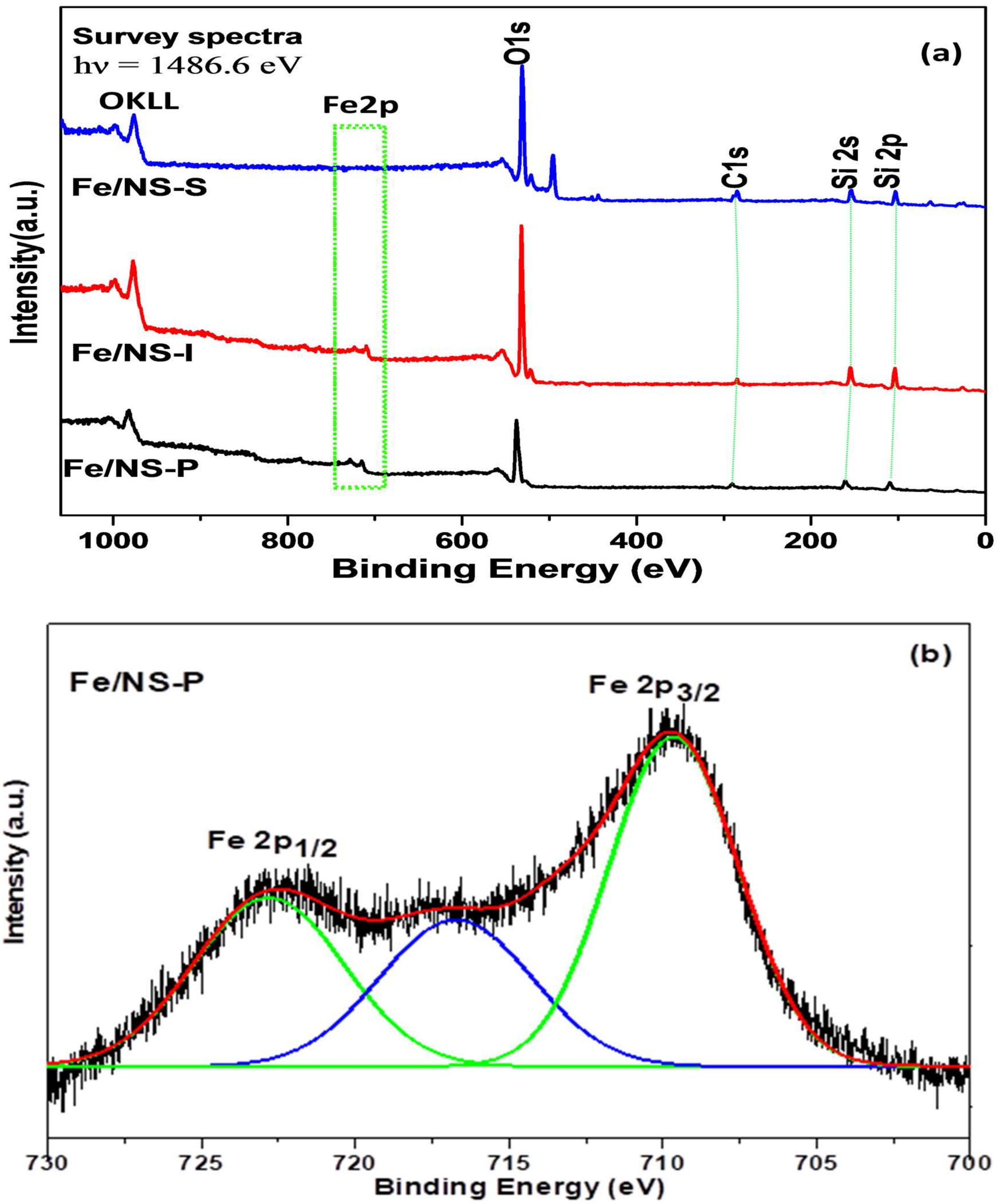
Survey spectra
hν = 1486.6 eV
(a)
OKLL
Fe2p
O1s
C1s
Si 2s
Si 2p
Fe/NS-S
Fe/NS-I
Fe/NS-P
Intensity(a.u.)
1000
800
600
400
200
0
Binding Energy (eV)
(b)
Fe/NS-P
Fe 2p3/2
Fe 2p1/2
Intensity (a.u.)
730
725
720
715
710
705
700
Binding Energy (eV)

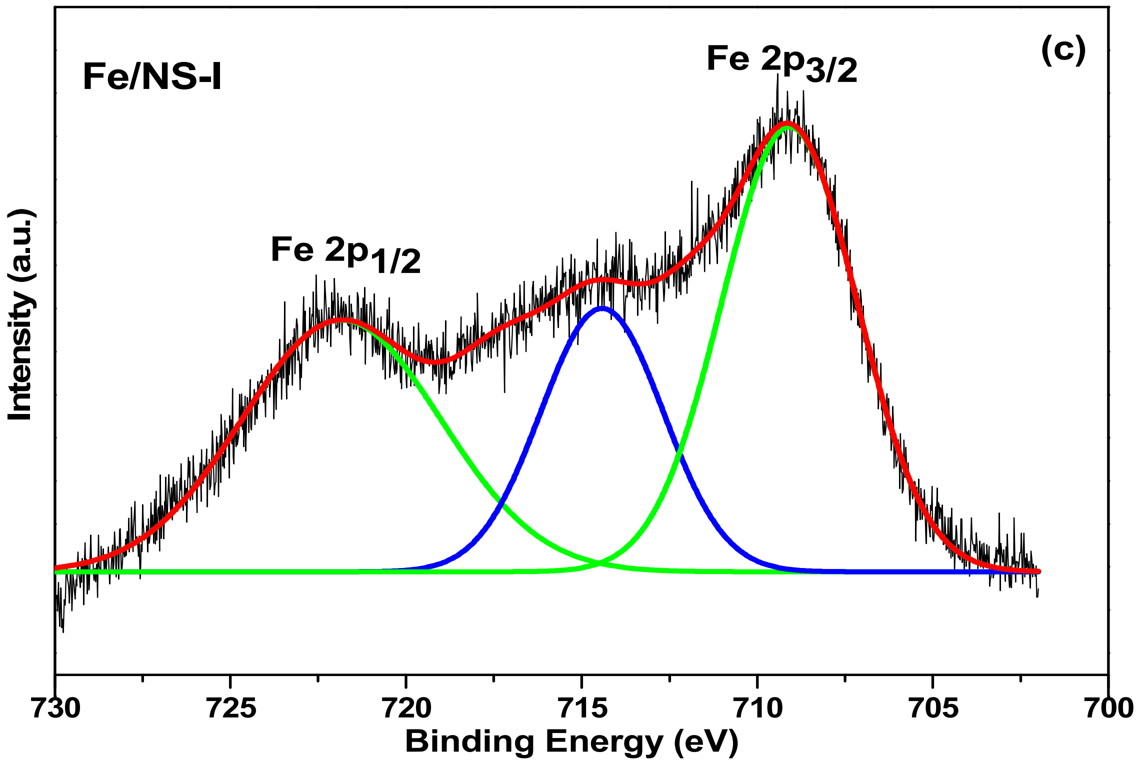

Figure 3.4. X-ray photoelectron spectra (XPS) of (a) Fe/NS catalysts and high resolution spectra of the Fe 2p core level state of (b) Fe/NS-P and (c) Fe/NS-I catalysts.

FTIR spectroscopy was performed to determine the characteristic bonding with the NS and the iron oxide nanoparticles, as well as the presence of molecular species bonded to the surfaces of the catalysts NS (Figure 3.5). It was found that all catalysts and virgin NS had characteristic peaks of SiO_2 bonds at approximately 1090 cm^{-1}, 813 cm^{-1} and 460 cm^{-1} , which can be attributed to Si–O–Si stretching, Si–O and O-Si-O bending vibrations, respectively, which is in good agreement with the literature [102-104]. In addition, the absorption bands at approximately 2975 cm^{-1} and between 1410 -1460 cm^{-1} are related to C-H stretching and bending vibrations, respectively. The bands at approximately 3443 and 1637 cm^{-1} can be attributed to the H-O-H stretching and vibration of hydrogen bonded surface silanol groups and physically adsorbed water, respectively [104-106]. In Figure 3.5a, b and c, the absorption bands of Fe–O bond were observed at approximately 588 cm^{-1} and are in good agreement with the literature [104, 106, 140, 141].

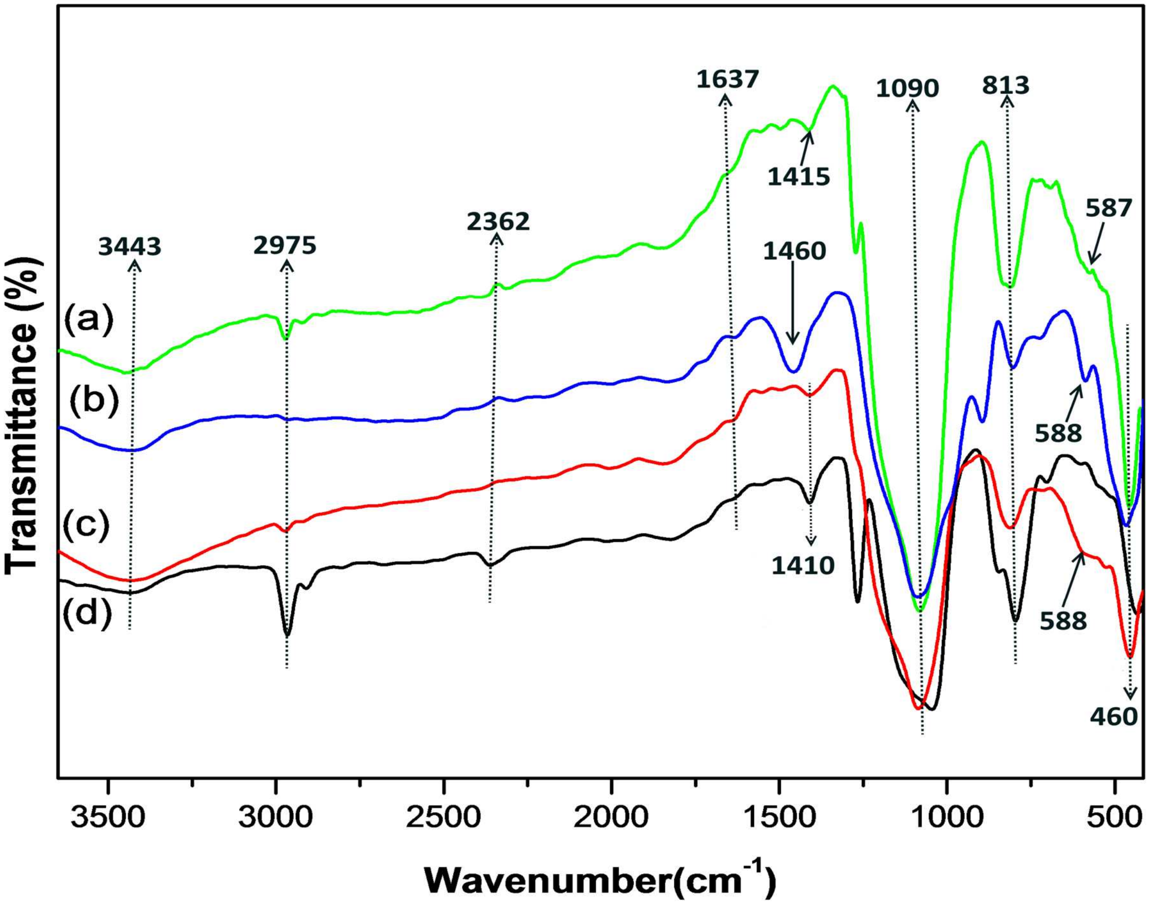

Figure 3.5. FTIR spectra of (a) Fe/NS-P; (b) Fe/NS-S; (c) Fe/NS-I; (d) virgin NS.

TGA was carried out to determine the thermal stability of the calcined catalysts and NS. The TGA thermograms of virgin NS and calcined NS (at 600 °C for 4h), Fe/NS-I, Fe/NS-P, Fe/NS-S catalysts are shown in Figure 3-6. The virgin NS showed a transition at 420 ^{o}C with about 36% total weight loss and this phenomenon is currently under investigation. The calcined NS and Fe/NS catalysts showed a total weight loss of approximately 5.0 % and 2.8%, respectively at 800 ^{o}C. This small weight loss is probably due to evaporation of adsorbed material on the NS and Fe/NS catalysts [106, 142]. Additionally, the weight loss was observed above 600 ^{o}C and can be attributed to complete removal of material during calcination. The TGA results of the Fe/NS catalysts showed no significant decomposition until 800 ^{o}C, which clearly implies that the Fe/NS catalysts have good thermal stability.

The BET surface area of virgin NS, calcined NS and Fe/NS catalysts were determined. The surface area of virgin NS was 302 m^2/g and upon heating to 600 ^{o}C the surface area decreased to 185 m^2/g and a corresponding 36% weight loss. All three Fe/NS catalysts had a reduced surface area compare to the virgin and heated NSs. The Fe/NS-I catalyst had the highest area of 127m^2/g, while the Fe/NS-S and Fe/NS-P had surface areas of 76 m^2/g and 74m^2/g, respectively. The calcination of NS above 600°C showed a significant decrease in surface area of 39%. Also, examination of Figure 3.6 shows that the incorporation of Fe on NS significantly decreases the surface area by approximately 75% for both Fe/NS-P, Fe/NS-S catalysts and 58% for the Fe/NS-I catalyst, as compared to 38% for unincorporated and calcined NS. This suggests that the Fe nanoparticles nucleate within the pores of the NS.

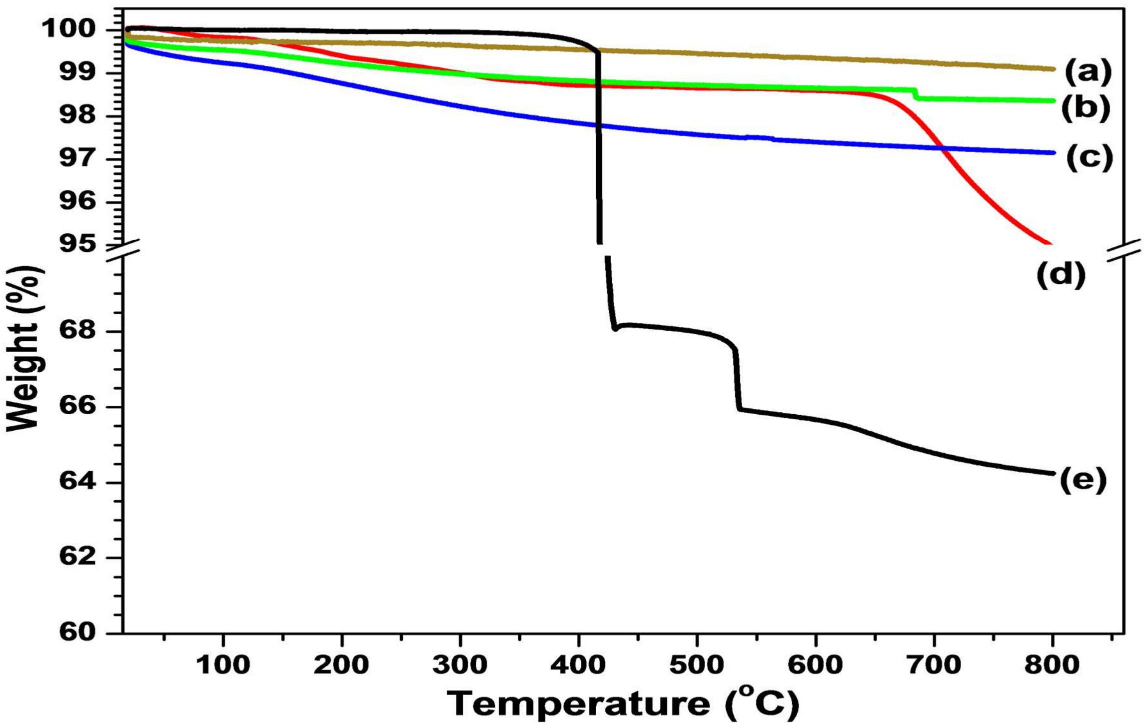

Figure 3.6. TGA thermograms of (a) Fe/NS-S, (b) Fe/NS-P, (c) Fe/NS-I catalysts, (d) virgin NS and (e) calcined NS.

3.4.2 H_2-TPR and CO-TPR

The catalytic activity of the iron oxides depends on the activation agent (e.g., H_2, CO) and activation temperature used. The activation of iron oxides with either H_2, CO or H_2+CO mixture is considered to occur according to the activation scheme shown in Figure 3.7 [143, 144]. During the activation process of Fe oxides, the carburization of α-Fe_2O_3 phase in CO can be transformed to Fe carbides (Fe_xC), which are the active phase in FTS. In contrast, the activation with CO+H_2 mixture can cause conversion to Fe carbide (Fe_xC) and α-Fe, while the reduction of α-Fe_2O_3 with H_2 is to α-Fe, as shown in Figure 3.7.

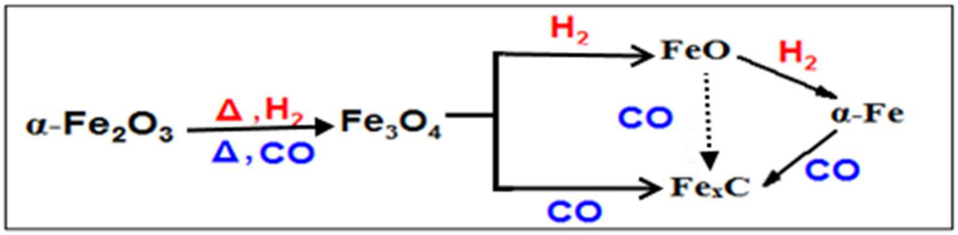

Figure 3.7. Schematic illustration of the activation of iron oxides using H_2 or CO.

The H_2 reduction temperature profile of the three calcined catalysts (Fe/NS-I, Fe/NS-P and Fe/NS-S) and Fe_2O_3 have been determined by H_2-TPR (Figure 3.8). Three peaks at 609, 708 and 844 °C are observed on the H_2-TPR profile of unsupported Fe_2O_3 nanoparticles. The first peak centered at 609 °C is attributed to the reduction of Fe_2O_3 to Fe_3O_4, whereas the second peak at 708 °C is assigned to the reduction of Fe_3O4 to FeO. The third sharp peak located at 844 °C is the final reduction step of FeO to Fe metal [145].

The reducibility of all three catalysts has been compared to pure Fe_2O_3 (Figure 3.8). The silica NS support for the Fe decorated catalysts (Fe/NS-I, Fe/NS-P and Fe/NS-S) significantly altered the H_2-TPR behavior. The profiles for Fe/NS-S and Fe/NS-P catalysts are similar and show several overlapping peaks that can be separated to three transition by peak-fitting. The minor peaks at 392 °C and 403 °C for Fe/NS-P and Fe/NS-S catalysts, respectively, are attributed to the reduction of Fe_2O_3 to Fe_3O_4. The broad peak for Fe/NS-P (440-693 °C) and Fe/NS-S (422-720 °C) are separated into two peaks. The first of these two peaks at approximately 537 °C is assigned to the reduction of Fe_3O_4 to FeO. The later peak 609-614^oC is the reduction of FeO to Fe. In contrast, the Fe/NS-I catalyst had a completely different profile from the other two and exhibits three distinctive peaks at 361, 540 and 726 ^oC, corresponding to the reduction of Fe_2O_3 to Fe_3O_4 to FeO to Fe, respectively.

Figure 3.9 shows the CO-TPR profiles of the three calcined catalysts (Fe/NS-I, Fe/NS-P and Fe/NS-S) and Fe_2O_3. During CO-TPR profiles, it is found that all of these catalysts have different carburization behavior. The TPR profiles of Fe_2O_3 is characterized by two major peaks located at 375 ^oC and 489 ^oC, which can be ascribed to the reduction of Fe_2O_3 to Fe_3O_4 and the carburization of Fe_3O_4 to iron carbides [146]. For Fe/NS-I and Fe/NS-P catalysts, the CO-TPR profiles of these catalysts show two reduction/carburization regions in the temperature range of 380-463 ^oC and 380-598 ^oC, respectively. Whereas, the CO-TPR profiles of Fe/NS-S catalyst exhibits no obvious peaks and instead has a broad single reduction/carburization peak centered at 354 °C. The CO-TPR results of Fe/NS-S catalyst are consistent with the results of XPS data, where both indicate that there is a strong interaction between the Fe and NS support. It is well known that a strong metal-support interaction can significantly suppress the carbonization of catalyst [146, 147]. Comparison of the CO reduction of Fe_2O_3 with the Fe/NS catalyst demonstrates that the addition of NS support significantly influences the carbonization temperature of all three catalysts.

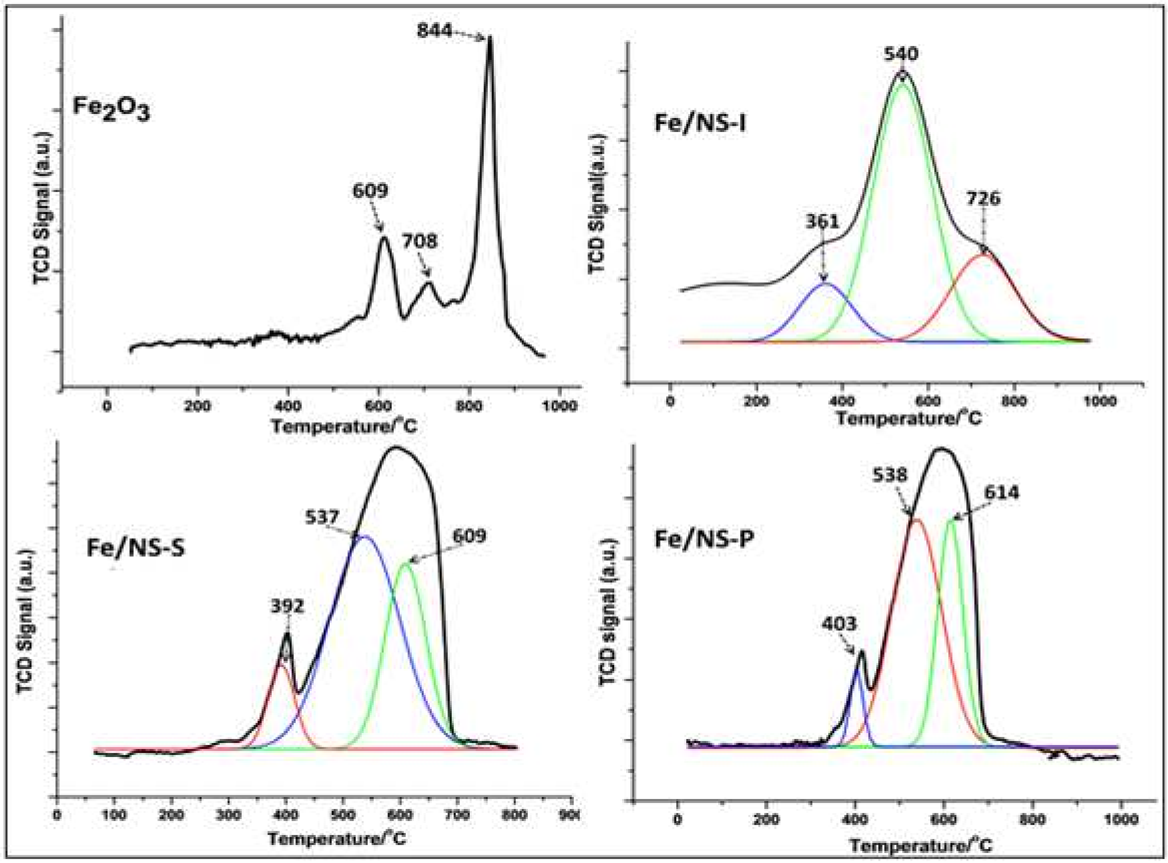

Figure 3.8. H_2-TPR profiles of calcined unsupported Fe_2O_3 and Fe/NS catalysts.

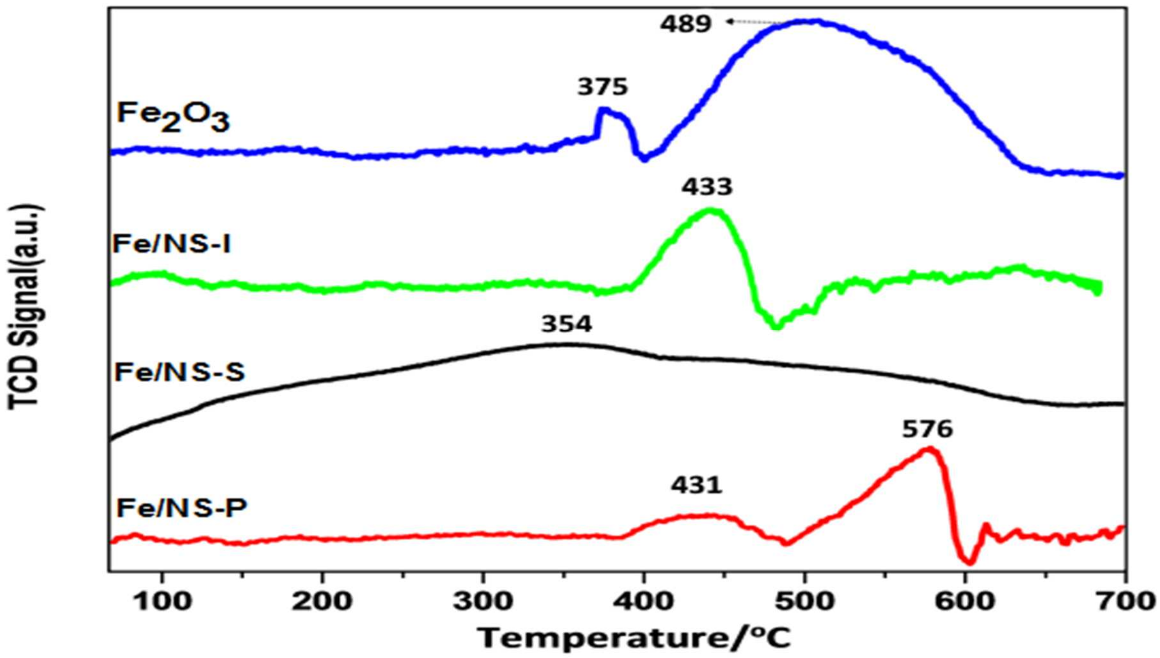

Figure 3.9. CO-TPR profiles of calcined unsupported Fe_2O_3 and Fe/NS catalysts.

3.4.3 Catalyst Evaluation

The Fe/NS catalysts were reduced with three different activation agents (i.e., CO, H_2 and H_2+CO mixture) to look at their effects of FTS efficiency. The catalytic performances of the Fe/NS catalysts were carried out in a quartz fixed-bed micro-reactor at 270 °C with a H_2/CO ratio of 2 for 12 h. The condensable liquid products were analyzed by GC-MS and the non-condensable gases (CO, CO_2, H_2, N_2 and CH_4) were analyzed by GC. The FTS activity measured by CO conversion and hydrocarbons distribution results are summarized in Table 3.2. The CO conversions and hydrocarbon distributions are affected by both the preparation and activation methods. The Fe/NS-I catalyst reduced by CO gives the highest CO conversion of 76.6% and selectivity in the

C_6-C_{14} hydrocarbon range. This catalytic performance could be attributed to the following possibilities: (i) according to TEM images in Figure 3.2c, the dispersion of iron particles in The Fe/NS-I catalyst is more homogeneous on the surface of NS support, which should be favorable for the CO conversion, (ii) the possibility of the formation of the most active iron carbide phases for FTS (χ-Fe_5C_2) or (θ-Fe_3C) after activation by carburization and/or during FTS reaction. Although this study does not provide any evidence that can explain the existence of these carbides after activation and FTS reaction, this is in line with the literature [116, 148, 149]. Several research groups have reported that CO-reduced iron catalyst gives higher CO conversion activity and high selectivity than the other reduction methods [88, 150]. Unlike the CO reduced Fe/NS-I catalyst, both H_2 reduced Fe/NS-P and Fe/NS-S catalysts give maximum CO conversions of 43.2% and 46.7%, respectively. The FTS activity results are in agreement with XPS, CO-TPR and crystallographic data. The results of XPS and CO-TPR of Fe/NS-S catalyst exhibit a weak signal for the existence of both iron particles on the surface of the catalyst and carbides during CO activation. This low iron content may cause a lower overall CO conversion for this catalyst. It also worth noting, the size of the iron particles affects the activity of the catalyst. It has been reported that small iron particles exhibit a lower selectivity towards long chain hydrocarbons [151]. In this study, the crystallographic measurements of Fe/NS-S catalyst had a particle size of 1.7-2.6 nm, which is smaller than that Fe/NS-I and Fe/NS-P catalysts. Therefore, the influence of iron particle size of Fe/NS-S catalyst on the performance of FT reaction is clearly evident.

Figures 3.10 and 3.11 show the H_2 and CO conversion results of Fe/NS-I, Fe/NS-S and Fe/NS-P reduced in H_2, CO or H_2+CO mixture. The highest CO conversion (76.6%) is for the Fe/NS-I catalyst reduced by CO. This catalyst also shows a significantly higher FT activity when reduced by either H_2, CO or H_2+CO mixture, as compared to those of the catalysts prepared by precipitation and modified sol-gel methods. The catalytic activity and selectivity of Fe/NS-I catalysts are considerably better than those obtained over Fe/NS-S or Fe/NS-p catalysts. Furthermore, it is found that the Fe/NS-I catalyst reduced by CO has higher aromatic content and selectivity towards C_6–C_{14} (JP-4 jet fuel and gasoline ranges) than Fe/NS-I catalysts, which were also reduced by H_2 and H_2+CO mixture at the same reduction conditions (Figure 3.12). It is also evident from Figure 3.12 that all Fe/NS-I catalysts reduced by either H_2, CO or H_2+CO mixture don’t follow the Anderson, Schultz and Flory (ASF) distribution for the products of FTS [152]. However, gasoline range hydrocarbons increase when using the Fe/NS-I catalyst reduced by CO, whereas both Fe/NS-I catalysts reduced by either H_2 or H_2+CO mixture confined product distribution to the C_6-C_{11} range of products. Although the Fe/NS-I catalysts exhibit the highest catalytic activity, the activity of these catalysts in the paraffin C_6-C_{14} range is relatively low. Furthermore, branched paraffin and olefins products over Fe/NS-I catalysts reduced by H_2 and CO are more favorable than n-paraffin and n-olefins. Detailed composition of the condensed liquid products determined by GC-MS and the resulting chromatograms are given in Tables 3-3 through 3.11.

Comparing the selectivity and distribution of all Fe/NS catalysts reduced by either H_2, CO or H_2+CO mixture that the Fe/NS-I catalyst reduced by CO shows low selectivity to methane and the highest distribution of products to C_6-C_{14} of 56.9%. Moreover, the Fe/NS catalysts reduced by CO produces liquid hydrocarbons in C_6-C_{14} contained 78.7% aromatics, 11.9% branched olefins and 4.4% branched paraffins. GC-MS analysis of liquid products in C_6-C_{14} range synthesized at reaction temperature 270 °C and $H_2/CO = 2$ is also presented in Table 3.2. The paraffins in the C_6–C_{14} range are almost all but absent in all the Fe/NS catalysts except when the Fe/NS-I catalyst is reduced by CO.

The major hydrocarbon products in the C_6–C_{14} range for all catalysts are in the following order: aromatics > branched olefins > branched paraffins (including cycloalkanes). The reason for high aromatic content and decreasing the amount of paraffins may be due to the use of Fe/NS catalysts under a relatively high temperature FTS process (270 ^oC), as well as the H_2/CO ratio has a significant effect on the product distribution and the FT [153, 154]. The formation of C_6-C_{14} aromatic hydrocarbons by Fe/NS-I catalysts reduced by CO and H_2 are mainly composed of mono-nuclear aromatics that include xylenes (*m, o* and *p*), toluene and alkyl benzenes (ethyl benzene, trimethyl, tetramethyl, and 1-ethyl-4-methylbenzenes, etc). In addition, there are several classes of hydrocarbons formed by Fe/NS-I catalysts reduced by CO and H_2, among which di- and poly-nuclear aromatics such as naphthalene and alkyl-naphthalene isomers. Several studies have been performed to investigate the effect of Fe-based catalysts on FT products distribution. The results obtained herein are in general agreement with Yan et al [152] in that the higher reaction temperature over Pd-promoted Fe/HZSM-5 catalyst leads to the higher selectivity toward aromatics in the liquid hydrocarbon products. Also Qian et al [155] found that the Fe/SiO_2 catalysts reduced in syngas at different temperatures showed high activity and product distribution C_{9+} decreased with an increase in activation temperature. The CO conversion as a function of reaction time for Fe/NS-I catalyst at 270 ^oC for 12 h and activated by H_2, CO or H_2+CO mixture is shown in Figure 3.13. CO conversion in Fe/NS-I catalyst is relatively constant and reaches its highest activity after almost 4 hours into the reaction. It can be concluded that no significant deactivation in catalytic stability has been observed during the 12 h run of the FT reaction.

Table 3.2. Catalytic performance and major components of synthesized liquid F-T fuel over Fe/NS FTS catalysts

Catalyst	**Fe/NS-I**			**Fe/NS-P**			**Fe/NS-S**		
Activation gas	H_2	CO	H_2/CO	H_2	CO	H_2/CO	H_2	CO	H_2/CO
CO Conversion (%)	73.3	76.6	35.3	43.2	22.4	5.2	46.7	21.3	6.4
H_2 Conversion (%)	58.6	68.3	25.6	29.2	18.5	36.2	60.2	53.4	28.9
Products Selectivity (%)									
CO_2 select.(%)	18.9	0.6	1.2	0.2	11	5.8	1.5	1.3	14.7
CH_4 select.(%)	11.8	13.4	21.3	15.6	16.4	23.6	15.2	24.2	26.6
Product distribution (Mol.%)									
C_6-C_{14} aromatics	50.2	56.9	16.2	16.7	8.4	12.1	25.0	11.2	11.1
benzene	11.2	5.0	7.4	3.2	2.9	3.2	5.2	3.9	4.2
toluene	16.6	12.8	6.9	6.8	1.8	4.9	7.3	3.1	4.3
xylenes	7.2	3.6	1.9	2.6	0.8	2.3	3.8	--	0.5
alkylbenzenes	5.4	10.7	--	3.3	1.0	1.7	1.9	0.9	2.1
indane	--	0.8	--	0.8	--	--	--	--	--
indene	--	1.4	--	--	--	--	1.3	1.2	--
naphthenes	--	2.4	--	--	0.8	--	--	1.1	--
alkylnaphthenes	3.1	3.2	--	--	0.4	--	0.6	0.5	--
others	6.4	4.9	0	0	0	0	4.9	0.5	0
total aromatics	49.9	44.8	16.2	16.7	7.7	12.1	25.0	11.2	11.1
branched Paraffin	--	5.3	--	--	--	--	--	--	--
branched olefins	0.3	6.8	--	--	0.7	--	--	--	--

(--) indicates not identified by GC-M

Table 3.3. The FT products identified by GC-MS for Fe/NS-I catalyst reduced by CO at a temperature of 270 ^{o}C, and atmospheric pressure and H_2/CO =2.

Retention time (min)	Identified compounds	Mol(%)	M+ (m/z)
2.64	Benzene	5.02	78
4.34	Toluene	12.8	92
4.88	1-octene	2.33	112
5.26	2-octene	0.55	112
6.55	3,4-Dimethyl-1-octene	0.83	140
6.71	Ethylbenzene	2.78	106
6.94	o-Xylene	3.58	106
7.58	1-methylpentyl cycloprpane	4.05	126
8.02	Trans- 4 –nonene	0.48	126
9.44	n-Propylbenzene	1.37	120
9.70	1 -ethyl-3-methylbenzen	2.20	120
10.70	1 -ethyl-2-methylbenzen	1.64	118
10.81	Indane	0.81	118
11.08	Cis-3-Decene	0.61	140
12.22	Indene	1.40	116
12.60	Butylbenzene	0.67	134
13.69	2,6,Dimethyl-7-octene	0.69	140
14.11	Cyclopropane,1-pentyl-2propyl	0.41	154
15.10	1,2-Dimethyl-4-ethylbenzene	0.40	132
15.39	1-methyl-4-(1-propynyl)benzene	1.60	130
15.56	2-Methylindene	1.40	130
16.40	Naphthalene	2.40	128
16.64	3-methy!-1-heplanol	0.35	130
17.04	5-Dodecene	0.31	168
17.26	2 4-dimethyl-1-heptanol	0.17	144
18.56	1,2-dihydro-4-methylnaphthalene	0.55	144
18.71	1-methylnaphthalene	0.50	142
19.66	n-Decane	0.18	142
19.80	6-Tridecene	0.24	182
19.98	2-methylnaphthalene	0.40	124
20.06	3,7-Dimethyl-1-octene	0.15	140
21.79	Phenylbenzene	0.13	154
22.08	5-tetradecene	0.70	198
22.16	1-ethylnaphthalene	0.80	156
22.29	6-ethyl-2-methyl-decane	0.26	184
22.43	1,7-Dimethylnaphthalene	0.68	156
22.68	3,7-Dimethyl-1-octene	0.09	140
22.91	2,6-Dimethylnaphthalene	0.08	156
23.32	2,3-Dimethylnaphthalene	0.10	156
23.99	1-(4-methylpent-3-enyl)-benzene	0.15	172
24.45	Acenaphthene	0.43	154
24.53	1-Propylnaphthalene	0.17	170
24.68	Diphenylmethane	0.17	168
24.78	2,7,10-Trimethyldodecane	0.18	212

24.91	Naphthalene, 2-(1-methylethyl)	0.60	170
25.11	1-isopropyl-naphthalene	0.27	168
26.79	Phenalene	0.06	166
27.12	Benzene,[1-(2,4-cyclopentadien-1-ylidene)ethyl]	0.39	168
27.22	4-Methylbiphenyl	0.43	168
29.37	4-methyl-9H-fluorene	0.13	180
31.15	phenanthrene	0.23	178

Table 3.4. The FT products identified by GC-MS for Fe/NS-I catalyst reduced by H_2 at a temperature of 270 ^{o}C, and atmospheric pressure and H_2/CO =2.

Retention time (min)	Identified compounds	Mol(%)	M+ (m/z)
2.65	Benzene	11.13	78
4.30	Toluene	16.6	92
6.52	Ethylbenzene	1.62	106
6.75	m-Xylene	5.37	106
7.41	p-Xylene	1.87	106
9.47	isopropylbenzene	1.29	106
10.44	1-ethyl-3-methyl-benzene	0.58	120
11.72	cyclopropyl benzene	0.95	118
11.98	1-Propenylbenzene	0.79	116
13.28	Methyl-4-(2-propenyl)-benzene	0.25	132
14.84	2,4-dimethylethylbenzene	0.38	132
15.15	1-methyl-1,2-propadiene benzene	0.65	130
15.32	1-methyl-4-(1-propynyl)benzene	0.43	130
16.15	1-Methyl-1H-indene	4.16	128
19.26	1-methylnaphthalene	2.55	142
19.72	1,6-Methano[10]annulene	0.80	142
21.91	1-ethylnaphthalene	0.18	156
22.18	2,6-Dimethylnaphthalene	0.35	156
22.53	6-ethyl-2-methyl-decane	0.25	184

Table 3.5. The FT products identified by GC-MS for Fe/NS-I catalyst reduced by CO/H_2 at a temperature of 270 ^{o}C, and atmospheric pressure and H_2/CO =2.

Retention time (min)	Identified compounds	Mol(%)	M+ (m/z)
2.64	Benzene	7.4	78
4.34	Toluene	6.92	92
6.72	m-Xylene	0.69	106
6.95	o-Xylene	1.11	106

Table 3.6. The FT products identified by GC-MS for Fe/NS-P catalyst reduced by CO at a temperature of 270 ^{o}C, and atmospheric pressure and H_2/CO =2

Retention time (min)	Identified compounds	Mol(%)	M+ (m/z)
2.60	Benzene	2.95	78
4.31	Toluene	1.77	92
6.64	Ethylbenzene	0.34	106
6.86	m-xylene	0.77	106
12.15	1 -ethyl-4-methylbenzen	0.62	116
16.33	Naphthalene	0.80	128
19.48	1-methylnaphthalene	0.35	142
19.94	1,6-methano[10]annulene	0.16	142
22.21	2,6-Dimethylnaphthalene	0.35	156
22.60	6-ethyl-2-methyl-decane	0.16	184

Table 3.7. The FT products identified by GC-MS for Fe/NS-P catalyst reduced by H_2 at a temperature of 270 ^{o}C, and atmospheric pressure and H_2/CO =2

Retention time (min)	Identified compounds	Mol(%)	M+ (m/z)
2.62	Benzene	3.22	78
4.31	Toluene	6.74	92
6.68	Ethylbenzene	1.32	106
6.92	m-xylene	1.47	106
7.60	p-xylene	1.1	106
9.67	1 -ethyl-3-methylbenzen	1.4	120
11.94	Indane	0.79	118
13.50	2,4-dimethylethylbenzene	0.56	132

Table 3.8. The FT products identified by GC-MS for Fe/NS-P catalyst reduced by CO/.H2 at a temperature of 270 ^{o}C, and atmospheric pressure and H_2/CO =2

Retention time (min)	Identified compounds	Mol(%)	M+ (m/z)
2.65	Benzene	3.15	78
4.33	Toluene	5.0	92
6.73	Ethylbenzene	1.65	106
6.95	m-Xylene	1.16	106
7.63	P-Xylene	1.08	106

Table 3.9. The FT products identified by GC-MS for Fe/NS-S catalyst reduced by CO at a temperature of 270 °C, and atmospheric pressure and $H_2/CO = 2$

Retention time (min)	Identified compounds	Mol(%)	M+ (m/z)
2.62	Benzene	3.91	78
4.31	Toluene	3.13	92
6.90	Ethylbenzene	0.9	106
12.21	Indene	1.15	116
16.37	Naphthalene	1.14	128
19.52	1-methylnaphthalene	0.47	142
19.97	1,6-methano[10]annulene	0.17	142
26.78	Phenalene	0.26	166

Table 3.10. The FT products identified by GC-MS for Fe/NS-S catalyst reduced by H_2 at a temperature of 270 °C, and atmospheric pressure and $H_2/CO = 2$

Retention time (min)	Identified compounds	Mol(%)	M+ (m/z)
2.60	Benzene	5.19	78
4.31	Toluene	7.27	92
6.64	Ethylbenzene	0.68	106
6.87	m-xylene	2.34	106
7.53	p-xylene	1.50	106
9.62	1,2,3-Trimethylbenzene	0.45	120
10.61	1-Propenylbenzene	0.75	116
12.16	Indene	1.33	116
15.34	1-methylindene	0.66	130
16.35	1-methyl-1H-indene	1.81	128
19.48	1,6-methano[10]annulene	1.25	142
19.92	1-methylnaphthalene	0.39	142
22.39	1,2-Dimethylnaphthalene	0.12	156
23.26	1,5-Dimethylnaphthalene	0.12	156
26.74	9H-fluorene	0.39	166
26.76	Phenalene	0.37	166
29.31	4-methyl-9H-fluorene	0.12	180
31.07	phenanthrene	0.25	178

Table 3.11. The FT products identified by GC-MS for Fe/NS-S catalyst reduced by H_2/CO at a temperature of 270 °C, and atmospheric pressure and $H_2/CO = 2$

Retention time (min)	Identified compounds	Mol(%)	M+ (m/z)
2.61	Benzene	4.21	78
4.32	Toluene	4.27	92
6.94	Ethylbenzene	1.41	106
7.14	p-Xylene	0.47	106
10.45	1-ethyl-3-methyl-benzene	0.66	120

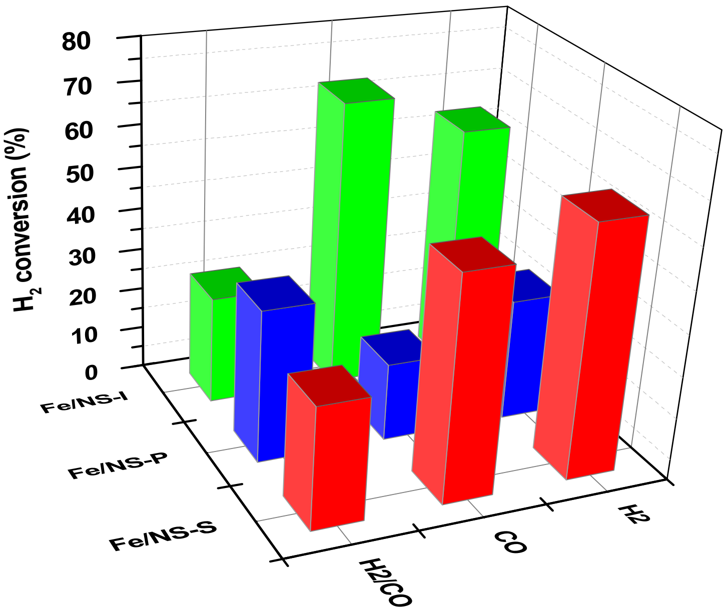

Figure 3.10. H_2 conversion % for Fe/NS catalysts activated by H_2, CO, & H_2/CO

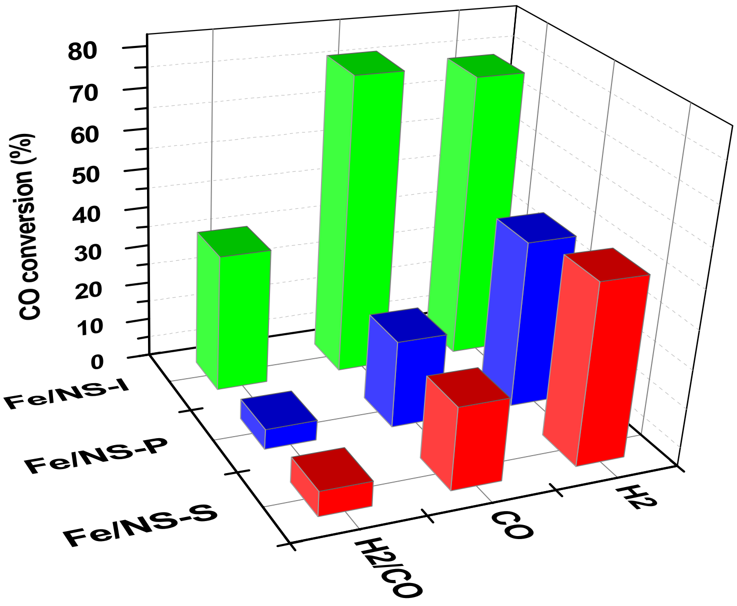

Figure 3.11. CO conversion (%) for Fe/NS catalysts activated by H_2, CO and H_2+CO.

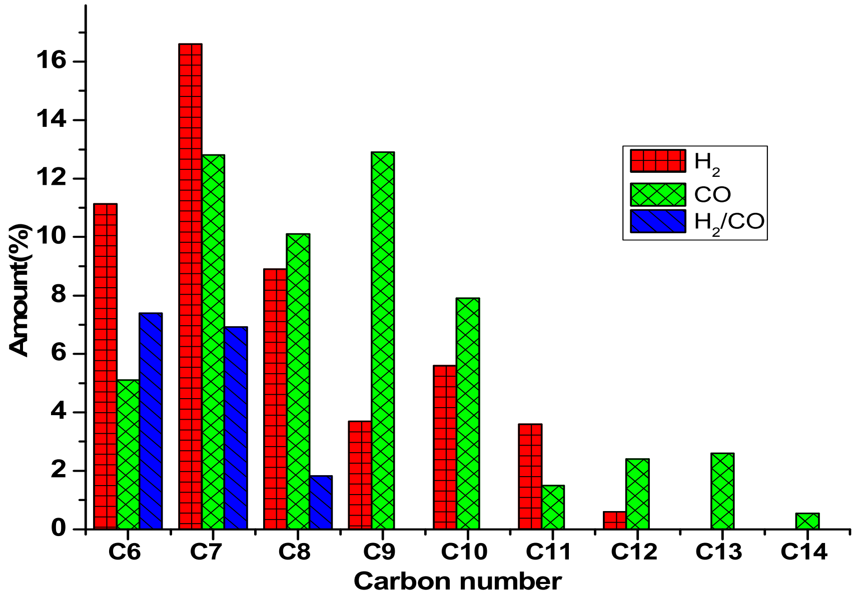

Figure 3.12. Product distribution after 12h for Fe/NS-I catalyst (activated by H2, CO & H2/CO).

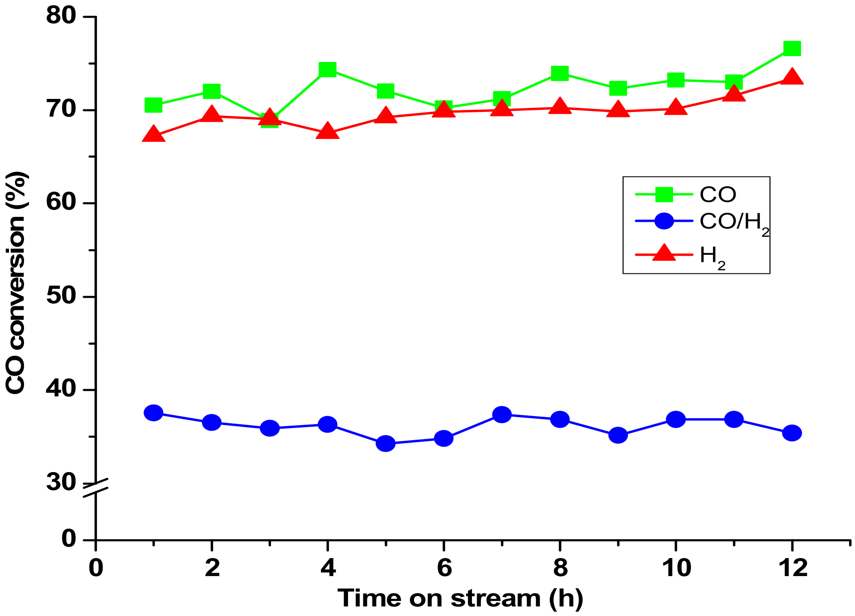

Figure 3.13. CO conversion with time on stream over Fe/NS-I catalyst activated by H_2, CO and H_2/CO.

3.5 Conclusion

Three Fe catalysts supported on NS with different particles size and Fe phases have been successfully synthesized using three different methods, i.e. incipient wetness impregnation, precipitation and modified sol-gel and activated by H_2, CO or H_2+CO mixture and subsequently studied. TEM imaging of the catalysts have shown that the particle size and phase composition of nanostructure of the Fe/NS catalysts can be controlled by the chemistry of preparation process. Moreover, the positions of diffraction in the XRD of Fe/NS-I, Fe/NS-P and Fe/NS-S catalysts are consistent with the standard structure of diffraction data for γ-Fe_2O_3, α-Fe_2O_3 and Fe_3O_4, respectively. The influence of preparation and activation methods on the catalytic performance of Fe/NS catalysts for higher liquid hydrocarbons synthesis has been investigated. Based on the results of our studies, we conclude that the Fe/NS-I catalyst prepared using wetness impregnation and activated by CO has highest activity and its selectivity falls within the range of gasoline C_6–C_{14}. By contrast, the other Fe/NS catalysts showed poor catalytic activity and selectivity when the Fe/NS catalysts is prepared using precipitation and modified sol-gel methods. We conclude that the optimal preparation and activation methods to reach the highest catalytic activity and selectivity toward light hydrocarbons are with the Fe/NS-I catalyst activated by CO. In addition, the Fe/NS-I catalysts selectivity favor aromatics in the C_6–C_{14} range. The FTS products mainly consists of a high content of aromatics and low contents of n-olefins and n-paraffins.

Our findings could have implications for designing a new family of catalysts with improved catalyst for direct conversion of syngas to a wide range of aromatic hydrocarbons.

CHAPTER 4: ENHANCEMENT OF THE CATALYTIC PERFORMANCE OF SILICA NANOSPRINGS (SN)-SUPPORTED IRON CATALYST BY PROMOTING COPPER, MOLYBDENUM, COBALT AND RUTHENIUM FOR FISCHER-TROPSCH SYNTHESIS

4.1 Abstract

Fe/NS catalyst and promoted Fe/NS catalysts with the different metals such as Co, Mo, Cu and Ru were synthesized via impregnation method and employed to investigate effects of on physico-chemical properties and catalytic behavior of Fe/NS catalyst during the Fischer-Tropsch synthesis (FTS). The physico-chemical properties of the prepared catalysts were characterized before the FT reaction by various techniques, such as BET surface area, X-ray diffraction (XRD), transmission electron microscopy (TEM), energy dispersive X-ray spectroscopy (EDS), temperature programmed reduction (H_2-TPR), X-ray photoelectron spectroscopy (XPS), fourier transform infrared spectroscopy(FTIR) and thermogravimetric analysis (TGA). The FTS performance of the prompted catalysts was examined in a quartz fixed-bed microreactor (H_2/CO of 2:1, 230 ^{o}C and atmospheric pressure) and the products trapped and analyzed by GC-TCD and GC-MS to determine CO conversion and reaction selectivity. The characterization results obtained indicated that the promotion of Fe/NS catalyst with Co, Mo, Cu and Ru oxides enhanced the catalytic activity of Fe/NS catalyst. The catalytic performance over Ru-Fe/NS, Co-Fe/NS, Mo-Fe/NS and Cu-Fe/NS catalysts at the same

conditions showed that Co conversion were 93.3%, 43.6%, 82.4% and 56.3%, respectively. The C_6-C_{16} liquid hydrocarbon selectivity were 41.1%, 30.1%, 25.4% and 33.8% of which were olefins. The addition of promoters led to the increase the selectivity towards olefins instead of aromatics over unpromoted Fe/NS catalyst. Finally, it was found that the Ru, Co, MO and Cu promoters proved to have the significant effect on selectivity towards desired products namely paraffins and olefins.

4.2 Introduction

Fischer-Tropsch synthesis (FTS) has been recognized as one of the most promising alternative catalytic technologies in converting syngas (CO and H_2) derived from the gasification of coal, natural gas and biomass into liquid transportation hydrocarbon fuels and industrial chemicals. Consequently, selecting and modifying the appropriate catalyst is an important factor in the context of FT process. Among the most active metals for FTS, Fe and Co based catalysts are the most commonly used in FTS industrial applications because of their high activity, low methane selectivity and low cost as well as high water gas shift (WGS) activity [156]. Fe-based FTS catalysts are commercial used to produce light olefins or oxygenated hydrocarbons. However, hydrocarbon distribution of FT liquids produced depends upon catalyst specifications (e.g., promoters, support, etc.) and processes conditions (e.g., reactors, temperature and reaction pressure, activation and preparation methods, etc.).

From earlier studies, the FT reaction over Fe/NS catalyst activated by CO showed a high selectivity toward aromatic formation (gasoline) and low selectivity for n-olefins and n-paraffins (jet and diesel fuels) [157]. Although there are many positive sides of Fe–based catalysts, there were also some technical challenges that still need to be overcome including catalyst deactivation (iron oxidation during FTS due to the high reactor water partial pressures) and control of product selectivity [158-160]. In order to find efficient ways to overcome these challenges, many attempts have been done on some chemical parameters of FTS that have potential influences on FT process. Among these parameters is the addition of transition metal oxide promoters that play an important role in influencing the physico-chemical properties (e.g., stability, dispersion and rate of reducibility, etc.), catalytic activity and production selectivity of these Fe based catalyst for FTS because of the electron donation by the promoter to Fe [161, 162]. The utilization of promoters such as Mo, Cu, Co and Ru on Fe-based catalysts supported have been studied by various researchers [161, 163, 164]. Feyzi et al. [161] investigated the influence of Fe–Co/SiO_2 catalyst on the FTS performance. It was found that the catalyst had higher CO conversion (65.8 %) and selectivity (52.4 %) to form C_5–C_{12} products. Other studies have been performed on Cu (also known as reduction promoter) promoted Fe catalysts. Among them, Tasfy et al.[165], Wan et al.[164] and Bukur et al. [166] have shown that the addition of Cu to Fe based catalysts significantly influences their dispersion of the active phase and reduction behavior. Tasfy [9] and Wan [8] found that the addition of Cu promoter led to a reduction in catalytic activity while Bukur [10] found that Cu increased the rate of FTS reaction.

Ru has also been shown to be a good promoter for Fe catalysts by improving its stability for FTS [160]. Furthermore, addition of Ru was shown to improve resistance to deactivation by either water or oxygen during FTS [160]. However, it is also noted that much higher CO_2 and CH_4 selectivity's were observed. In the same context, the use of Mo as a promoter was reported to have improved stability and selectivity for the Fe catalyst. In previous studies [158, 163] have shown that the addition of Mo to Fe catalyst as promoter had significant impacts on the catalytic performance and catalytic properties (dispersion and stability).

As mentioned earlier, a number of studies have been conducted to verify the effects of different promoters on supported or unsupported Fe catalysts, but there have been no studies done using 1 dimensional (1D) nanostructured supports, such as silica nanosprings (NS), for FTS. Consequently, the objective of the present study is to investigate the effect of different promoters such as Mo, Cu, Co and Ru on the catalytic performance of Fe/NS catalyst for FTS and describe the features and surface properties. Fe/NS catalyst and Mo, Cu, Co and Ru promoted Fe/NS catalysts were prepared. In order to obtain optimum singly promoters affecting the FTS performance of the Fe/NS catalyst, the catalysts were comparatively characterized by various analytical techniques such as: BET, XRD, XPS, TGA-DTA, TEM, EDS, H_2-TPR, and FTIR. In addition, the CO conversion and hydrocarbon selectivity of the studied catalysts were calculated with aid of GC and GC-MS analyses.

4.3 Experimental methods

4.3.1 Catalyst Preparation

The Fe/NS (15 wt %) catalyst and all promoted catalysts M-Fe/NS (where M= 7wt % Cu, 5wt % Mo, 10wt % Co and 5wt% Ru) were prepared by the incipient wetness impregnation technique and co-impregnation technique, respectively. The loading of Fe was 15 wt % for all catalysts. The silica NS was heated at 600 ^oC for 5h to remove any residual precursors prior to deposition of active iron or promoters [157]. For 15 wt% Fe/NS catalyst preparation, $Fe(NO_3).9H_2O$ (0.25 mmol; 100 mg in 10 mL water) was added drop-wise to NS (75 mg in 15 mL ethanol) and ultra-sonicated for 15 min at 50 ^oC. The mixture was stirred at 80 ^oC for 24 h, after that the impregnated solution was dried overnight at 110 ^oC. Finally, the dried catalyst was calcined in air at 600 ^oC for 5h. Meanwhile, to prepare Cu-Fe/NS, Mo-Fe/NS, Co-Fe/NS and Ru-Fe/Ns promoted catalysts with a desired metal loading, an aqueous solution containing (0.25 mmol; 100 mg in 10 mL water) $Fe(NO_3).9H_2O$ was added to $Cu(NO_3)_2.3H_2O$ (0.9 mmol; 21mg), $Co(NO_3)_3$ $3H_2O$, $(NH_4)6Mo_7O_{24}\cdot4H_2O$, $Co(NO_3)_2\cdot6H_2O$ or $RuCl_3.H_2O$. The solutions were impregnated onto the NS (75 mg in 10 mL ethanol) by drop-wise addition and the mixture stirred for 24 h at 80 ^oC. The impregnated samples were dried at 120 ^oC overnight and subsequently calcined in air at 600 ^oC for 4 h.

4.3.2 Catalyst Characterization

H_2-TPR profiles of the prepared catalysts were performed by using a ChemiSorb 2720 instrument (Micrometrics, USA) equipped with a TCD detector. The TCD was calibrated by the reduction of CuO (20 mg, 99.99%) between 25 and 500 °C. Before running each TPR experiment, the catalyst was flushed with N_2 (30 mL/min) at 150 °C for 1 h to remove the surface impurities and then cooled down to room temperature. H_2-TPR experiments were conducted in a 10 vol. % H_2 in N_2 atmosphere. The total flow was adjusted to 30 mL/min. The temperature was ramped from room temperature to 1000 °C at a heating rate of 10 °C/min.

The SBET-specific surface area measurements of all degassed (220 °C for 30 min) catalysts (60-80 mg) were determined by an N_2 adsorption-desorption isotherm at -196 °C using a Micromeritics ChemiSorb 2720 instrument. By assuming that the iron oxide nanoparticles are spherical, the average crystallite size (d_{BET}) of iron oxides was estimated by the following equation [167-169]:

$$d_{BET} = \frac{6}{\rho\, S_{sp}} \qquad \text{(Eq. 4-1)}$$

Where d is the average crystallite in nm, ρ is the true density (ρ for iron oxide is 5.24 g/cm^3), Ssp is the specific surface area of the sample.

FT-IR spectra of the calcined catalysts (10% mixed with KBr) was recorded at room temperature in the range 480 - 3500 cm^{-1} by diffuse reflectance (5% in KBr) using a Thermo Nicolet Avatar 370 DTGS spectrometer.

X-ray diffraction (XRD) of the calcined catalysts was carried out by a Siemens D500 powder diffractometer with Cu/kα radiation (λ= 1.54 A°). The diffraction intensities were recorded from 10°- 80° (2θ value) with 0.01° step using a 1 s acquisition time per step. The average crystallite size (d_{XRD}) of iron oxides was estimated using Scherrer's equation [97]

$$d_{XRD} = \frac{0.9\,\lambda}{\beta \cos\theta} \qquad \text{(Eq. 4-2)}$$

Where d is the average crystallite in nm, 0.9 is shape factor (for spherical shape particles), λ is the wavelength of X-ray (λ = 1.54 Å), β is line broadening at half the maximum intensity (FWHM) in radians, θ is the Bragg angle.

The surface morphology of the catalysts (dispersed in ethanol and applied to a copper grid coated with carbon support film) was characterized by TEM (JEOL JEM-2010) operated at 200 kV. The iron particle size was measured on TEN images using ImageJ software. EDS analysis was conducted to study the chemical composition of promoted catalysts by using the Proza Phi-Rho-Z correction method.

Thermogravimetric (TGA) and differential thermal (DTA) anlayzes of the sample (5 mg) were carried out respectively on Perkin Elmer TGA-7 and DTA -7 instruments from 30 °C to 900 °C at 20 °C/min under N_2 (30 mL/min).

XPS experiments were recorded on a custom built ultrahigh vacuum (UHV) chamber using a dual anode X-ray lamp, XR 04-548 from PHYSICAL ELECTRONICS, and kinetic energy of the photoelectrons was measured with an EA 125 hemispherical energy analyzer with a net resolution of 25 meV. The X-ray source used was the Al-Kα line at 1486.6 eV.

4.3.3 Catalytic activation and FTS reaction test

The catalyst samples (approximately 20 mg of each calcined unprompted and promoted Fe/NS catalyst diluted with 40 mg quartz sand) were loaded into a quartz fix-bed micro-reactor (10 mm Ø x 300 mm with a "0" quartz frit connected 180 mm from the top to support the catalyst) housed in a tube furnace (25 mm Ø x 150 mm), and then reduced in H_2 (40 mL/min) in N_2 gas mixture using mass flow controllers (CG1, Dakota Instruments) (Figure 4.1). The reactor temperature was increased from room temperature to 750 ^oC for 24 h at atmospheric pressure. The activated catalyst was cooled to 175 ^oC and subsequently used for *in situ* FTS reaction. After catalyst activation, synthesis gas stream with $H_2/CO = 2$ was feed to the reactor at 230 ^oC using mass flow controllers (CG1, Dakota Instruments) and at atmospheric pressure. The FTS reaction products were collected in a three-stage impinger trap placed in a liquid nitrogen bath. The uncondensed vapor stream was collected in a TedlarTM PVF (300 × 300 mm^2) gas-sampling bag. FTS reaction was maintained for 12 h under reaction temperature of 230 ^oC. Unreacted gases and gaseous reaction products and were determined by GC-TCD (GOW-MAC, Series 350) with (i) a packed HaySep DB stainless steel column (3.3 mm Ø x 9.1 m) at 25 ^oC for CO, CO_2, H_2, N_2 and CH_4 and (ii) a packed PoraPakQ stainless steel column (3.3 mm Ø x 1.8 m) at 60^oC for C_xH_y ($x \leq$ C4)) on elution with He. The liquid products C_xH_y ($x \geq C_5$) collected were then identified by GC-MS (Fous-ISQ, ThermoScientific). Separation was achieved on a ZB5ms (0.25 mm Ø x 30 m, Phenomenex) capillary column with a temperature program of 40 ºC (1 min) ramped to 250 ºC at 5 ºC/min. Data was analyzed using the Xcalibur v2 software. The results in terms of CO conversion, selectivity, and yield of products were calculated using following method:

$$X_{CO}(\%) = \frac{(\text{n } CO\ at\ inlet)-(\text{n } CO\ at\ outlet)}{(\text{n CO at inlet})} x100 \qquad \text{(Eq. 4-3)}$$

$$X_{H2}(\%) = \frac{(\text{n } H2\ at\ inlet)-(\text{n } H2\ at\ outlet)}{(\text{n H2 at inlet})} x100 \qquad \text{(Eq. 4-5)}$$

$$X_{CO_2}(\%) = \frac{(nCO_2\ at\ outlet)}{(nCo\ at\ inlet)-(n\ CO\ at\ outlet)} x100 \qquad \text{(Eq. 4-6)}$$

$$X_{CH_4}(\%) = \frac{(\text{ n } CH_4\ at\ outlet)}{(\text{n CO } at\ inlet - \text{ n CO } at\ outlet)-(\text{n CO}_2\text{at outlet})} x100 \qquad \text{(Eq. 4-7)}$$

$$S\ C_n(\%) = \frac{n\ HC\ \ produced}{(n\ CO\ at\ inlet)-(n\ CO\ at\ outlet)} x100 \qquad \text{(Eq. 4-8)}$$

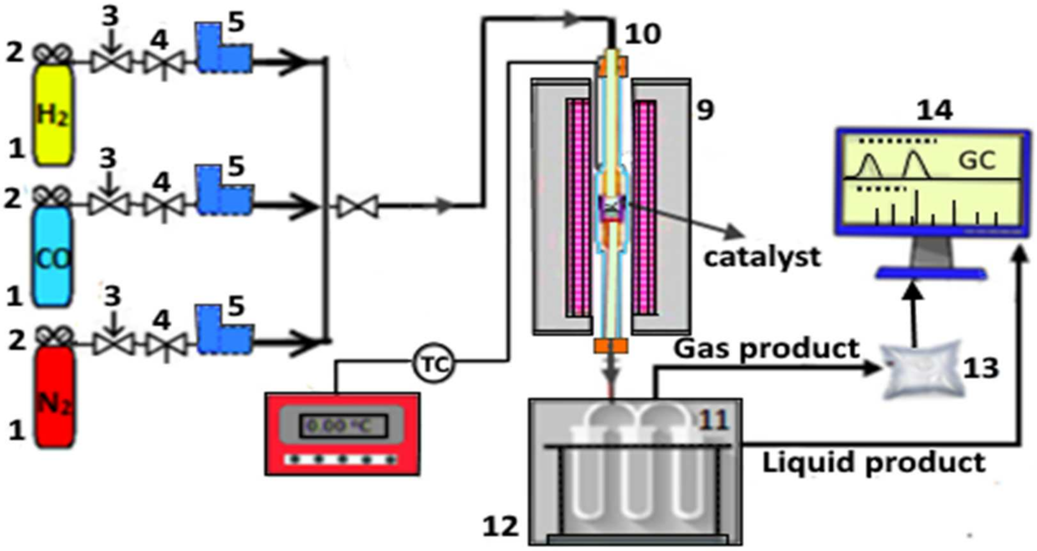

Figure 4.1. Schematic diagram of FTS apparatus used. (1) gas cylinders (H_2, CO and N_2), (2) pressure regulators, (3) needle valves, (4) valves, (5) mass flow controllers, (6) ball valves, (7) thermocouple (Type-K), (8) PID temperature controller, (9) furnace, (10) quartz tubular reactor, (11) 3- stage condenser-impinger, (12) liquid nitrogen bath (condenser), (13) gas sampling bag, (14) gas chromatograph.

4.4 Results and discussion

4.4.1 Catalyst preparation and characterization

The prepared calcined catalysts (Fe/NS and Co, Mo, Ru, and Cu promoted Fe/NS) were analyzed for surface area and the results summarized in Table 4.1. The S_{BET} surface area of Fe/NS catalysts was 127 m^2/g. The Fe/NS catalyst promoted by 5wt % Ru, and 10wt % Co had a slight decrease in S_{BET} surface area, suggesting that the Fe oxides were incorporated inside the NS pores after the co-impregnation process. In contrast, the Fe/NS catalyst promoted with 7wt % Cu and 5% Mo promoter loading increased the S_{BET} values to 192 m^2/g and 135 m^2/g, respectively. This seems to indicate that Cu and Mo improved the dispersion of iron oxides and thus increased the S_{BET} of Fe/NS catalyst [170, 171]. Similar result was obtained by Tasfy et al.[165] who reported that the surface area of Fe/SiO_2 catalyst increased upon addition of small amounts of Cu in the catalyst. The average crystallite size of Fe particles in Fe/NS, Ru-Fe/NS, Co-Fe/NS, Mo-Fe/NS and Cu-Fe/NS catalysts measured by using equation (Eq. 4-1) were found to be 9.0 nm,13.9 nm, 10.7 nm, 8.4 nm and 5.9 nm respectively. There is some difference between the average crystallite sizes of Fe particles calculated by d_{BET} and that obtained from d_{TEM} and d_{XRD}. In contrast, a positive correlation was observed between the average crystallite sizes of Fe particles obtained by d_{TEM} and d_{XRD}, as will be seen later (TEM and XRD results). This difference in crystallite sizes of Fe particles between d_{BET}, d_{TEM} and d_{XRD} may due to the aggregation of Ru nanoparticles on Fe oxides or NS surface.

Table 4.1. Surface area (S_{BET}) of Fe/NS and promoted catalysts

catalysts	Loading (wt %)	S_{BET} (m^2/g)
Fe/NS	15 %Fe	127
Ru-Fe/NS	5 % Ru-15 %Fe	82
Mo-Fe/NS	5 % Mo-15 %Fe	135
Cu-Fe/NS	7 % Cu-15 %Fe	192
Co-Fe/NS	10 % Co-15 %Fe	107

FTIR spectroscopy was performed to determine surface functional groups present of each prepared catalyst, as well as to examine the removal of organic species (organic solvents that used in the preparation catalysts) by calcination at 600 ^oC. The FTIR spectra are shown in Figure 4.2. It was found that all catalysts had characteristic Si–O–Si stretching and Si–O bands at around 1090 cm^{-1} and 813 cm^{-1}, respectively, and were in good agreement with the literature [102-104]. In addition, the absorption bands at around 2975 cm^{-1} and between 1410 -1460 cm^{-1} were related to C-H stretching and bending vibrations, respectively. The bands at around 3443 and 1637 cm^{-1} can be attributed to the H-O-H stretching and vibration of hydrogen bonded surface silanol groups and physically adsorbed water, respectively [104-106]. Furthermore, the absorption bands of Fe–O bond were observed in all catalysts at 588-590 cm^{-1} and consistent with the literature [104, 106, 140, 141]. Meanwhile, the FTIR spectra of promoted catalysts below 1000 cm^{-1} show some variances in the surface species (metal oxide (M-O) groups) present on NS as support. The weak and broad band at 843, 593, 666 and 555 cm^{-1} were respectively assigned to Mo-O [172], Cu-O [173],Co-O [174] and Ru-O. Thus, the FTIR results suggest that Fe and metal promoters (i.e., Co, Mo, Ru, and Cu) species were present in metal oxides structure on the NS.

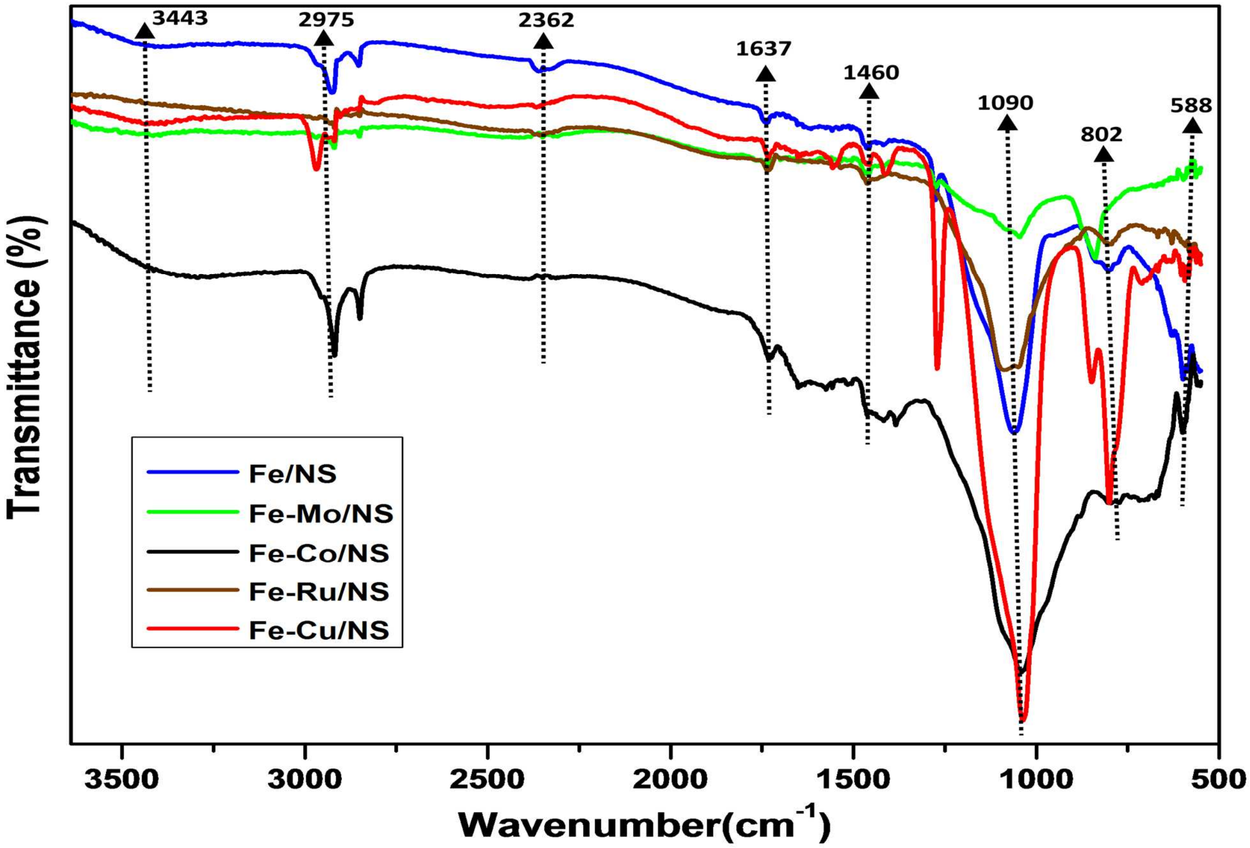

Figure 4.2. FTIR spectra of different promoters doped Fe/NS catalyst

To determine particle sizes and morphologies of NS supported Fe promoted catalysts, TEM was used. TEM micrographs of Fe/NS and promoted Fe/NS catalysts are shown in Figure 4.3. All of the NS supported catalysts were shown to have a nano-helical structure. For the Fe/NS catalyst (Figure 4.3e) the dark spots show the presence of Fe particles on the of NS surface with an average particle size (d_{TEM}) of 9.8 nm. For the promoted Fe/NS catalysts TEM does not differentiate between the metallic species on the surface of catalysts. However, it can be clearly seen from Figures 4.3a and 4.3d that several agglomeration of small metal particles were randomly dispersed on the surface of NS support of Co-Fe/NS and Ru-Fe/NS catalysts with average particle sizes (d_{TEM}) of 6.2 nm and 2.7 nm, respectively. Meanwhile, several agglomeration of large metal particles were found on the NS surface in Fe-Mo/NS and Fe-Cu/NS catalysts (Figure 4.3b and 4.3c) with average particle sizes (d_{TEM}) of 3.3 nm and 3.5 nm, respectively. In general, the particles showed small and large spherical morphology but with a tendency for agglomeration on the NS surface of all catalysts.

The elemental compositions of all the catalysts were determined by using energy dispersive X-ray spectrometry (EDS). Based on each individual EDS observations, all the expected metal elements were present on the surface of catalysts. Meanwhile, iron and silica signals were observed in all the EDS spectra, which confirmed that the Fe particles were successfully dispersed on the silica NS support. Moreover, the EDS analysis (Figure 4.4) of the Co-Fe/NS, Mo-Fe/NS, Cu-Fe/NS and Ru-Fe/NS promoted catalysts revealed the presence of each of their respective Co, Mo, Cu, and Ru species. This confirmed that the catalysts contained the promoter metal. It is worth noting that the EDS spectra of Co-Fe/NS, Mo-Fe/NS and Ru-Fe/NS catalysts also showed the presence of Cu (artificial Cu signals), which is attributed to the TEM copper grid sample holder. Also worth noting that the EDS spectra of the promoted Fe/NS catalysts exhibited the presence of some artificial signals as assigned to Cr and Al. This may be due to the fact that iron catalyst typically consist small fraction of chromium (III) oxide and aluminum oxide [51].

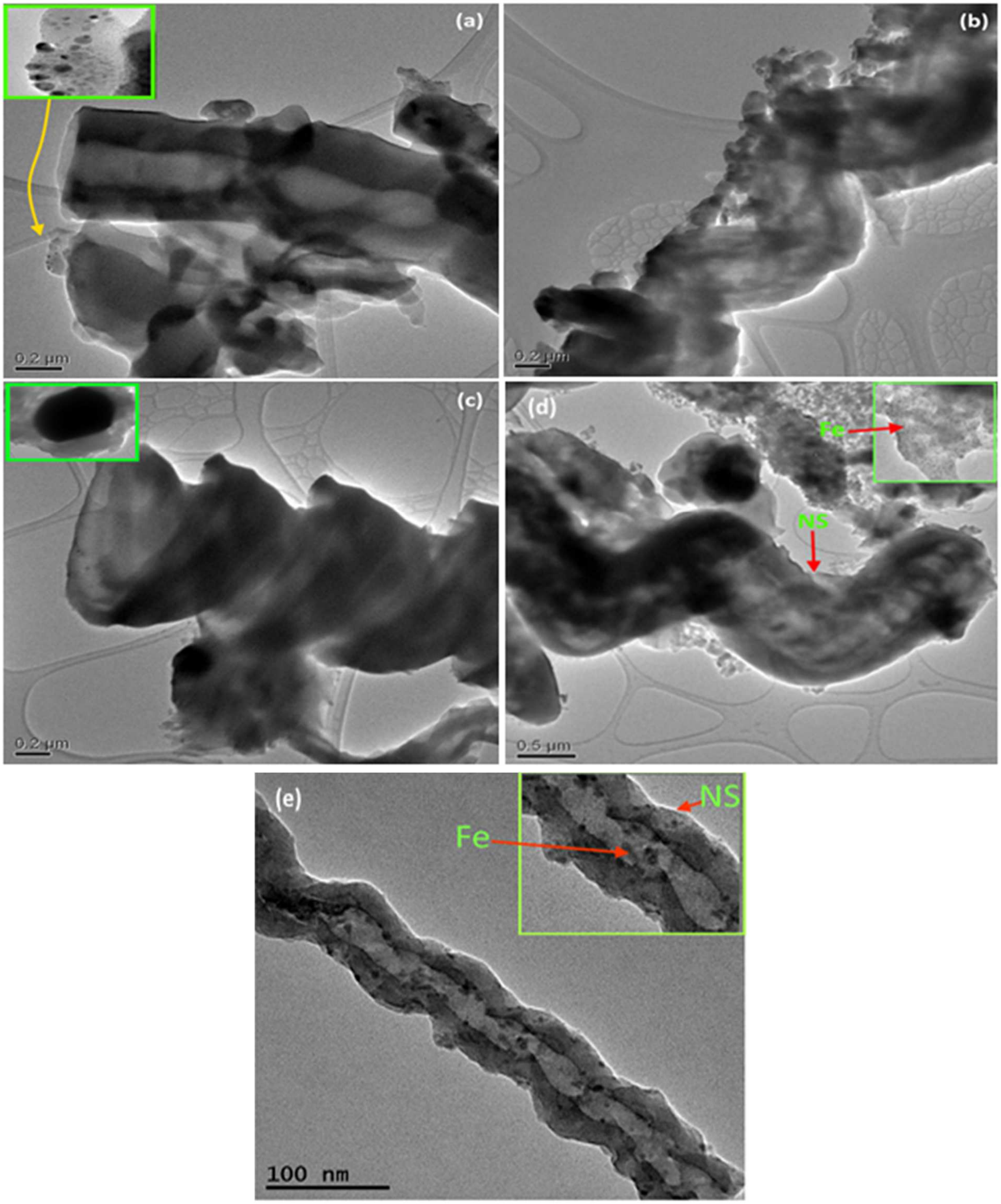

Figure 4.3. Transmission electron micrographs of calcined Co-Fe/NS (a), Mo-Fe/NS (b), Cu-Fe /NS (c), Ru-Fe/NS (d), and Fe/NS (e) catalysts

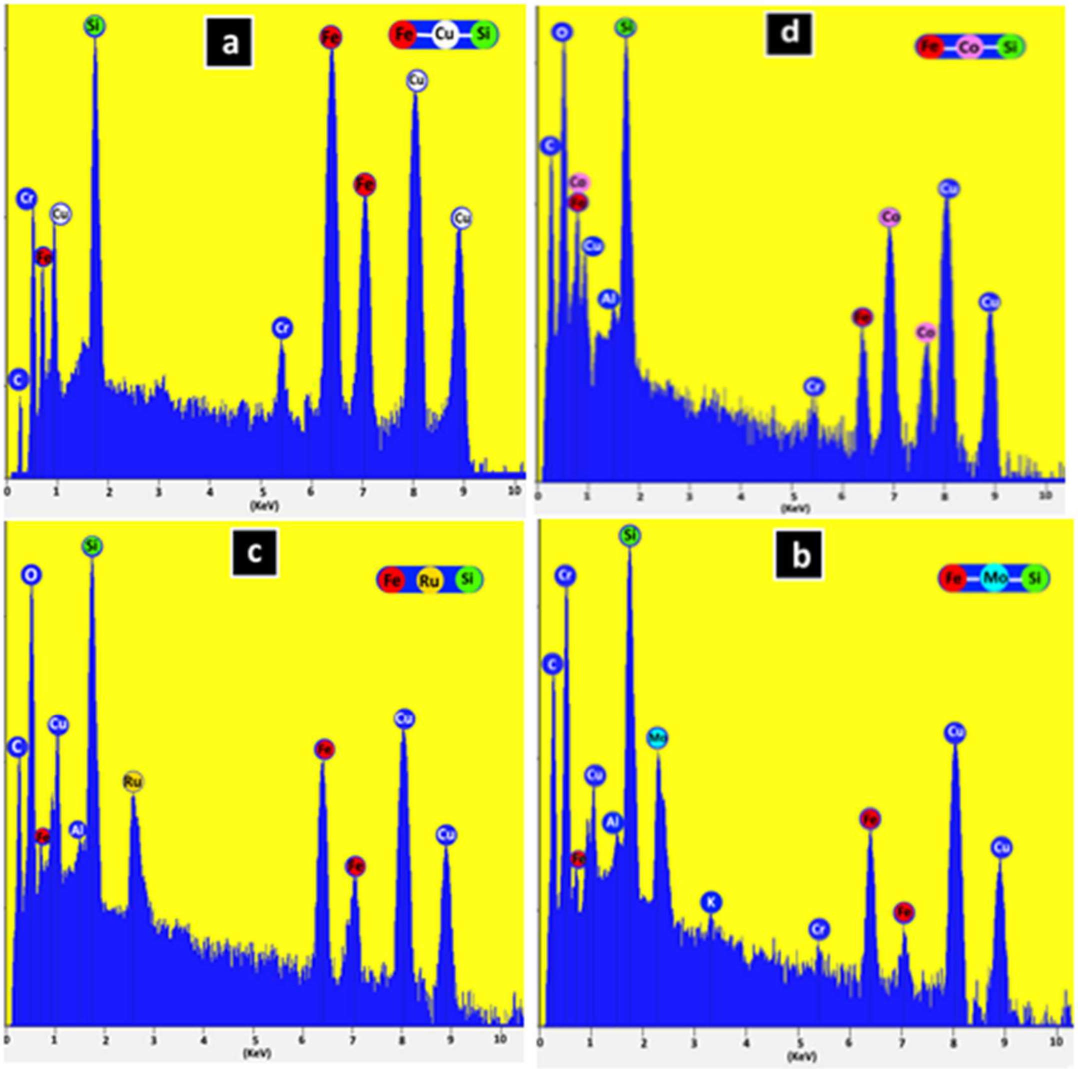

Figure 4.4. Energy dispersive spectra showing elemental composition of calcined promoted Cu-Fe/NS (a), Mo-Fe/NS (b), Ru-Fe/NS (c) and Co-Fe/NS (d) catalysts.

The thermal stability of the calcined Fe/NS based catalysts were evaluated by TGA and DTA. The TGA and DTA thermograms are shown in Figures 4.5a and 4.5b, respectively. The TGA thermogram of Fe/NS catalyst (Figure 4.5a) indicates that the total overall weight loss up to 900 °C was about 1.1 %, whereas the total overall weight losses for the Cu-Fe/NS, Ru-Fe/NS, Co-Fe/NS and Mo-Fe/NS promoted catalysts were 11.2%, 11.4%, 10.2% and 6.0%, respectively. This weight loss for the promoted Fe/NS catlyst is probably due to evaporation of adsorbed material on catalysts [106, 142]. Additionally, the weight loss was observed above 600 °C can be attributed to incomplete calcination, which corresponds to an exothermic peak between 600-800 °C by DTA (Figure 4.5b). However, the initial endothermic peaks in all catalysts around 55-100 °C may due to the removal of adsorbed water. Both the TGA and DTA analyzes of the Fe/NS catalysts showed no significant decomposition up to 900 °C, which clearly imply that all studied catalysts have a good thermal stability.

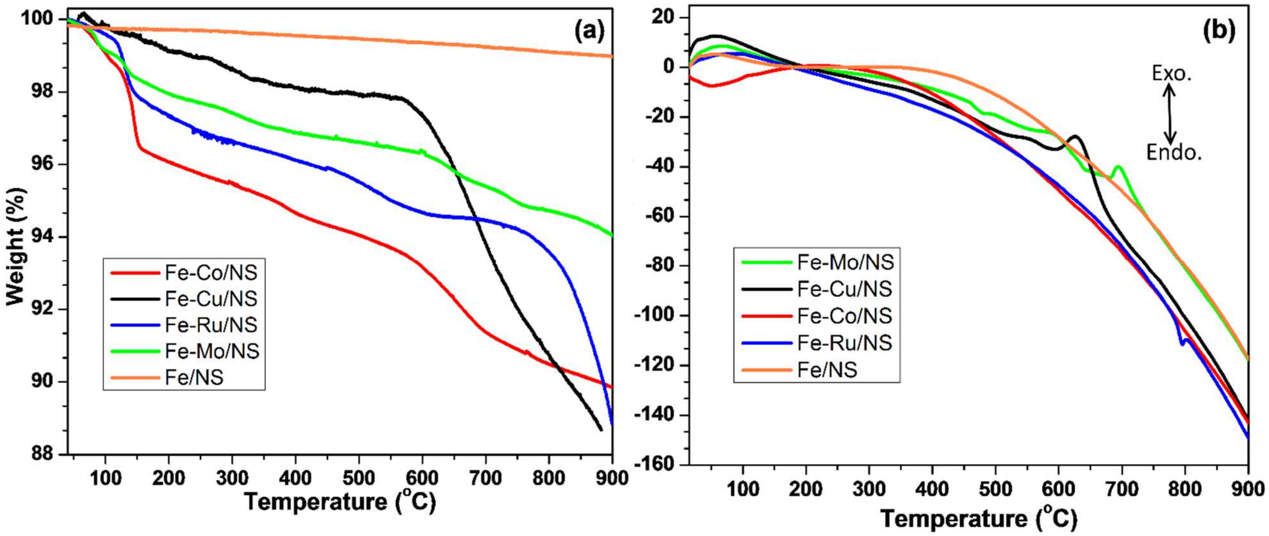

Figure 4.5. (a) TGA and (b) DTA thermograms of Fe/NS, Mo-Fe/NS, Co-Fe/NS, Cu-Fe/NS and Ru-Fe/NS catalysts.

X-ray diffraction (XRD) analysis was performed to identify the crystallographic phase in the catalysts. The XRD diffractograms of the calcined Fe/NS catalysts are shown in

Figure 4.6. XRD analysis showed that each of the catalysts are slightly different. All of the catalysts show a broad peak at 2θ about 23° which is assigned to crystal planes of the silica NS [98, 99]. The Fe/NS catalyst showed six major diffraction peaks centered at 2θ = 35.7°, 38.2°, 44.2°, 54.2°, 64.8° and 77.4°, which correspond to the (221), (311), (400), (422), (440), and (533) diffraction planes, respectively, of maghemite (γ-Fe_2O_3; JCPDS card 39-1346) [97, 117] [123-125]. The average crystallite size (d_{XRD}) of γ-Fe_2O_3 for Fe/NS catalyst was calculated to be 7.1 nm from the (311) diffraction peak at 2θ = 38.3° using the Scherrer's formula. Furthermore, the presence of γ-Fe_2O_3 was confirmed in all calcined Fe/NS promoted catalysts with different intensities of the diffraction peaks. However, the XRD diffractograms of the calcined promoted Fe/NS catalysts have diffraction peaks, which could be assigned to their respective metal (i.e. Co, Mo, Cu and Ru). The Ru-Fe/NS catalyst (Figure 4.6c) showed diffraction peaks at 2θ = 31.7°, 38.4°, 44.3°, 46.1°, 56.7° and 75.6° which are attributed to the characteristic diffraction peaks of RuO_2 species [175-177]. However, the XRD patterns of promoted Mo-Fe/NS catalyst (Figure 4.6b) shows several diffraction peaks at 2θ = 24.7°, 27.2°, 28.1°, 30.1°, 32.7°, 38.4°, 41.6° and 43.4° which could be attributed to crystalline of $Fe_2(MoO_4)_3$ (JCPDS No.31-0642), whereas diffraction peaks at 2θ = 49.1°, 53.3°, 57.4°, 60.1°, 67.6°, 74.5.4° and 78.7° were attributed to the characteristic diffraction peaks of MoO_3 (JCPDS No.35-0609) [178-182]. Previous studies reported that the mixture of Fe_2O_3 and molybdenum trioxide (MoO_3) can easily form a ferric molybdate $Fe_2(MoO_4)_3$ due to loss of water when the calcination temperature is over 470 °C [178, 179, 183]. The XRD diffractograms of Fe-Mo/NS catalyst showed a mixture of crystalline Fe_2

$(MoO_4)_3$ and MoO_3 phases on the surface of catalyst. The XRD diffractogram of Co-Fe/NS catalyst (Figure 4.6d) revealed the presence of the Co_3O_4 phase on the catalyst with diffraction peaks located at $2\theta = 36.9^o, 38.8^o, 44.9^o$and 65.3^o [162, 184]. In the case of the Cu-Fe/NS catalyst (Figure 4.6e), there were minor diffraction peaks at $2\theta = 34.0^o, 38.6^o$ and 49.0^o which can be ascribed to characteristic diffraction peak of crystal CuO species [185].

It is worth noting that the intensity of the peaks (particularly at 2θ about 38.2° and 44.2°) of Ru-Fe/NS, Cu-Fe/NS and Mo-Fe/NS catalysts declined compared to the diffraction peaks intensities of the unpromoted Fe/NS catalyst (Figure 4.6a). This suggests that the addition of Ru, Cu and Mo promoters decreased the crystallite size of γ-Fe_2O_3 and their dispersions increased [178, 185]. The average crystallite size of γ-Fe_2O_3 in Ru-Fe/NS, Cu-Fe/NS and Mo-Fe/NS catalysts were approximately 4.7, 5.4 and 6.0 nm, respectively. On the contrary, the average crystallite size of γ-Fe_2O_3 in Co-Fe/NS catalyst increased slightly with the addition of Co-promoter form 7.1 nm to 10.4 nm.

Overall, it can be concluded that the XRD results of calcined promoted Ru-Fe/NS, Co-Fe/NS, Cu-Fe/NS and Mo-Fe/NS catalysts consist of RuO_2, Co_3O_4, CuO and $Fe_2(MoO_4)_3$/ MoO_3 phases, respectively and all the diffraction peaks in promoted Fe/NS catalysts reveal the good crystallinity. The EDS results are also in agreement with the XRD results and displayed the presence of the Fe, Ru, Co, Cu and Mo elements, which indicates that promoted Fe/NS catalysts comprised of oxide promoter phases.

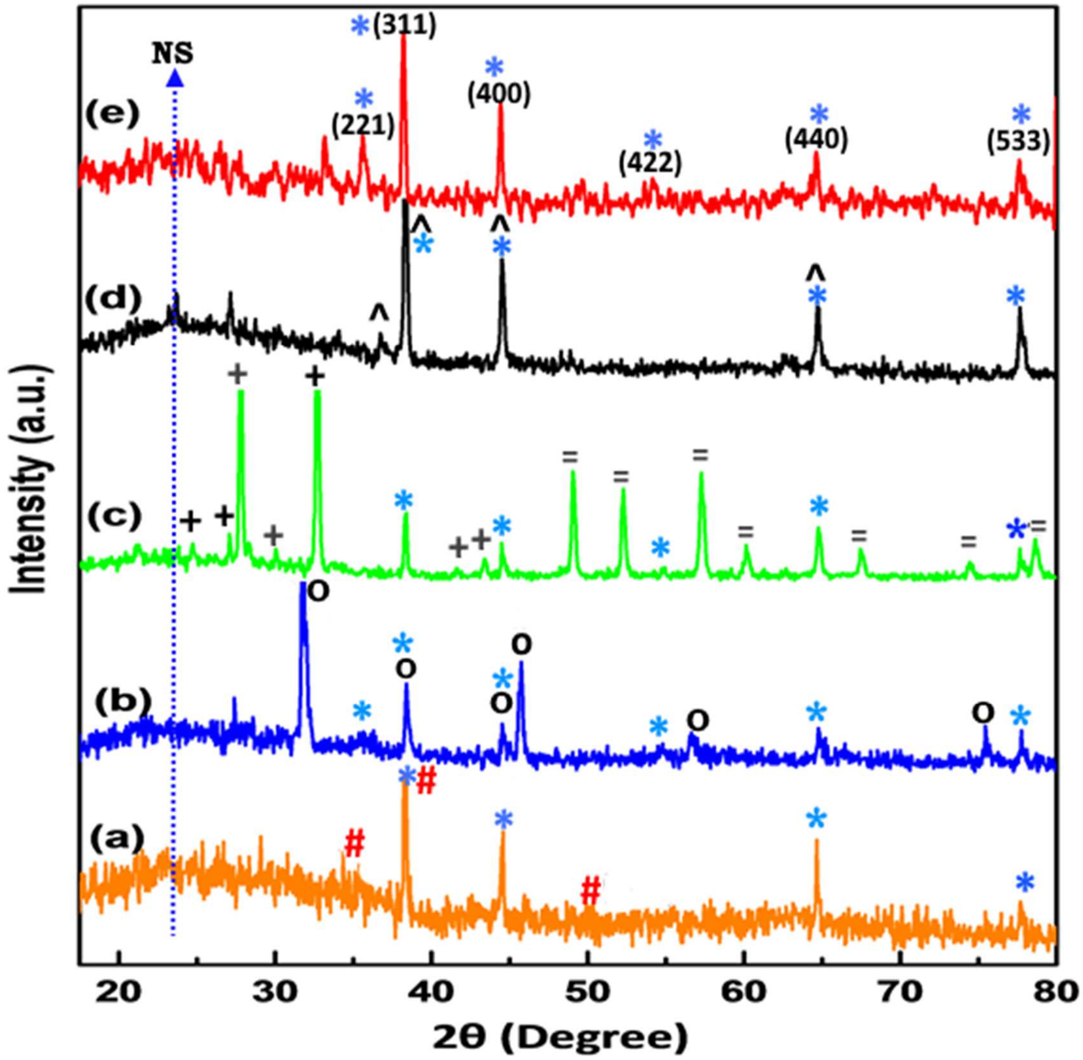

Figure 4.6. X-ray diffractograms of calcined of promoted and unpromoted Fe/NS catalysts: (a) Cu-Fe/NS, (b) Ru-Fe/NS, (c) Mo Fe-/NS, (d) Co Fe-/NS and (e) unpromoted Fe/NS catalyst. (NS), silica nanosprings; (*), Fe_2O_3; (^),Co3O4; (o), Ru; (#), CuO.

In order to further confirm the chemical states and composition of Fe, Ru, Co, Cu and Mo species on the surface and near surface of promoted Fe/NS catalysts, XPS was used to characterize all promoted Fe/NS catalysts.

The elements C, O, Fe, and Si were detected on all catalysts by XPS (Figure 4.7), except for the XPS of Ru-Fe/NS catalyst which did not show the Fe2p (710 eV) peak

(Figures 4.7c and 4.8). The absence of Fe2p peak suggests that iron oxide nanoparticles are confined within the porous NS support and not at the surface, which limited its detection in high resolution Fe2p spectrum [186][104][157]. The core level states at binding energies at approximately 285, 531, 710 and 103 eV were attributed to C1s, O1s, Fe2p and Si2p, respectively [132]. Moreover, the core level states at binding energies of near 710 and 723 eV in all catalysts were attributed to Fe2p$_{3/2}$ and Fe2p$_{1/2}$, respectively [124, 133, 134]. Figure 4.9(a-e) show high resolution scans of the Co2p for Co-Fe/NS, Cup2 for Cu-Fe/NS, Mo3d for Mo Fe-/NS, Ru3d for Ru Fe-/NS and Ru3p for Ru-Fe/NS catalyst. The initial high resolution XPS spectrum of the Co2p, Cu2p, Mo3d, Ru3d and Ru3p regions are shown in Figure 4.9. The presence of Ru, Co, Cu and Mo particles on the surface of promoted Fe/NS catalysts are identified by the binding energies of Co2p 3/2 and Co2p1/2 (780.9 eV and 796.2 eV[187], Cu2p$_{3/2}$ and Cup$_{1/2}$ (933.2 eV and 953.1 eV) [185] , Mo3d $_{3/2}$ and Mo3d$_{1/2}$ (232.9 eV and 236.1 eV) [182], Ru3d$_{3/2}$ and Ru3d$_{5/2}$ (282.9 eV and 279.2 eV)[188] [189] and Ru3p$_{3/2}$ (462.2 eV)[189]. These results in good agreement the with XRD analysis that give evidence for the existence of RuO_2, Co_3O_4, CuO and Fe2$(MoO_4)_3$/MoO_3 phases on Ru-Fe/NS, Co-Fe/NS, Cu-Fe/NS and Mo-Fe/NS catalysts, respectively.

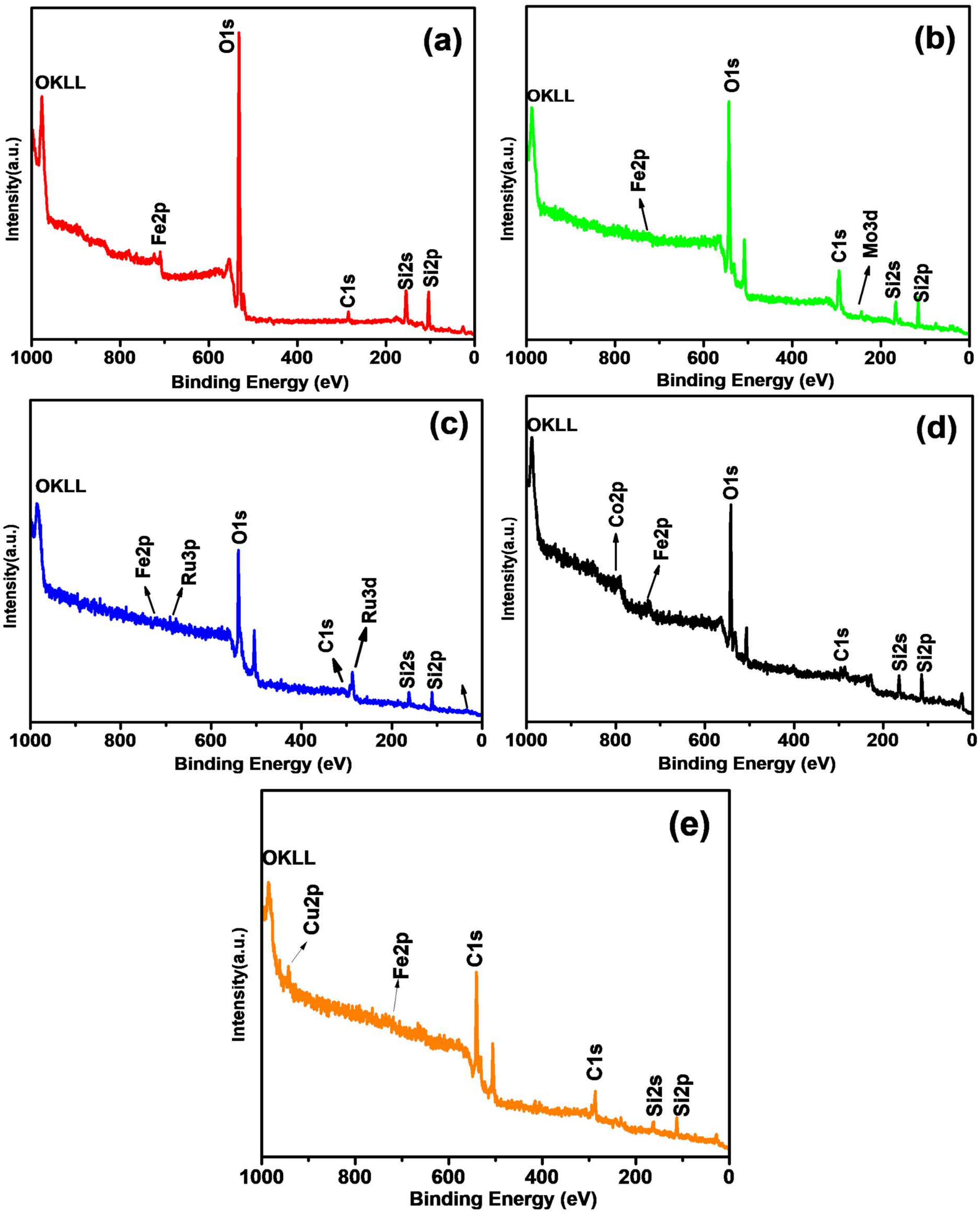

Figure 4.7. Wide scan X-ray photoelectron spectra (XPS) of (a) Fe/NS, (b) Mo-Fe/NS, (c) Ru-Fe/NS, (d) Co-Fe/NS and (e) Cu-Fe/NS catalysts.

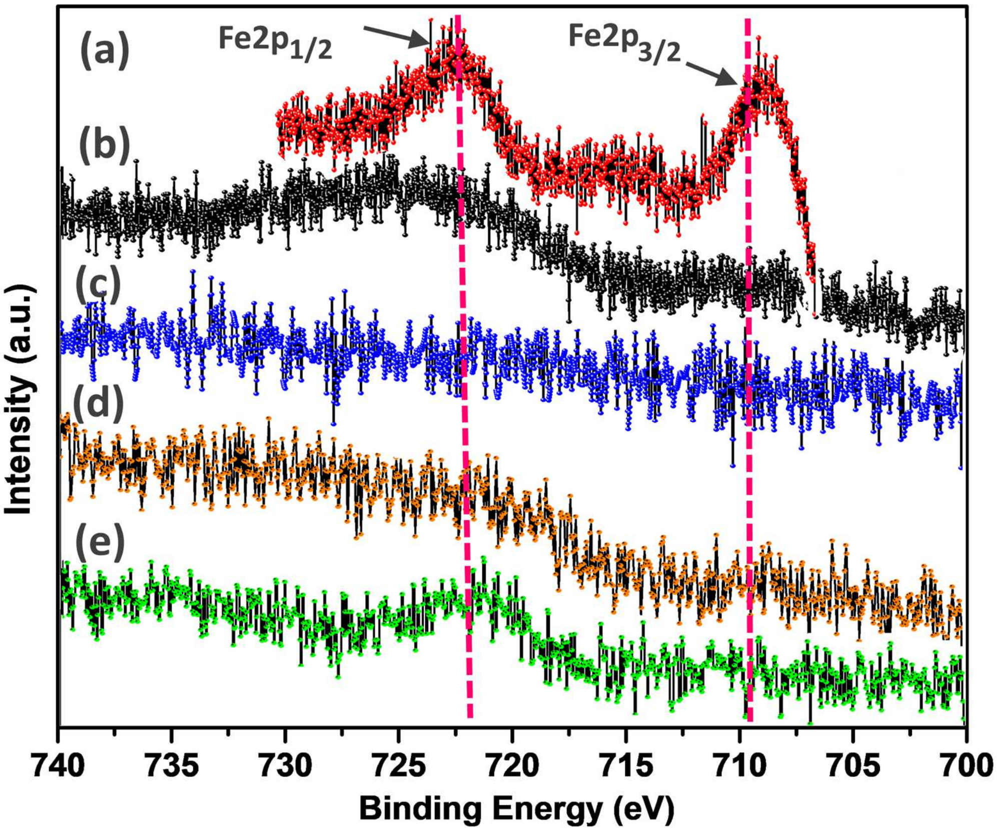

Figure 4.8. High resolution (XPS) spectra of the Fe 2p; (a) Fe/NS, (b) Co-Fe/NS, (c) Ru-Fe/NS, (d) Cu-Fe/NS and (e) Mo-Fe/NS catalysts.

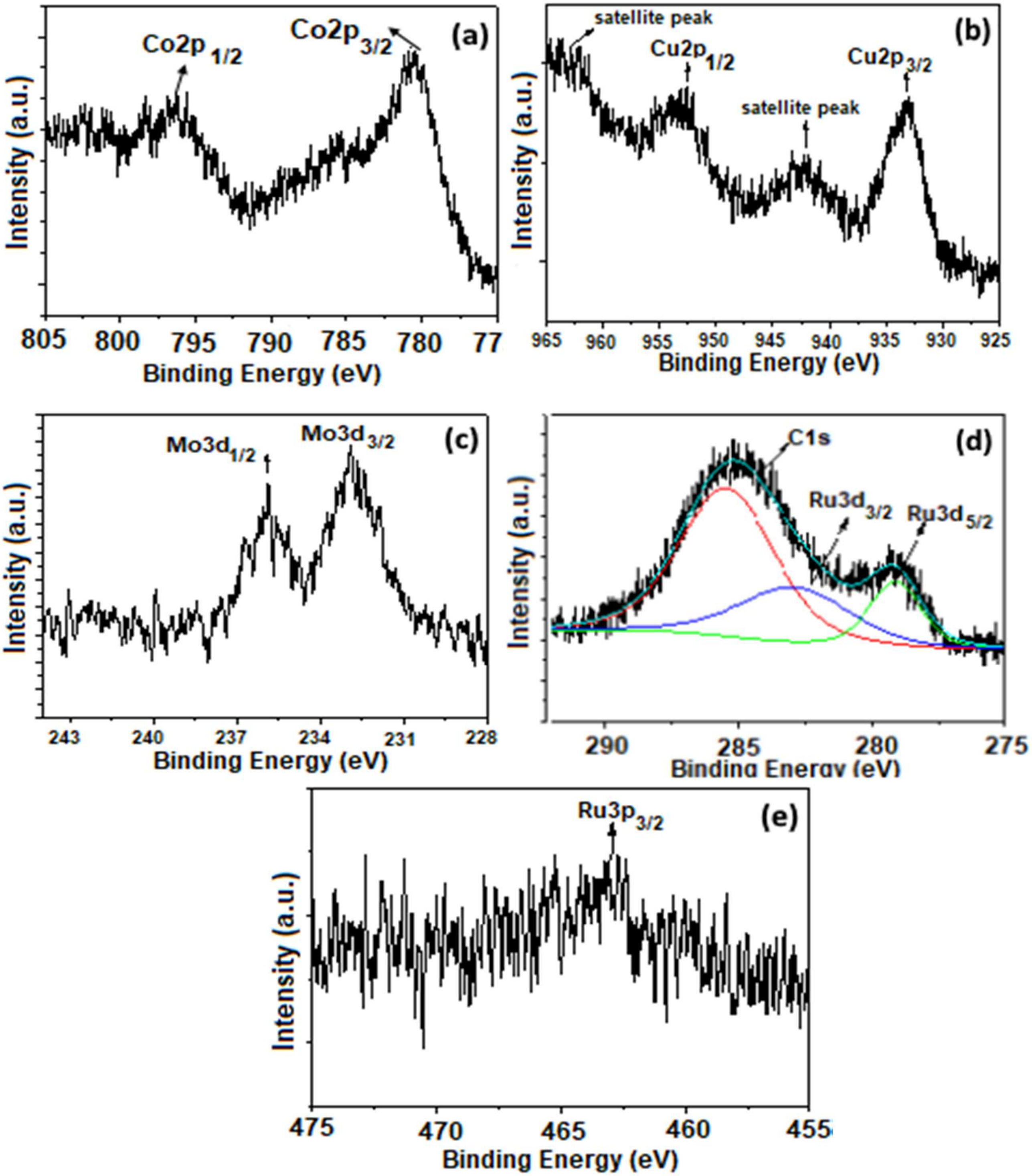

Figure 4.9. High resolution (XPS) spectra of promoted Fe/NS catalysts: (a) Co2p for Co-Fe/NS (b) Cup2 for Cu-Fe/NS, (c) Mo3d for Mo Fe-/NS, (d) Ru3d for Ru Fe-/NS and (e) Ru3p for Ru-Fe/NS catalyst.

H_2-TPR was performed to determine the temperature at which the metal oxide were reduced in the presence of H_2. Figure 4.10 shows the H_2-TPR profiles of the three calcined Co-Fe/NS, Mo-Fe/NS, Cu-Fe/NS, Ru-Fe/NS and Fe/NS catalysts. TPR patterns of the Fe/NS catalyst (Figure 4.10a) is characterized by three major peaks located at 406, 538 and 680 ^{o}C, which corresponds to the reduction of Fe_2O_3 to Fe_3O_4, Fe_3O_4 to FeO, and FeO to Fe(0), respectively. The TPR profile of the calcined Mo-Fe/NS catalyst consists of five peaks (Figure 4.10b). The first narrow peak located at 457 ^{o}C can be assigned to the reduction of Fe_2O_3 to Fe_3O_4, whereas the two peaks at around 509^{o}C and 601 ^{o}C correspond to the two reduction steps of the iron oxide: Fe_3O_4 to FeO and then FeO to Fe (0), respectively. Two further peaks appeared at 739 ^{o}C and 797 ^{o}C which corresponding to the reduction of MoO_3 to MoO_2 to Mo (0), respectively. For calcined Cu-Fe/NS catalyst (Figure 4.10c), it can be seen in the TPR profile that only four peaks were present: a sharp peak centered at 250 ^{o}C can be assigned to the reduction CoO to Cu (0) and peaks located at 427, 471 and 592 ^{o}C, corresponding to the reduction of Fe_2O_3 to Fe_3O_4 to FeO to Fe (0), respectively [185]. For calcined Ru-Fe/NS catalyst (Figure 4.10d), the peak at 197 ^{o}C can be attributed to reduction of RuO_2 to Ru (0), and its position depends on the degree of Ru dispersion [189-191]. Moreover, the relatively small peaks detected in the range 382-557^{o}C can be interpreted as corresponding to reduction of Fe_3O_4 to Fe (0). The reduction patterns of calcined Co-Fe/NS catalyst is shown in Figure 4.10e. It can be noted from the H_2-TPR profiles that the first two peaks located at 293^{o}C and 378 ^{o}C correspond to the two reduction steps of the Co_3O_4 species to CoO to Co (0), respectively [192, 193]. However, peaks located at 440°C, 500°C and 659 °C can be assigned to the reduction of Fe_2O_3 to Fe_3O_4 to FeO to Fe(0), respectively. It was clear that the Ru played a more important role in improving the reduction temperature of Fe oxides. In contrast to this, H_2-TPR of Mo-Fe/NS catalyst showed strong interaction between Fe and MO oxides, causing slight increase in reduction temperature after addition of Mo to Fe/NS catalyst. Generally, the addition of small amounts of Ru, Co, and Cu promoters to Fe/NS catalyst significantly decrease the reduction temperature of (Fe_2O_3) Fe/NS catalyst. This is indicated by a shift of the TPR peaks to lower temperatures compared to the peaks of TPR profiles of the Fe/NS catalyst (Figure 4.10a).

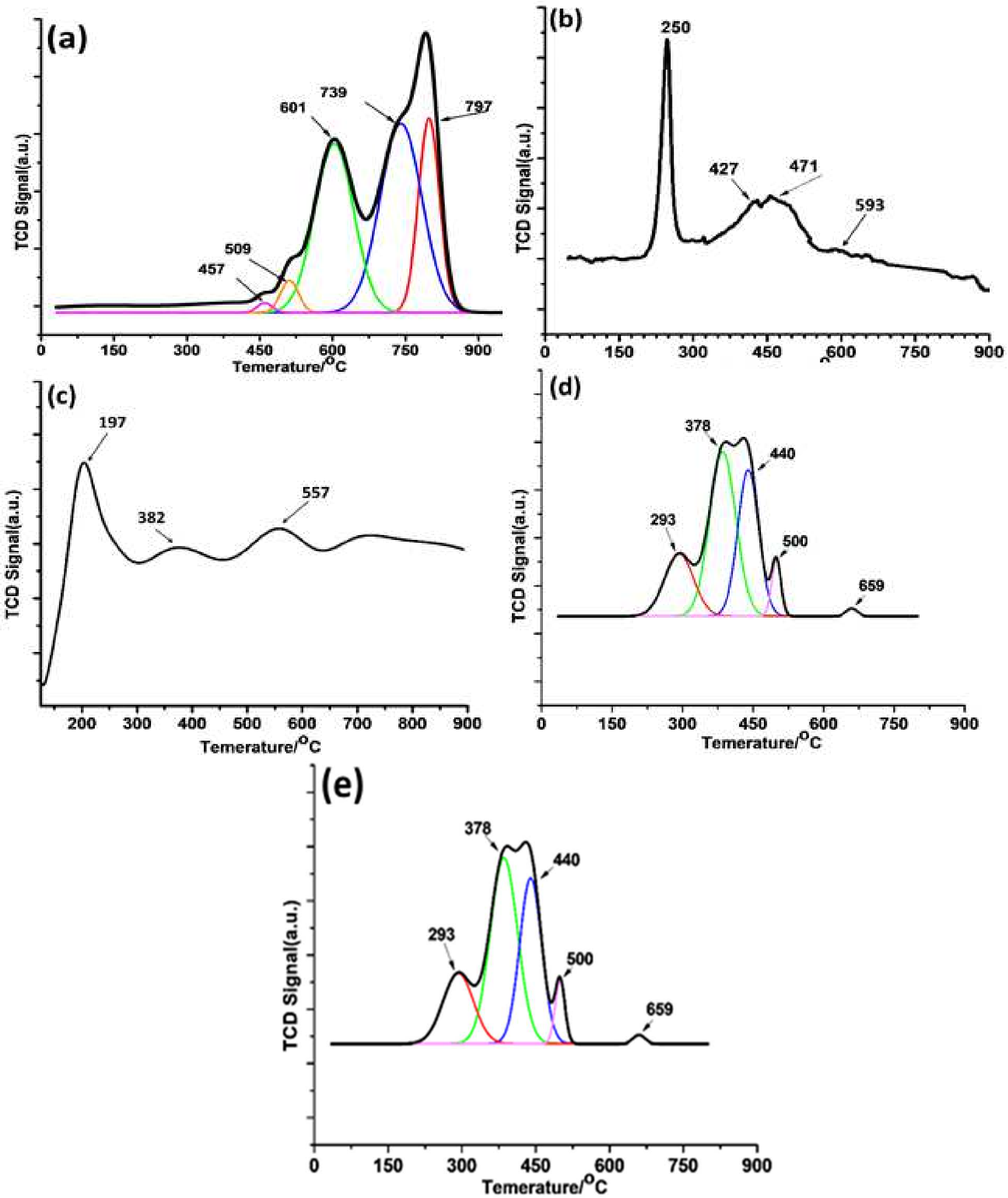

Figure 4.10. H_2-TPR profiles of Fe/NS catalysts: (a) Fe/NS, (b) Mo-Fe/NS, (c) Cu-Fe/NS,(d) Ru-Fe/NS and (e) Co-Fe/NS catalysts.

4.4.2 Catalyst Evaluation

The Fe/NS based catalysts were reduced using H_2 in N_2 gas mixture. The catalytic performances of Fe/NS catalysts were carried out in a quartz fixed-bed micro-reactor at 230 ^{o}C with a H_2/CO ratio of 2 for 84 h. The condensable liquid products were analyzed by GC-MS(Figure 4.13- 4.17) and the non-condensable gases (CO, CO_2, H_2, N_2, CH_4 and C_2-C_4) were analyzed by GC. Table 4.2 shows the effect of Ru, Co, Mo and Cu promoters on the catalytic performance of the Fe/NS catalyst. In the case of Fe/NS catalyst, the FT hydrocarbon product distribution was in the carbon number range of C_6-C_{16} with CO conversion of 68.2%. This catalytic performance could be attributed to the following possibilities: (i) the dispersion of iron particles in the Fe/NS catalyst is more homogeneous on the surface of NS support, which should be favorable for the CO conversion, (ii) the possibility of the formation of the most active iron carbide phases for FTS (χ-Fe_5C_2) or (θ-Fe_3C) after activation by carburization and/or during FTS reaction. Although this study does not provide any evidence that can explain the existence of these carbides after activation and FTS reaction and this is in line with the literature [116, 148, 149]. Most of the hydrocarbons product were aromatics in range of C_6-C_{16} (Table 4.2, Figure 4.11). The formation of C_6-C_{16} aromatic hydrocarbons by unpromoted Fe/NS catalyst are mainly composed of mono-nuclear aromatics that include xylenes (m, o and p), toluene and alkyl benzenes (ethyl benzene, trimethyl, tetramethyl, and 1-ethyl-4-methylbenzenes, etc). In addition, there are several classes of hydrocarbons formed by unpromoted Fe/NS catalyst, among which di- and poly-nuclear aromatics such as naphthalene and alkyl-naphthalene isomers. The aromatic products contribute 43.5 % overall, from C_6-C_{16} components. These results are in accordance with the results reported in our previous results [157].

The effect of Ru, Co, Mo and Cu promoters on H_2, CO conversions and product (C_6-C_{16}) distribution results are presented in Figures 4.11 and summarized in Table 4.2. As shown in Figure 4.11 and Table 4.2 the liquid product distribution (C_6-C_{16}) and CO conversion were affected by adding Ru, Co, Mo and Cu promoters to the Fe/NS catalysts. However, Figure 4.11 shows the hydrocarbons selectivity of promoted Fe/NS catalysts decreased, and CO_2 selectivity decreased with the addition of promoters. Table 4.2 also shows that the CO conversions of Ru-Fe/NS and Mo-Fe/NS catalysts increased (from 68.2% to 93.3% and 82.4%, respectively) by adding Ru and Mo promoters. Whereas, the addition of Co and Cu promoters decreases the CO conversions of Co-Fe/NS and Cu-Fe/NS catalysts (from 68.2% to 43.6% and 56.3 %, respectively). Furthermore, it is found that the product selectivity towards C_6–C_{14} in Ru-Fe/NS, Co-Fe/NS, Mo-Fe/NS and Cu-Fe/NS catalysts decreased after addition of promoters (from 5.1% to 89.3%, 53.0%, 65.3% and 69.8%, respectively) as compared to Fe/NS catalyst. It can be also seen in Table 4.2 that the ratio of olefin to paraffin (O/P) increased with the addition of promoters. This could be due chemical or electronic effect of promoter metal oxide on the Fe [194]. The Co-Fe/NS and Cu-Fe/NS catalysts exhibit higher (O/P) C_6-C_{16} (1.68 and 1.03, respectively) than others. This is possibly due to the improved dispersion of Fe oxides in both catalysts. On the other hand, the addition of Ru, Mo, Co and Cu promoters changed in the liquid product distribution C_6-C_{16} (JP-4 jet fuel and gasoline ranges) (Figure 4.12). The unpromoted Fe/NS catalyst exhibits more favorable to aromatics (52.1%) than paraffin (1.7%) and olefins (2.6%). Comparing the selectivity and distribution of all promoted Fe/NS catalysts that the Ru-Fe/NS shows low selectivity to methane and the highest distribution of products to C_6-C_{16} of 89.3%. The major hydrocarbon products in the C_6–C_{16} range for all promoted catalysts are paraffins, olefins, naphthenes (cycloalkanes) and a small amount of oxygenated products. The results indicate that the addition of Ru, Mo, Co and Cu promoters improved the FT hydrocarbon product distribution towards the production of gasoline. The Olefin distribution (%) in carbon number fractions for liquid products of all catalysts are is shown in Figure 4.18. The addition of Ru, Mo, Co and Cu promoters to Fe/NS catalyst lead to significant changes in selectivity to olefins. Thus, highest selectivity towards olefins were obtained over both Ru-Fe/NS and Cu-Fe/NS catalysts in the C_9, then decreasing with the C number, while that over Ru-Mo/NS and Co-Fe/NS catalysts was in C_{13}. The FTS hydrocarbons products (C_6-C_{16}) obtained from unpromoted Fe/NS catalyst was found to be qualitatively different from that found in promoted Fe/NS catalysts, while the hydrocarbons products (C_6-C_{16}) obtained from promoted Fe/NS catalysts were found to be qualitatively similar but not quantitatively. Figures 4.13 through 4.17, show the chromatograms of liquid FTS product obtained by GC-MS analysis for promoted/unpromoted Fe/NS catalysts. The chromatograms of unpromoted Fe/NS catalyst (Figure 4.13) shows different peaks and retention times of the hydrocarbons products compared with those obtained from promoted Fe/NS catalyst. The GC/MS analysis of liquid products provided the product distribution of hydrocarbons between C_6 and C_{16}, with high selectivity towards the formation of aromatics that include benzene, ethylbenzene, toluene and xylenes (m, o and p), etc. Besides, minor paraffins, olefins, naphthenes and oxygenates (C_6-C_{16}) compounds were identified by GC-MS in Fe/NS catalyst. In contrast, the major hydrocarbon products in the C_6–C_{16} range for all promoted Fe/NS catalysts were mainly composed of olefins that include n-olefins (alkenes) such as undecene and branched olefins (isomers) such as 4-Methyl-1-undecene. In addition, there are several classes of hydrocarbons formed by promoted Fe/NS catalysts, among which paraffins, naphthenes and minor oxygenates. The compounds identities (C_6-C16 range) identified using the GC/MS obtained from all unpromoted and promoted Fe/NS catalyst are given in Tables 4.3 through 4.7. Moreover, Figure 4.19 shows the CO conversion over Fe/NS, Ru-Fe/NS, Co-Fe/NS, Mo-Fe/NS and Cu-Fe/NS catalysts as a function of time on stream at 230 ^{o}C. CO conversion in promoted and unpromoted Fe/NS catalysts are relatively constant and reach their highest activities after almost 12 hours into the reaction, and then decreased slightly with time. It can be concluded that no significant deactivation in catalytic stability has been observed during the 84 h run of the FT reaction. The initial change in Co conversions of all catalysts during 6 h may be caused by carburization reaction of Fe catalysts during FTS reaction.

Table 4.2. Catalytic performance and major components of synthesized liquid F-T fuel over unpromoted/promoted Fe/NS catalysts at 230 °C, $H_2/CO=2$ and at atmospheric pressure.

Catalyst	Fe/NS	Ru-Fe/NS	Co-Fe/NS	Mo-Fe/NS	Cu-Fe/NS
CO Conversion (%)	68.2	93.3	43.6	82.4	56.3
H_2 Conversion (%)	54.6	79.2	39.8	67.4	47.2
Products Selectivity (%)					
CO_2 select. (%)	23.7	0.8	1.6	9.4	12.3
CH_4 select. (%)	13.9	6.3	20.7	13.6	8.1
$\sum < C_5$	10.3	3.6	24.7	11.7	9.8
Product distribution (Mol.%)					
$\sum C_6$-C_{16}	52.1	89.3	53.0	65.3	69.8
C_6-C_{16} Paraffins	1.7	29.8	8.6	12.6	25.4
C_6-C_{16} Olefins	2.6	41.1	30.1	25.4	33.8
Naphthenes	2.5	14.6	9.3	19.5	7.2
Aromatics	43.5	0	0	0	0
Oxygenates	1.8	3.8	5.0	7.8	3.4
Olefins/ Paraffins (o/p)	0.61	0.92	1.68	0.79	1.03

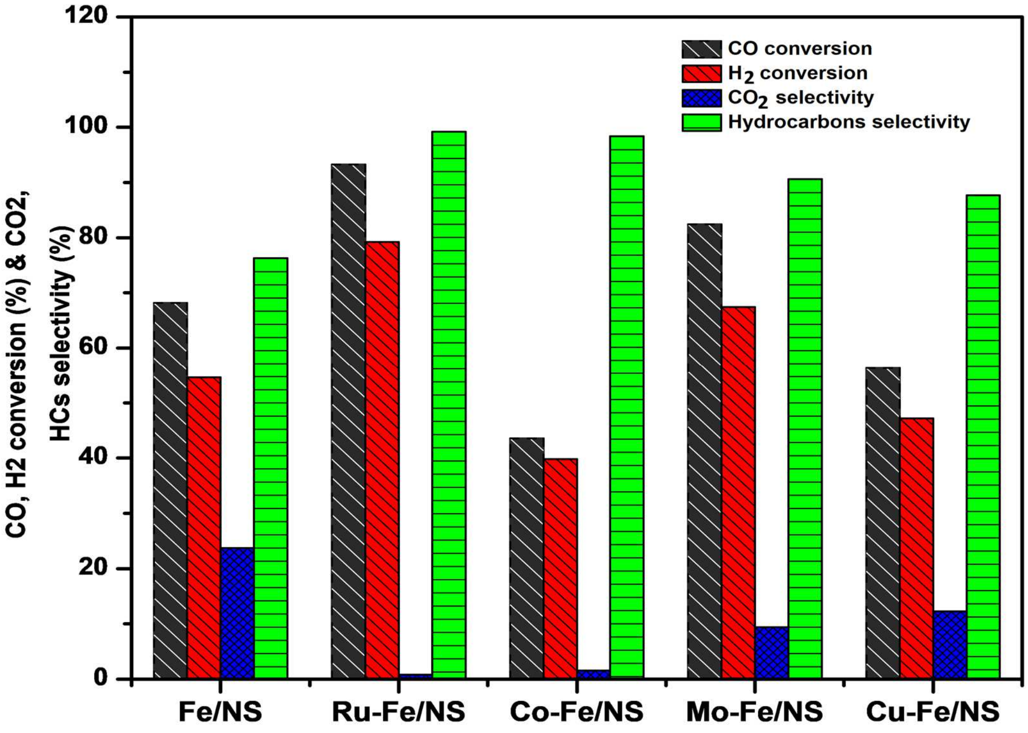

Figure 4.11. CO and H_2 conversions, CO_2 and hydrocarbons selectivities of promoted and unpromoted Fe/NS catalysts.

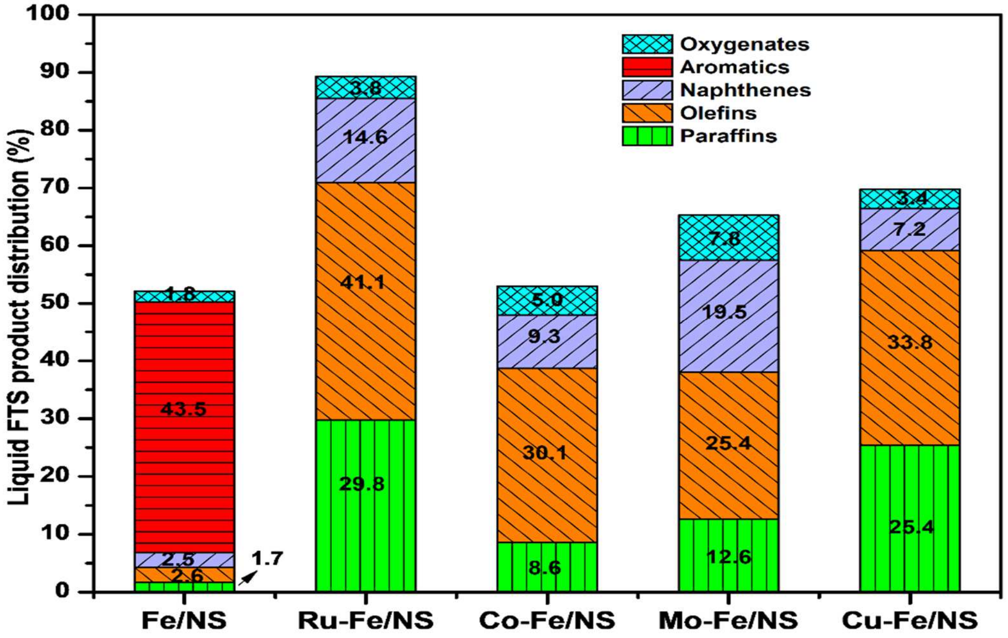

Figure 4.12. The liquid product distribution (C_6-C_{16}) obtained in the catalytic conversion of promoted and unpromoted Fe/NS catalysts.

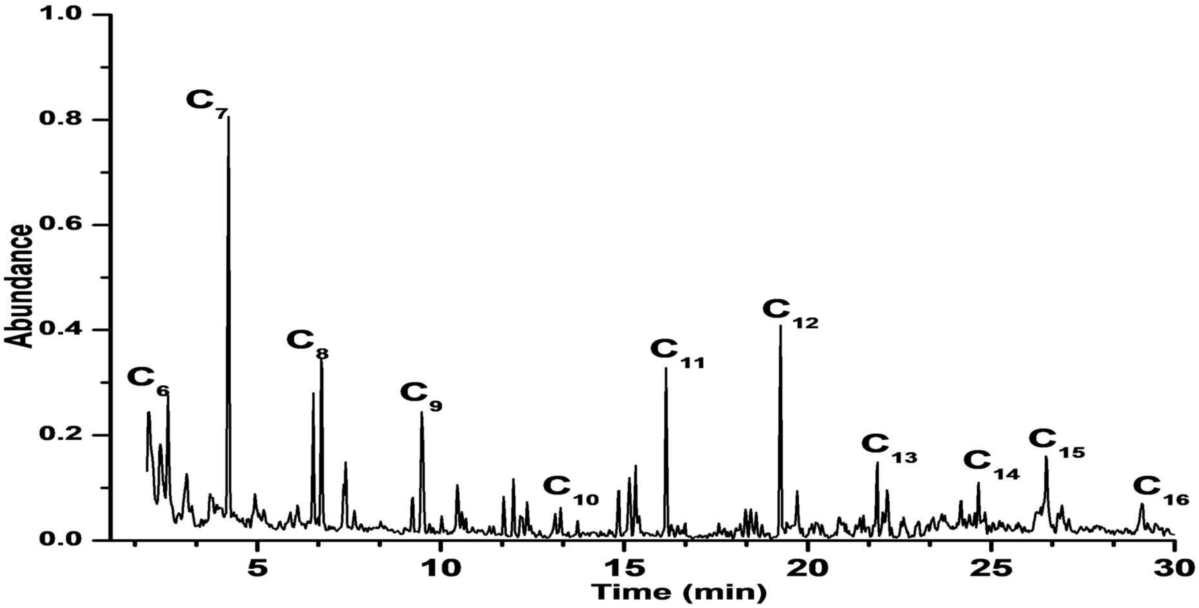

Figure 4.13. Overall FTS product spectrum obtained using GC-MS analysis, for unpromoted Fe/NS catalyst, at 230 °C and atmospheric pressure with a H_2/CO ratio of 2 for 12 h.

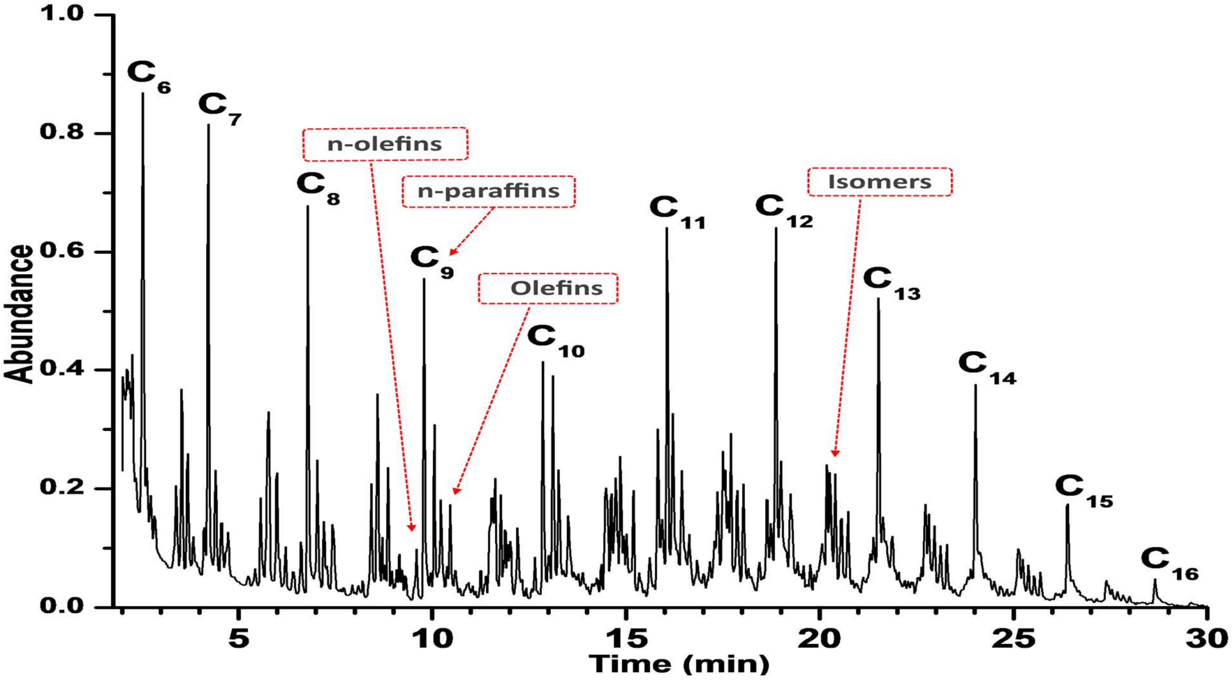

Figure 4.14. Sample GC-MS showing overall FTS product spectrum obtained from Ru-Fe/NS catalyst, at 230°C and atmospheric pressure with a H_2/CO ratio of 2 for 12 h.

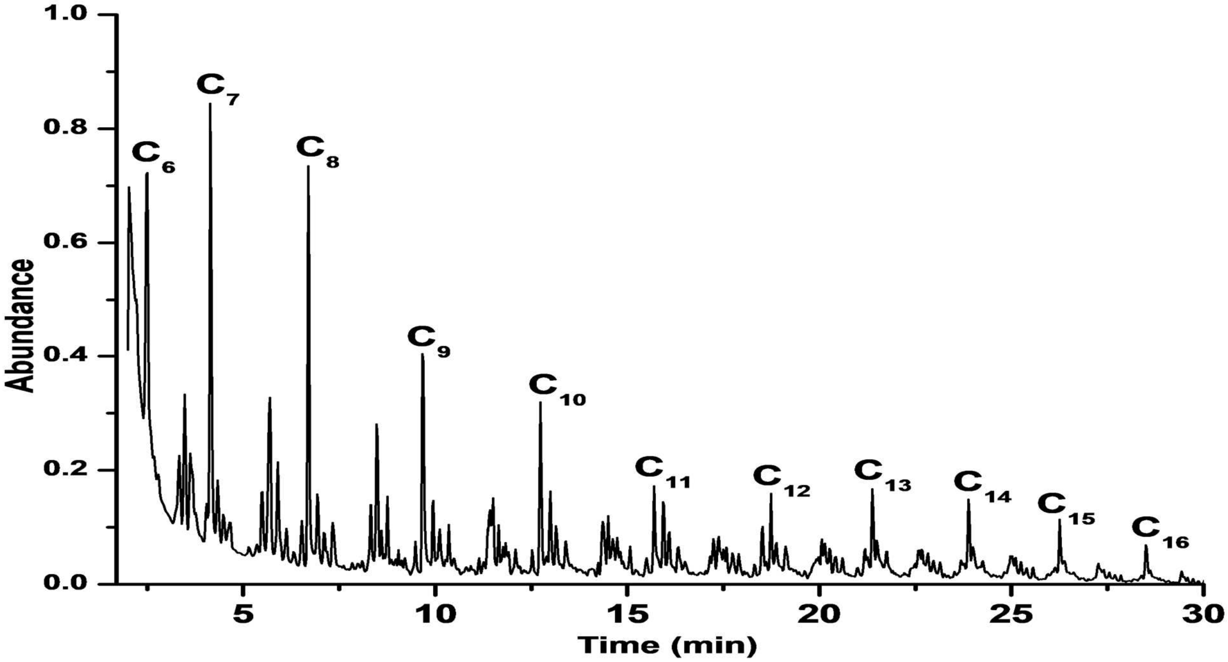

Figure 4.15. Overall FTS product spectrum obtained using GC-MS analysis, for Mo-Fe/NS catalyst, at 230°C and atmospheric pressure with a H_2/CO ratio of 2 for 12 h.

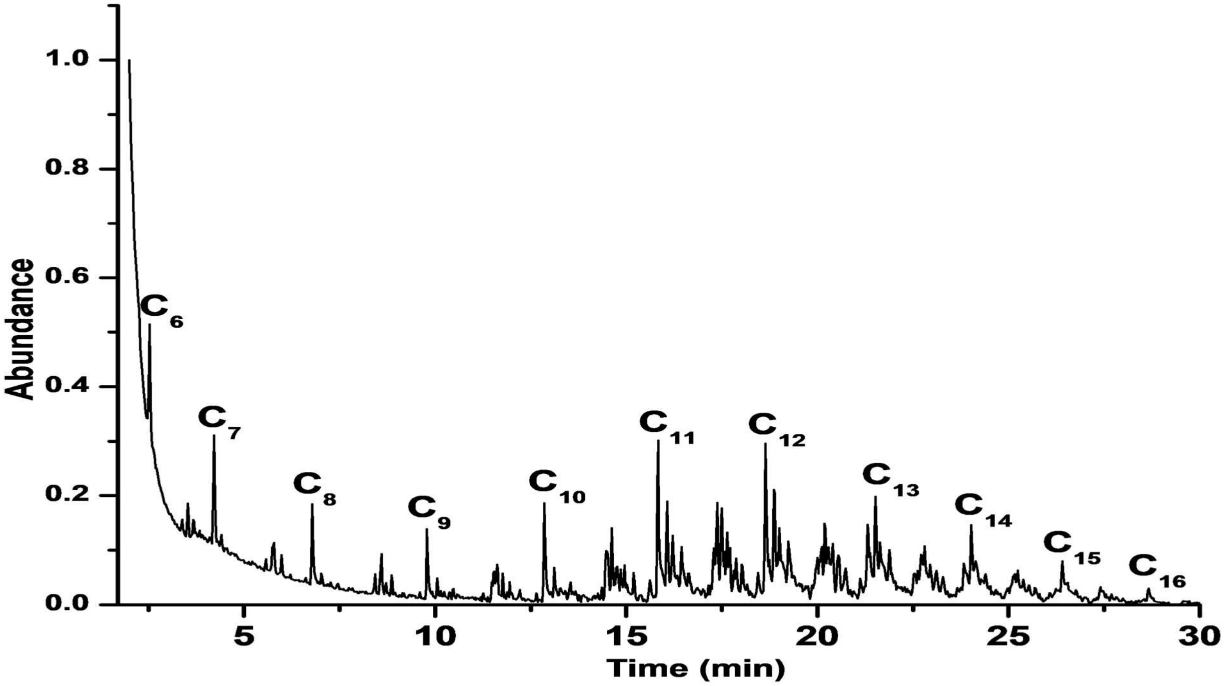

Figure 4.16. Overall FTS product spectrum obtained using GC-MS analysis, for Co-Fe/NS catalyst, at 230°C and atmospheric pressure with a H_2/CO ratio of 2 for 12 h.

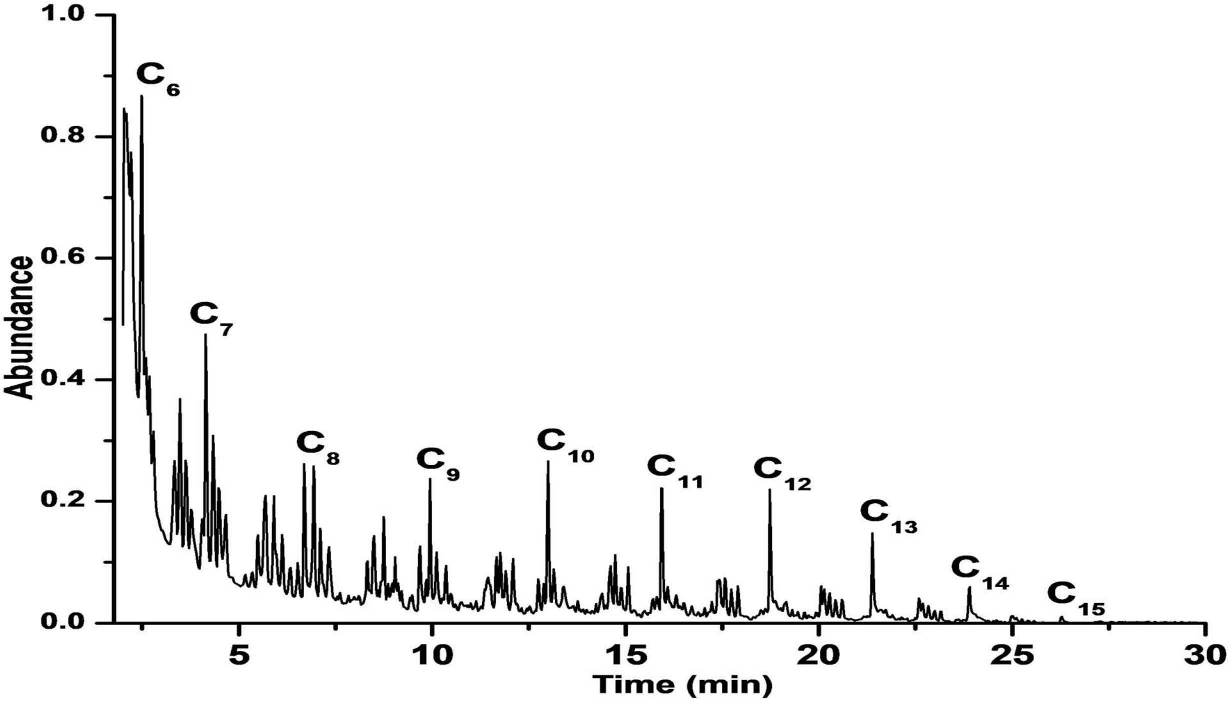

Figure 4.17. Overall FTS product spectrum obtained using GC-MS analysis, for Cu-Fe/NS catalyst, at 230°C and atmospheric pressure with a H_2/CO ratio of 2 for 12 h.

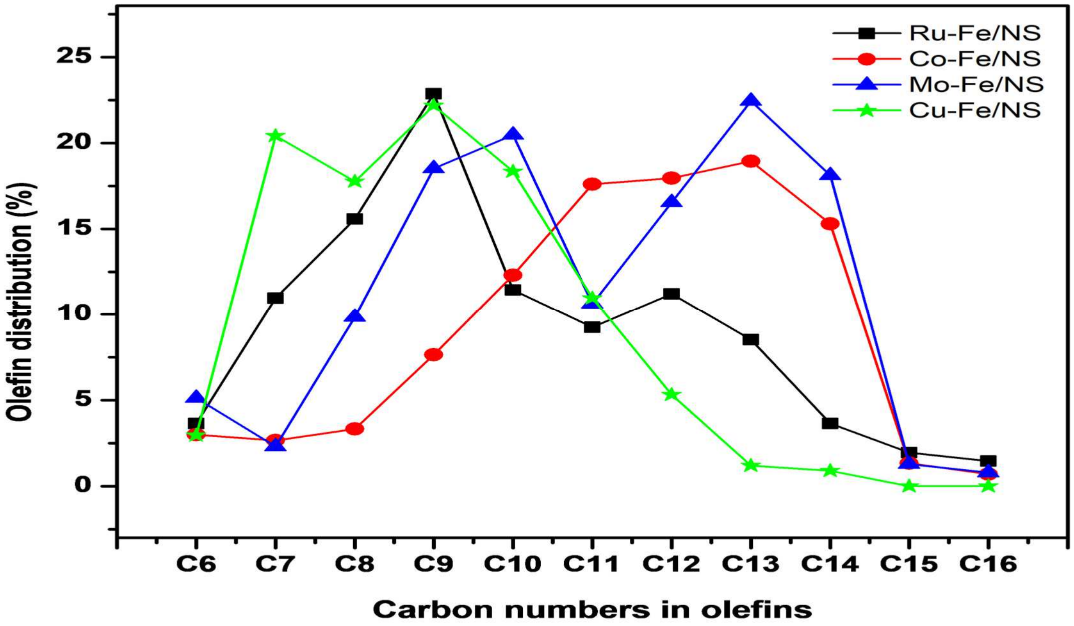

Figure 4.18. Olefin distribution (%) in liquid products, as a function of carbon number for promoted Fe/NS catalysts.

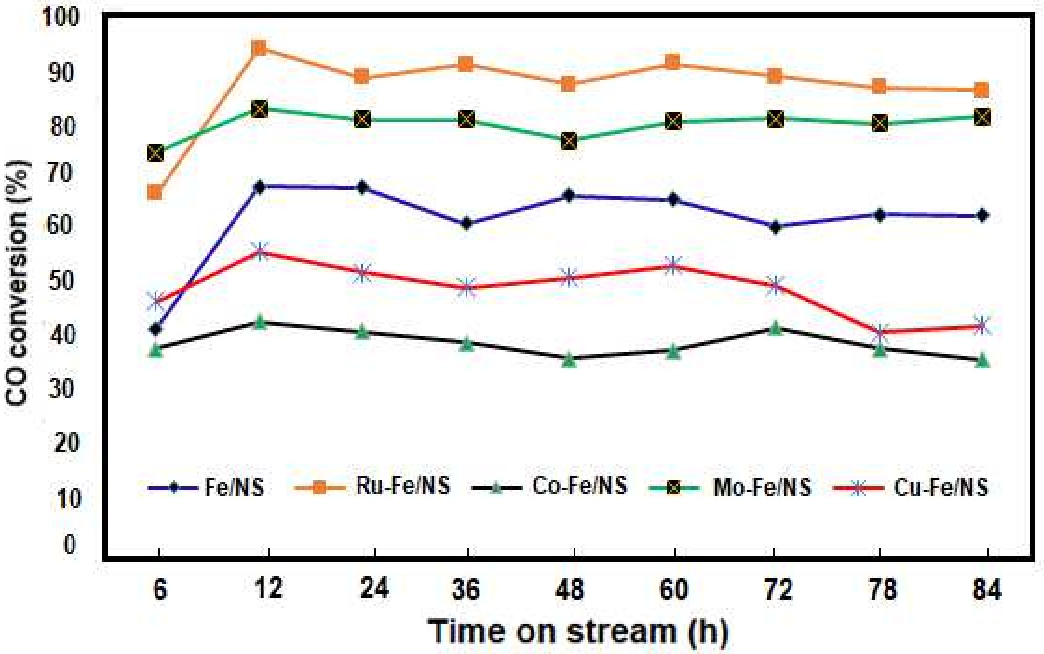

Figure 4.19. CO conversion with time on stream for promoted and unpromoted Fe/NS catalysts.

Table 4.3. The FT products identified by GC-MS for unpromoted Fe/NS catalyst reduced by H_2 at a temperature of 230 ^oC, and atmospheric pressure and H_2/CO =2.

Retention time (min)	Identified compounds	Mol(%)	M+ (m/z)
2.57	Benzene	2.78	78
3.07	1,3-Cyclopentadiene, 1,2-dimethyl	0.62	92
3.79	1-methyl-1 3-cyclohexadiene	0.5	92
4.21	Toluene	6.94	92
4.93	1-octene	0.9	112
6.10	1,5-Dimethyl-1,4-cyclohexadiene	0.47	108
6.53	Ethylbenzene	2.27	106
6.74	p-Xylene	3.15	106
7.35	Styrene	0.82	104
7.63	3-methyl heptane	0.46	114
9.22	n-Propylbenzene	0.63	120
9.69	α-Methyl-benzenemethanol	0.21	122
10.02	(1-methylethyl)benzene	0.27	120
10.47	1-ethyl-2-methylbenzene	1.25	118
10.57	Undecane, 4,5-dimethyl	0.03	184
11.33	1 2 3 trimethylbenzene	0.28	120
11.44	1-ethyl-2-methylbenzene	0.25	118
11.72	benzene 2-propenyl-	0.65	118
11.98	Indene	0.86	116
1218	1 4-diethylbenzene	0.36	134
12.23	1-methyl-3-propylbenzene	0.29	134
12.36	1,2,3,4,5,8-Hexahydronaphthalene	0.66	134
12.45	benzene 1-methyl-2-(1-methylethyl)-	0.18	134
13.11	Benzene 2-ethyl-1 4-dimethyl-	0.43	132
13.26	Benzene 1-methyl-4-(1-methylethyl)-	0.53	134
13.47	1-phenyl-1-butene	0.09	132
13.73	2,3-dimethylnonane	0.32	156
14.18	Benzene 1 3-diethyl-5-methyl-	0.08	148
14.68	1-methyl-indane	0.12	132
14.85	4 methyl indane	0.98	132
15.14	1-methylindene	0.35	130
15.30	3-ethyl indene	1.28	130
15.40	n-Pentylbenzene	0.35	148
16.14	Naphthalene	2.70	128
16.27	Benzene 1-methyl-3-(1-methyl-2-propenyl)	0.23	146
16.66	Undecane 4 7-dimethyl-	0.28	146
17.58	2 methylindene	0.25	184
18.17	Naphthalene, 1,2-dihydro-2-methyl	0.28	146
18.30	Naphthalene, 1,2-dihydro-3-methyl	0.27	144
18.45	Naphthalene, 1,2-dihydro-4-methyl	0.54	144
18.59	1,3-Dimethyl-1H-indene	0.37	144
19.26	2-methylnaphthalene	3.30	142

19.44	Undecane 4 6-dimethyl-	0.21	184
19.71	1H-indene,1 -ethylidene	0.86	144
21.52	Naphthalene 2-ethenyl-	0.34	154
21.89	Naphthalene 1-ethenyl-	139	156
22.05	Heptadecane 9-hexyl-	0.43	324
22.17	1 7-dimethylnaphthalene	1.30	156
22.55	2 3-dimethylnaphthalene	0.24	156
23.04	1 2-dimethylnaphthalene	0.35	156
24.16	Naphthalene 2-ethenyl-	0.89	156
24.18	Naphthalene 1-(2-propenyl)-	0.31	168
24.27	Naphthalene 1-propenyl-	0.34	170
24.55	Naphthalene 2-(1-methylethyl)-	0.94	170
26.51	IH-phenalene	0.14	166
26.79	Fluorene,14 dihydro	1.79	168
26.93	1-isopropenylnaphthalene	0.58	168
27.12	1-phenyl-2-methyl	0.77	168
29.07	9H-fluorene 2-methyl-	0.34	180
29.13	9H-fluorene 4-methyl-	0.63	180
30.83	9H-fluorene 9-methyl-	0.41	178

Table 4.4. The FT products identified by GC-MS for Ru-Fe/NS-S catalyst reduced by H_2 at a temperature of 230 ^{o}C, and atmospheric pressure and H_2/CO =2

Retention time (min)	Identified compounds	Mol(%)	M+ (m/z)
2.54	1-Heptene	3.88	98
2.64	2 3 4 trimethylhexane	0.62	128
2.74	Cyclopropane, 1-methyl-2-pentyl	0.28	126
2.85	Cyclohexane	0.26	84
3.39	3-methyl-1-heptene	0.88	112
3.54	4-methyl-1-heptene	1.52	112
3.69	5-methyl-1-heptene	1.11	112
3.84	3-methyl-heptene	0.31	114
4.11	2-methyl-1-heptene	0.42	112
4.22	Cyclopropane pentyl-	3.53	112
4.41	2 4-dimethylheptane	0.80	128
4.56	2-octene	0.46	112
4.74	Cyclobutane, 1,2-diethyl-, trans	0.48	112
5.57	3-methyl-1-octene	0.72	126
5.76	4-methyl-1-octene	0.72	126
5.79	1-nonene	2.09	126
5.99	6-methyl-1-octene	1.12	126
6.22	5-methyl decane	0.34	156
6.62	7-methyl decane	0.50	126
6.79	2-nonene	2.89	126

7.04	Nonene	1.01	128
7.20	2-Nonene, (E)	0.51	126
7.42	Cyclopropane 1-methyl-2-pentyl-	0.78	126
7.73	2 4-dimethyl-1-heptanol	0.50	144
7.94	Cyclopropane 1-methyl-pentyl-	0.08	126
8.21	Heptane, 2-methyl-3-methylene	0.13	126
8.43	3,7-dimethyl-1-octene	0.93	140
8.59	4 propyl heptane	1.82	142
8.71	1-Heptene, 6-methyl	0.31	112
8.86	3,7-dimethyl-1-octene	0.92	140
9.15	3-Methylnonane	0.28	142
9.23	2-ethyl-1-pentanol	0.16	116
9.59	2-methyl-1-nonene	0.49	140
9.79	1-Hexyl-2-methylcyclopropane	2.47	140.
10.06	Decane	1.08	142
10.23	3,3-Dimethyl-1-octene	0.80	140
10.46	2-Decene, (E)	0.70	140
10.60	1-Heptanol, 2-propyl	0.24	158
10.94	3,4-Dimethyl-1-decene	0.10	168
11.25	2-ethyl-4-methyl-1-pentanol	0.24	130
11.55	1-Methyl-2-octylcyclopropane	0.99	168
11.62	4-Methyl-1-decene	0.93	154
11.77	2,5,6-Trimethyl-decene	0.67	184
11.89	4-Methyl-decene	0.60	156
11.95	8-Methyl-decene	0.33	154
12.20	3-Methyl decane	0.71	156
12.32	8-methyl-2-decane	0.10	154
12.65	1-butyl-2-(2-methylpropyl)Cyclopropane	0.30	154
12.86	Cyclopropane, 1-butyl-2-methyl	1.83	154
13.02	3-Undecene,(E)-	0.32	154
13.11	Undecane	1.61	154
13.26	2-Undecene, (E)-	0.95	154
13.51	cyclopropane 1-methyl-2-pentyl-	0.69	154
13.89	1-heptanol 2-propyl-	0.14	158
14.49	cyclopropane 1-ethyl-2-heptyl-	1.40	168
14.62	4-Methyl-1-undecene	0.56	168
14.74	2 6-dimethyldecane	1.05	170
14.86	2 3-dimethyldecane	0.88	170
14.94	3-Undecene, 9-methyl-, (Z)-	0.38	168
15.19	Undecane, 2,3-dimethyl	0.83	184
15.61	2-Undecene, 10-methyl	0.42	186
15.82	cyclopropane nonyl-	1.43	168
15.93	4-Dodecene	0.67	168
16.07	Dodecane	2.63	168
16.21	2-Dodecene,(E)-	1.76	170
16.45	1-Dodecene	0.92	168
16.63	1-Heptanol, 2-propyl	0.36	158
16.84	2-Ethyl-1-decanol	0.31	186

17.29	1-Undecene, 8-methyl	0.30	168
17.37	3,7-Dimethyl-1-octene	0.70	140
17.51	6-methyl dodecane	0.82	184
17.71	Undecane, 2,3-dimethyl	0.88	184
17.86	2-Butyl-1-octanol	0.89	186
18.04	3-methyl dodecane	0.93	184
18.44	3,7-Dimethyl-1-octene	0.24	140
18.64	3-tetradecene (z)-	0.72	196
18.86	Tetradecane	2.87	184
18.99	6-Tetradecene	1.46	182
19.24	2-Methyl-1-undecanol	0.95	186
19.29	2-Ethyl-1-decanol	0.12	186
19.43	2-Isopropyl-5-methyl-1-heptanol	0.13	172
20.06	8-Methyl-1-undecene	0.44	168
20.19	6-methyl-tridecane	0.86	198
20.27	2,3-Dimethyl undecane	0.96	184
20.56	2,6-Dimethyl heptadecane	0.69	268
20.73	3-methyl tridecane	0.61	198
21.12	3,7-Dimethyl-1-octene	0.13	140
21.38	7-Tetradecene, (E)-	0.13	196
21.51	Tetradecane	2.44	198
21.63	3-Tetradecene, (Z)-	0.58	196
21.87	2-Methyl-1-undecanol	0.38	186
21.96	2-Ethyl-1-decanol	0.07	186
22.63	7-Methyl-2-decene	0.12	154
22.73	5-Ethyldecane	0.80	170
22.81	10-Methylnonadecane	0.49	282
22.96	4-Methyltetradecane	0.41	212
23.28	2,6-Dimethylheptadecane	0.39	268
23.90	2-Ethyl-1-decanol	0.11	186
24.02	2,6,11-Trimethyldodecane	1.69	212
24.12	2-Ethyl-1-decanol	0.42	186
25.12	5-propyl octane	0.65	184
25.24	5-methyl-pentadecane	0.28	226
25.52	2,3,5,8-tetramethyl	0.18	198
25.70	decane, 2,6,6,10-tetramethyl	0.21	212
26.39	Pentadecane	0.22	212
27.40	7-methyl pentadecane	0.18	226
28.65	Hexadecane	0.28	226
29.57	5-methyl-pentadecane	0.05	266

Table 4.5. The FT products identified by GC-MS for Mo-Fe/NS-I catalyst reduced by H_2 at a temperature of 230 °C, and atmospheric pressure and H_2/CO =2.

Retention time (min)	Identified compounds	Mol(%)	M+ (m/z)
2.48	Cyclobutane, 1,2-diethyl	4.55	112
3.33	Cyclohexane	1.34	84
3.47	Ethyl-1-butanol	1.85	102
3.62	5-Methyl-1-heptene	1.63	112
3.67	Toluene	0.21	92
4.04	2-Methyl-1-heptene	0.46	112
4.15	Cyclopropane, pentyl	5.71	112
4.33	3-Methylhexane	0.79	114
4.48	2-Octene	0.43	112
4.65	1,2-Dimethylcyclobutane	0.50	112
5.17	1,8-Nonadien-3-ol	0.19	140
5.35	2-cyclopropyl pentane	0.18	112
5.48	3-Methyl-1-octene	0.97	126
5.69	3-Methyl-1-butanol	2.88	130
5.90	6-Methyl-1-octene	1.51	126
6.12	3,6-Nonadien-1-ol	0.59	140
6.33	3-cyclopropyl pentane	0.28	112
6.52	7-Methyl-1-octene	0.89	126
6.94	Nonane	0.93	128
7.11	4-Nonene	0.44	126
7.32	cis-2-Nonene	0.76	126
7.84	3 6-nonadien-1-ol	0.12	140
8.33	3,7-Dimethyl-1-octene	1.06	140
8.49	(E)-6-Methyl-3-undecene	2.20	168
8.61	6-Methyl-1-heptene	0.38	112
8.76	2 4-dimethyl-1-octene	0.94	140
9.04	4-methyloctane	0.21	142
9.49	2-Methyl-1-nonene	0.47	140
9.68	1-Hexyl-2-methylcyclopropane	3.07	140
9.95	Decane	0.87	142
10.12	3 6-dimethyl-1-octene	1.83	140
10.35	Cyclobutane, 1-butyl-2-ethyl	0.59	140
11.14	3-Methyl-1-heptanol	0.21	130
1136	5-Decene, (E)	0.44	168
11.43	Cyclopropane, octyl	0.98	154
11.52	4-Methyl-1-decene	0.98	154
11.65	9-Methyl-1-decene	0.56	154
11.83	8-Methyl-1-decene	0.26	154
12.09	4-Methyl-1-undecene	0.52	168
12.20	6-methyl-1-heptanol	0.09	130
12.53	1-butyl-2-(2-methylpropyl)Cyclopropane	0.35	154
12.74	1-undecanol	2.13	172
13.00	Tridecane	0.91	184

13.15	2-Undecene	0.59	154
13.39	Cyclopropane, 1-pentyl-2-propyl	0.51	154
14.24	1-Heptanol, 2-propyl	0.74	158
14.51	8-Methyl-1-undecene	0.53	168
14.62	2,4-Dimethyl decane	.53	170
14.74	2,3-Dimethyldecane	0.32	170
15.70	Cyclopropane nonyl	1.32	168
15.94	Dodecane	0.88	170
16.08	3,7-Dimethyl-1-octene	0.63	140
16.32	2-Dodecene,(Z)	0.47	168
16.51	2-Propylheptanol	0.16	158
17.16	8-Methyl-1-undecene	0.21	168
17.25	9-Methyl-1-undecene	0.44	168
17.58	1-Hexanol, 5-methyl-2-(1-methylethyl)	0.35	158
17.75	2-Isopropyl-5-methyl-1-heptanol	0.33	172
17.91	3-methyl dodecane	0.31	184
18.32	6-Methyl-1-octene	0.19	126
18.74	Tridecane	0.96	184
18.87	6-Tridecene	0.57	182
19.12	2-Tridecene, (E)-	0.42	182
20.06	2-Methyl-2-octanol	0.40	144
20.27	2-Ethyl-1-decanol	0.38	186
20.98	10-Methyl-2-undecene	0.16	168
21.18	7-Tetradecene, (Z)-	0.9	196
21.38	Tetradecane	1.07	198
21.75	3-Tetradecene, (Z)-	0.36	196
22.42	8-Methyl-1-undecene	0.17	168
22.58	2-Mthyl-1-octanol	0.34	144
22.67	2-Butyl-1-octanol	0.32	186
23.15	2,6-Dimethylheptadecane	0.23	268
23.69	7-hexadecene (z)-	0.16	224
23.88	Pentadecane	0.91	121
23.99	2-Ethyl-1-dodecanol	0.43	214
24.37	2-Ethyl-1-decanol	0.03	186
24.97	5-Methyl-2-undecene	0.24	168
25.11	2-Butyl-1-octanol	0.22	186
25.25	2,3,4-Trimethyl decane	0.18	184
26.26	Pentadecane	0.52	212
26.63	Decane, 5-cyclohexyl	0.06	224
27.28	1-Heptanol, 2-propyl	0.23	158
27.32	2,3,5-Trimethylheptane	0.13	142
27.55	2,3,5,8-tetramethyl decane	0.12	198
27.85	3-Methylhexadecane	0.09	198
28.39	2-Ethyl-1-decanol	0.08	240
28.50	Pentadecane	0.05	186
28.60	2-Ethyl-1-decanol	0.48	212
29.042	4-Methyl-1-undecene	0.18	168
29.72	2,3,4-Trimethyldecane	0.06	184

Table 4.6. The FT products identified by GC-MS for Cu-Fe/NS-S catalyst reduced by H_2 at a temperature of 230 ^{o}C, and atmospheric pressure and H_2/CO =2

Retention time (min)	Identified compounds	Mol(%)	M+ (m/z)
2.22	Cyclohexane	2.06	84
2.49	1-Heptene	6.89	98
2.59	2 4-dimethylheptene	1.62	128
2.68	1-Methylpentyl Cyclopropane	141	126
2.79	3-Methyl-1-pentene	0.89	84
3.33	3-Methyl heptane	1.98	112
3.84	4-Methyl heptene	0.38	112
3.62	5-Methyl heptene	1.87	112
3.78	2-Methylheptane	0.84	114
1.05	6-Methyl heptane	0.84	112
4.15	1-Octene	3.97	112
4.34	Octane	2.40	114
4.49	2-Octene	1.70	112
4.66	Cyclobutane, 1,2-diethyl	1.32	112
5.16	1,8-Nonadien-3-ol	0.27	140
5.36	Pentane, 2-cyclopropyl	0.34	112
5.49	3-Methyl-1-octene	0.90	126
5.69	4-Methyl-1-octene	2.12	126
5.90	6-Methyl-1-octene	1.32	126
6.13	5,6-Dimethylundecane	0.93	184
6.33	4-Methyl-2-heptanol	0.65	130
6.53	Pentane, 2-cyclopropyl	0.76	112
6.70	1-Nonene	2.07	126
6.94	Nonane	2.30	128
7.32	2-Nonene,(Z)-	1.09	126
7.62	3-Methyl-1-heptanol	0.15	130
8.32	3,7-Dimethyl-1-octene	0.73	140
8.49	2-Methyl-1-octanol	1.26	144
8.75	3-Methylheptane	1.35	128
8.88	2,4,6-Trimethylheptane	0.22	142
8.97	6-Methylheptane	0.34	112
9.05	3-Methyl-nonane	0.60	142
9.11	3,4-Dimethyl-1-octene	0.31	140
9.20	3 5-dimethyl-1-octene	0.23	140
9.48	3 7-dimethyl-1-octene	0.23	140
9.68	2,6-Dimethyl-1-octene	1.18	140
9.85	2-Methyl-3-nonene	0.38	140
9.94	Decane	1.82	142
10.11	3-Decene	0.90	140
10.35	5-Decene	0.73	140
11.45	1-Octanol, 2-methyl	0.41	144
10.49	4-Methyl-1-undecene	0.36	168

11.66	5-Methyldecane	0.72	156
11.77	4-Methyldecane	0.83	156
11.92	1-Heptanol, 2-propyl	0.69	158
12.09	5-methyl-decane	0.95	184
12.74	4-Undecene,(E)-	0.59	154
14.89	4-Methyl-1-undecene	0.38	168
15.07	3-Methylundecane	0.61	170
15.70	2,6-Dimethyl-3-octene	0.29	140
15.80	5-Undecene, 4-methyl	0.32	168
15.94	Dodecane	2.04	170
16.08	8-Methyl-1-undecene	0.32	168
16.30	2,5,6-Trimethyldecane	0.28	184
17.44	5-Methyldecane	0.55	184
17.58	2,3,4-Trimethyldecane	0.67	184
17.74	2,8-Dimethylundecane	0.43	184
17.92	3-methyl dodecane	0.46	184
18.74	Tridecane	1.98	184
19.16	Decane, 2,4,6-trimethyl	0.24	184
20.06	Tridecane, 6-methyl	0.49	198
20.14	Tridecane, 5-methyl	0.41	198
20.26	Decane, 2,3,5,8-tetramethyl	0.37	198
20.43	3-methyl decane	0.32	184
20.60	3-methyl tridecane	0.35	186
21.39	Pentadecane	1.42	212
21.71	2,7,10-Trimethyldodecane	0.15	212
22.61	6-methyl-tridecane	0.43	198
22.69	5-Methyldodecane	0.22	184
22.83	2,8-Dimethylundecane	0.18	184
23.15	Dodecane, 2,6,10-trimethyl	0.17	184
23.89	Decane, 6-ethyl-2-methyl	0.88	184

Table 4.7. The FT products identified by GC-MS for Co- Fe/NS-P catalyst reduced by H_2 at a temperature of 230 ^oC, and atmospheric pressure and H_2/CO =2

Retention time (min)	Identified compounds	Mol(%)	M+ (m/z)
2.55	Cyclohexane	2.26	84
3.53	pentane, 2-cyclopropyl	0.53	112
4.22	Cyclobutane, 1,2-diethyl	1.82	112
5.58	Cyclopentane, 1,3-dimethyl	0.24	84
57.8	4-Methyl-1-heptanol	0.90	130
5.99	3-Methyl-1-heptanol	0.43	130
6.79	Cyclobutane, butyl	1.62	112
7.03	3-ethylhexane	0.22	114
8.43	3-Methyl-1-heptene	0.39	112
8.60	2-Propyl-1-pentanol	0.84	130

8.71	1-octanol	0.18	130
8.87	6-Methyl-1-heptene	0.33	112
9.61	3,4-Dimethyl-1-hexene	0.10	112
9.80	1-Nonene	1.26	126
10.06	Heptane, 2,4-dimethyl	0.32	128
10.47	6-Methyl-1-octene	0.20	126
11.63	4-Methyl-2-propyl-1-pentanol	0.59	144
11.77	2-Propyl-1-pentanol	0.33	116
11.95	4-Methyl-1-octene	0.27	126
12.21	2,3, 4-trimethylhexane	0.23	128
12.66	7-Methyl-1-octene	0.14	126
12.86	1-Decene	1.77	140
13.12	Decane	0.54	142
13.28	3,7-Dimethyl-1-octene	0.33	140
13.54	6-methyl-1-heptanol	0.32	130
14.48	2,6-Dimethyl-3-octene	1.59	140
14.62	1-Hexanol, 5-methyl-2-(1-methylethyl)	0.90	158
15.62	9-Methyl-1-decene	0.52	154
15.83	1-Undecene	3.59	168
16.07	Octane, 2,3,7-trimethyl	1.40	154
16.21	n-octyl-cyclopropane	1.15	168
16.45	8-Methyl-1-undecene	1.11	168
17.29	9-Methyl-1-undecene	0.74	168
17.38	1-Methyl-2-octylcyclopropane	1.46	168
17.50	3,4-Dimethyl-1-decene	1.29	168
17.63	5-Methyl-1-undecene	0.70	168
17.87	2-Methyl-1-dodecanol	0.79	168
18.04	3-methyl dodecane	0.68	186
18.64	1-Tridecene	3.35	184
18.87	Dedecane	2.16	170
19.00	3-Tridecene,(E)-	1.30	182
19.25	2-Tridecene,(E)-	1.21	182
20.20	2-Ethyl-1-decanol	1.06	186
21.31	3-Tetradecene,(E)-	1.85	198
21.51	2,3,5,8-Tetramethyl-decane	1.18	198
21.64	7-Tetradecene, (E)-	1.29	196
21.88	3-Tetradecene, (E)-	0.93	196
22.54	4-Tetradecene, (E)-	0.56	196
22.81	2-Hexyl-1-octanol	0.52	214
24.02	Dodecane,2,6,10-trimethyl	1.32	212

4.5 Conclusion

Fe/NS catalysts with and without Ru, Co, Mo and Cu promoters were synthesized by impregnation method, and investigated for hydrogenation of CO. The addition of promoters was observed to have a significant effect on the physico-chemical properties of Fe/NS catalyst, such as the surface area, crystallite size of iron oxide, the adsorption and reduction behavior, as well as catalytic performance including the catalytic activity, stability and selectivity during FTS. XRD and XPS results of the promoted Fe/NS catalysts revealed that RuO_2, Co_3O_4, CuO and $Fe2(MoO_4)_3/MoO_3$ phases were presented on the Ru-Fe/NS, Co-Fe/NS, Cu-Fe/NS and Mo-Fe/NS catalysts. The FTS products over unpromoted Fe/NS catalyst mainly consists of a high content of aromatics and low contents of n-olefins and n-paraffins. Furthermore, based on the FTS results of our studies, we found that the addition of Ru, Co, Mo and Cu promoters to Fe/NS catalysts increased the Co conversion, shifted the FTS product distributions and improved the selectivity towards C_6-C_{16} olefins instead of aromatics in unpromoted Fe/NS catalyst. Overall, our findings could have implications for designing a promoter-modified catalyst with improved catalyst for direct conversion of syngas to a wide range of olefins hydrocarbons.

CHAPTER 5: CONCLUSION

5.1 Conclusions

The main objectives of the dissertation were to prepare, characterize and evaluate the physicochemical properties of silica nanosprings (NS) as a new support for Fe and Co (FT) catalysts for biofuel production, combined with the use of promoters (i.e. Cu, Mo and Ru addition). Unpromoted Co/NS, Fe/NS and promoted Fe/NS catalysts with the different metals such as Co, Mo, Cu and Ru were successfully synthesized by various techniques and employed to investigate effects of physico-chemical properties and catalytic behavior of Fe and Co catalysts during the FTS. However, catalyst preparation, evaluation of FT catalytic performance, and activation are the most important steps in the design of FT catalysts. Since Co and Fe are the only two transition metal oxides (catalysts) of choice for industrial applications, because of their relatively low cost and high activity for FTS, experiments carried out on silica 1D NS supported Fe and Co catalysts to study the effects of each the above parameters on the performance criteria of these catalysts, including CO conversion, hydrocarbons product selectivity, catalyst stability and liquid hydrocarbon product composition. The following summarizes the main findings to specific objectives outlined for this study:

(i) The first study (Chapter Two) was to investigate the effect of reduction temperature (409 and 609^{o}C) on the performance of Co/NS catalysts as well as to make comparisons between silica NS supported Co catalyst and conventional silica gel-supported Co catalysts in terms of CO hydrogenation. Two catalysts (Co/SiO_2 and Co/NS) were catalysts were prepared by impregnation method, and investigated in FTS under similar conditions but at two different reduction temperatures. The catalysts were characterized using a variety of techniques. Co/NS catalyst showed smaller Co_3O_4 particles, better dispersion, and higher reduction temperature than the conventional Co/SiO_2-gel. Moreover, the study of catalytic performance of the Co/NS catalyst has revealed that the CO conversion increased with the reduction temperature of ~ 600 ^oC, it showed the highest catalytic activity with the 88% Co conversion (%). In addition to the high CO conversion, Co/NS catalyst also showed higher production rate of C_6-C_{17} hydrocarbons than the catalyst reduced at 409 ^oC. From the catalytic tests carried out in this study can concluded that silica NS has potential to enhance the catalytic activity of the Co/NS for FT compared with conventional Co/SiO_2-gel catalyst.

(ii) The second approach (Chapter Three) was to evaluate the influence of synthesis and activation methods on catalytic properties of Fe/NS catalyst. A number of experiments were conducted with various catalyst preparation (impregnation, precipitation and sol-gel) methods and different reducing agents (H_2, CO or H_2+CO mixture). The Fe/NS catalysts were characterized to see what changes had occurred during the different preparation methods that might influence on FTS. In this study, we found that the different catalyst preparation methods were able to produce Fe nanoparticles with different particle sizes and Fe phases, which can affect the catalytic performance of Fe/NS catalyst. In addition, it was found that the Fe/NS-I catalyst prepared using wetness impregnation and activated by CO has highest activity and its selectivity falls within the range of gasoline C_6–C_{14}.

(iii) The third approach (Chapter Four) involved the use of Ru, Mo, Co and Cu promoters in order to study their influence of on the activity and selectivity of Fe/NS catalyst for FTS. Four promoted Fe/NS catalysts were prepared by co-impregnation method and were evaluated in a quartz fixed-bed micro reactor.

Among the promoters studied Ru gave the highest distribution of products to C_6-C_{16} of 89.3%. The main product obtained for promoted Fe/NS catalysts was olefins, while the highest selectivity towards aromatics was obtained over unpromoted Fe/NS catalyst. Furthermore, the catalytic activities obtained for promoted Mo-Fe/NS catalyst is closed to the value of CO conversion (82.4%). The FTS hydrocarbons products under promoted Fe/NS catalysts were found to be qualitatively similar but not quantitatively. The promoted Fe/NS catalysts also demonstrated higher olefin to paraffin selectivity compared to unpromoted Fe/NS catalyst. In order to better investigate the stability of promoted and unpromoted Fe/NS catalyst, the FT reaction time was extended to 84 h. It was observed that no significant deactivation in catalytic stability has been observed during the 84 h run of the FT reaction. From the results obtained for the promotion of Fe/NS catalysts it can be concluded that the Ru, Mo, Co and Cu can be used as promoters to adjust a desired FTS product distribution and enhance the catalytic activity of Fe/NS catalysts.

In summary, on the basis of these findings we believe that that silica 1D NS is an excellent support for FT catalysts for improving the catalytic activity and developing new FT catalysts. Besides that, the effects of silica NS have a highly positive effect on performance of FT catalysts in terms of activity and selectivity. The success of this distraction shows that there is an avenue for using silica NS as attractive support for manufacturing synthetic liquid hydrocarbons fuels and chemicals on the basis of the FTS from alternative feedstock.

5.2 Future Work

Based on the work carried out in this dissertation the future work arising from these studies is are proposed for better understanding of FTS process. Only various catalyst preparation methods, different reduction temperature, different promoters and activation methods were employed to study effects these parameters on the properties and catalytic performance of silica (NS) supported Co and Fe catalysts. However, more FT pretreatments are going to be carried out in the future, such as the influence of different Co-supports effects (e.g. Al_2O_3 and TiO_2) on of silica (NS) supported Co and Fe catalysts, the influence incorporation with relatively inexpensive and abundant promoters (e.g. Zn, Mn, Pb, Cr, Cd, etc.) and expanding the use of nanosprings supports (e.g. Al_2O_3 and TiO_2) nanosprings. Additionally, the FTS experiments of silica (NS) supported Co and Fe catalysts could also be conducted on a large-scale experimental testing in order to produce renewable hydrocarbon biofuels (diesel or jet fuel, or gasoline), and then characterize their chemical and physical properties including density, viscosity, acid value, flash point, water content, combustion, etc. These tests will allow to make specific comparisons between FT fuel product and conventional diesel, jet fuel, and gasoline, as well as with renewable fuel standard requirements.

REFERENCES

1. Jahangiri, H., et al., *A review of advanced catalyst development for Fischer–Tropsch synthesis of hydrocarbons from biomass derived syn-gas.* Catalysis Science & Technology, 2014. **4**(8): p. 2210-2229.
2. Dad, M., *From 2D to 3D: Development, characterization and testing of a well-defined Fe-Mn/SiO2 Fischer− Tropsch model catalyst*. 2016, Ph. D. Thesis, Technische Universiteit Eindhoven, Eindhoven, The Netherlands.
3. Koontasang, Y., *Two-Stage Synthesis of Liquid Fuels from Carbon Dioxide and Methane*. 2006: Kasetsart University.
4. Zhang, S., *Production of Transportation Fuel Range Middle Distillates via Fischer-Tropsch Synthesis with Integrated Product Upgrading under Supercritical Phase Conditions*. 2013, Auburn University.
5. Dad, M., *From 2D to 3D: development, characterization and testing of a well-defined Fe-Mn/SiO2 Fischer-Tropsch model catalyst*. 2016, Technische Universiteit Eindhoven Eindhoven, The Netherlands.
6. Subiranas, A.M., *Combining Fischer-Tropsch synthesis (FTS) and hydrocarbon reactions in one reactor*. 2008: Univ.-Verlag Karlsruhe.
7. Timmons, D., J.M. Harris, and B. Roach, *The economics of renewable energy.* Global Development And Environment Institute, Tufts University, 2014: p. 52.
8. SAVARE, P. and F. SALZANI, *New insights on Pt promotion of Co/γ-Al2O3 catalysts for Fischer Tropsch synthesis.* 2016.
9. Spath, P.L. and D.C. Dayton, *Preliminary screening-technical and economic assessment of synthesis gas to fuels and chemicals with emphasis on the potential for biomass-derived syngas*. 2003, National Renewable Energy Lab Golden Co.
10. Jahangiri, H., et al., *A review of advanced catalyst development for Fischer–Tropsch synthesis of hydrocarbons from biomass derived syn-gas.* Catal. Sci. Technol., 2014. **4**(8): p. 2210-2229.
11. Boerrigter, H. and R. Rauch, *Review of applications of gases from biomass gasification.* ECN Biomassa, Kolen en Milieuonderzoek, 2006. **20**.
12. Hu, J., F. Yu, and Y. Lu, *Application of Fischer–Tropsch synthesis in biomass to liquid conversion.* Catalysts, 2012. **2**(2): p. 303-326.
13. Kumar, A., D.D. Jones, and M.A. Hanna, *Thermochemical biomass gasification: a review of the current status of the technology.* Energies, 2009. **2**(3): p. 556-581.
14. Wood, D.A., C. Nwaoha, and B.F. Towler, *Gas-to-liquids (GTL): A review of an industry offering several routes for monetizing natural gas.* Journal of Natural Gas Science and Engineering, 2012. **9**: p. 196-208.
15. Dry, M. and A. Steynberg, *Fischer-Tropsch Technology. Studies in Surface Science and Catalysis*. 2004: Elsevier Science & Technology.
16. van der Laan, G.P., *Kinetics, selectivity and scale up of the Fischer-Tropsch synthesis*. 1999: [University Library Groningen][Host].
17. Forman, G.S., T.E. Hahn, and S.D. Jensen, *Greenhouse gas emission evaluation of the GTL pathway.* Environmental science & technology, 2011. **45**(20): p. 9084-9092.
18. Donado Sainz de la Maza, E., *Cobalt supported on mesoporous silicas for the Fischer-Tropsch synthesis*. 2012.
19. Bahome, M.C., *Synthesis and use of carbon nanotubes as a support for the Fischer-Tropsch Synthesis*. 2007, Faculty of Engineering and the Built Environment, University of the Witwatersrand, Johannesburg.

20. Trepanier, M., *Promoted Co-CNT nano-catalyst for green diesel production using Fischer-Tropsch synthesis in a fixed bed reactor*. 2010.
21. Thommes, K. and V. Strezov, *Fischer–Tropsch Synthesis from Biosyngas.* Biomass Processing Technologies, 2014: p. 309.
22. Lualdi, M., *Fischer-Tropsch Synthesis over Cobalt-based Catalysts for BTL Application*, in *Chemical Engineering*. 2012, KTH School of Chemical Science and Engineering Stockholm, Sweden. p. 95.
23. *Series Page*, in *Advances in Chemical Engineering*, M.V.G. Kevin, Editor. 2016, Academic Press. p. ii.
24. Todić, B.S., *Kinetic modeling and optimization of fixed-bed reactor for Fischer-Tropsch synthesis*, in *Technology and Metallurgy* 2015, University of Belgrade: Belgrade. p. 219.
25. Arndt, A.A.M.A.S., *Chemical Energy Storage*. 2012, Germany: De Gruyter.
26. Fronzo, A., *Biomass to Liquid Process: new kind of cobalt and iron based catalysts for the Fischer-Tropsch Synthesis.* 2014.
27. Gates, B.C., H. Knoezinger, and F.C. Jentoft, *Advances in Catalysis*. 2011: Academic Press/Elsevier.
28. Lohithar, N., *FORMATION OF ACTIVE CATALYTIC SITES IN HYDROCARBON SYNTHESIS AND REACTION* 2008, Clemson University: South Carolina, USA. p. 205.
29. Hexana, W.M., *A systematic study of the effect of chemical promoters on the precipitated Fe-based Fischer-Tropsch Synthesis catalyst* in *chemical Engineering*. 2009, University of the Witwatersrand: Johannesburg. p. 178.
30. Osakoo, N., *INFLUENCE OF SUPPORT AND REDUCTION PROMOTER ON ACTIVITY OF COBALT CATALYSTS FOR FISCHER-TROPSCH SYNTHESI*, in *Chemistry*. 2014, Suranaree University of Technology Thailand. p. 181.
31. Dalai, A. and B. Davis, *Fischer–Tropsch synthesis: a review of water effects on the performances of unsupported and supported Co catalysts.* Applied Catalysis A: General, 2008. **348**(1): p. 1-15.
32. Oues, A.K., *Studying the fischer tropsch synthesis on alumina support cobalt base catalyst in fixed bed reactor*. 2013.
33. Colmyer, R.J., *Fischer-Tropsch synthesis: Using nanoparticle oxides as supports for cobalt-based Fischer-Tropsch catalysts*. 2011: University of Florida.
34. Campen, A., *Fly ash zeolite catalyst support for Fischer-Tropsch synthesis*. 2012: Southern Illinois University at Carbondale.
35. Mabry, J.C., *Utilization of cobalt catalyst for high temperature Fischer-Tropsch synthesis in a fluidized bed reactor*. 2014: Southern Illinois University at Carbondale.
36. van de Loosdrecht, J., et al., *Fischer–Tropsch Synthesis: Catalysts and Chemistry*. Vol. 7. 2013. 525-557.
37. Doss, T., *Low severity Fischer-Tropsch synthesis for the production of synthetic hydrocarbon fuels*. 2012, Aston University.
38. Li, Y., *Development of a Fischer-Tropsch Gasoline Process for the Steam Hydrogasification Technology.* 2013.
39. Håvik, S., *SiC supported Co catalysts for the Fischer-Tropsch synthesis*, in *Chemical Engineering*. 2012, Norwegian University of Science and Technology: Norway. p. 117.
40. Zhang, Q., J. Kang, and Y. Wang, *Development of novel catalysts for Fischer–Tropsch synthesis: tuning the product selectivity.* ChemCatChem, 2010. **2**(9): p. 1030-1058.
41. Musanda Mukenz, T., *Graphical methods for the representation of the Fischer-Tropsch reaction: towards understanding the mixed iron-cobalt catalyst systems*. 2011.
42. Nozonke, D., *Iron Modification of Rhodium Nano-crystallites for CO Hydrogenation*, in *chemical Engineering*. 2013, University of Cape Town: South African

43. Sango, T., *Nitrogen-containing compounds from ammonia co-feed to the Fischer-Tropsch synthesis*, in *Engineering*. 2013, University of Cape Town South Africa. p. 134
44. James, O.O., B. Chowdhury, and S. Maity, *TPR and TPD studies of effects of Cu and Ca promotion on Fe–Zn-based Fischer–Tropsch catalysts.* Journal of Chemical Sciences, 2013. **125**(3): p. 679-686.
45. Bell, T. and L. Torrente-Murciano, *H2 Production via Ammonia Decomposition Using Non-Noble Metal Catalysts: A Review.* Topics in Catalysis, 2016. **59**(15-16): p. 1438-1457.
46. Khodakov, A.Y., W. Chu, and P. Fongarland, *Advances in the development of novel cobalt Fischer− Tropsch catalysts for synthesis of long-chain hydrocarbons and clean fuels.* Chemical reviews, 2007. **107**(5): p. 1692-1744.
47. Arsalanfar, M., et al., *Effect of support and promoter on the catalytic performance and structural properties of the Fe–Co–Mn catalysts for Fischer–Tropsch synthesis.* Journal of Industrial and Engineering Chemistry, 2014. **20**(4): p. 1313-1323.
48. Mirzaei, A.A., et al., *A review of Fischer-Tropsch synthesis on the cobalt based catalysts.* Physical Chemistry Research, 2014. **2**(2): p. 179-201.
49. Dasgupta, D. and T. Wiltowski, *Enhancing gas phase Fischer–Tropsch synthesis catalyst design.* Fuel, 2011. **90**(1): p. 174-181.
50. Alagiri, P., *Fischer-Tropsch synthesis on commercially available carbon nanotubes*. 2016, Southern Illinois University at Carbondale.
51. North, M., *Sustainable Chemistry: With Non-Endangered Metals Part 1*. 2015: Royal Society of Chemistry.
52. Liu, Y., *Silicon carbide and nano-carbons containing cobalt catalysts for the Fisher-Tropsch synthesis*. 2013, Université de Strasbourg.
53. Keyvanloo, K., *Preparation of Active, Stable Supported Iron Catalysts and Deactivation by Carbon of Cobalt Catalysts for Fischer-Tropsch Synthesis*, in *Chemical Engineering* 2014, Brigham Young University Provo,USA. p. 219.
54. Kababji, A.H., B. Joseph, and J.T. Wolan, *Silica-Supported Cobalt Catalysts for Fischer–Tropsch Synthesis: Effects of Calcination Temperature and Support Surface Area on Cobalt Silicate Formation.* Catalysis Letters, 2009. **130**(1-2): p. 72-78.
55. Abbaslou, M.R.M., *Iron Catalyst Supported on Carbon Nanotubes for Fischer-Tropsch Synthesis: Experimental and Kinetic Study*, in *Chemical Engineering* 2010, University of Saskatchewan: Canada. p. 207.
56. Peluso, E., *Eggshell Catalyst for Hydrocarbon Synthesis: Kinetic Modeling and Reactor Performance*, in *Chernical and Biochemical Engineering* 1998, University of Western Ontario: London ,Ontario. p. 232.
57. Pokhrel, S., *Fischer-Tropsch synthesis on functionalized carbon nanotubes*. 2014.
58. Liu, J.-Y., J.-F. Chen, and Y. Zhang, *Cobalt-imbedded zeolite catalyst for direct syntheses of gasoline via Fischer–Tropsch synthesis.* Catalysis Science & Technology, 2013. **3**(10): p. 2559.
59. Wang, Z., et al., *Design and synthesis of 3D ordered macroporous ZrO2/Zeolite nanocomposites.* Microporous and Mesoporous Materials, 2009. **120**(3): p. 351-358.
60. Mokhonoana, M.P. and N.J. Coville, *Highly Loaded Fe-MCM-41 Materials: Synthesis and Reducibility Studies.* Materials, 2009. **2**(4): p. 2337-2359.
61. Bahome, M.C., et al., *Fischer–Tropsch synthesis over iron catalysts supported on carbon nanotubes.* Applied Catalysis A: General, 2005. **287**(1): p. 60-67.
62. Klettlinger, J.L.S., *Fischer-Tropsch Cobalt Catalyst Improvements with the Presence of TiO2, La2O3, and ZrO2 on an Alumina Support.* 2012.

63. Norton, M.G., et al. *Silica Nanosprings–a novel nanostructured material for hydrogen storage*. in *Proc. Clean Technology Conference, Houston*. 2009.
64. Klaigaew, K., et al., *Effect of preparation methods on activation of cobalt catalyst supported on silica fiber for Fischer–Tropsch synthesis.* Chemical Engineering Journal, 2015. **278**: p. 166-173.
65. Hass, J.L., et al., *Synthetic osteogenic extracellular matrix formed by coated silicon dioxide nanosprings.* J Nanobiotechnology, 2012. **10**: p. 6.
66. Wang, L., et al., *High yield synthesis and lithography of silica-based nanospring mats.* Nanotechnology, 2006. **17**(11): p. S298-S303.
67. Timalsina, Y.P., et al., *Alternating current impedance spectroscopic analysis of biofunctionalized vertically-aligned silica nanospring surface for biosensor applications.* Journal of Applied Physics, 2011. **110**(1): p. 014901.
68. Sai, V., et al., *Silica nanosprings coated with noble metal nanoparticles: Highly active SERS substrates.* The Journal of Physical Chemistry C, 2010. **115**(2): p. 453-459.
69. Luo, G., et al., *A novel nano fischer-tropsch catalyst for the production of hydrocarbons.* Environmental Progress & Sustainable Energy, 2014. **33**(3): p. 693-698.
70. Kengne, B.-A.F., et al., *Preparation, surface characterization and performance of a Fischer-Tropsch catalyst of cobalt supported on silica nanosprings.* Applied Surface Science, 2015. **359**: p. 508-514.
71. Nanduri, A., *Catalyst-scale modeling and simulation of a fixed-bed reactor for Fischer-Tropsch synthesis*. 2014, Texas A&M University-Kingsville.
72. Jayan, A., et al., *An Overview of Ferrous and Cobalt Catalysts Used in the Conversion of Synthetic Gas to Fuels.*
73. Sheng, M., *Enhanced Heat Transfer Catalyst Structures for Fischer-Tropsch Synthesis*. 2012: Auburn University.
74. van der Lee, G., et al., *Manipulation of the selectivity of rhodium by the use of supports and promoters.* Journal of the Chemical Society, Faraday Transactions 1: Physical Chemistry in Condensed Phases, 1987. **83**(7): p. 2103-2112.
75. Morales, F. and B.M. Weckhuysen, *Promotion effects in Co-based Fischer-Tropsch catalysis.* Catalysis, 2006. **19**(1).
76. Rafati, M., L. Wang, and A. Shahbazi, *Effect of silica and alumina promoters on co-precipitated Fe–Cu–K based catalysts for the enhancement of CO 2 utilization during Fischer–Tropsch synthesis.* Journal of CO2 Utilization, 2015. **12**: p. 34-42.
77. Hole, N.-O.A., *Effects of Potassium and Copper Promoters on Iron Fischer-Tropsch Catalysts*. 2015, NTNU.
78. Munnik, P., P.E. de Jongh, and K.P. de Jong, *Recent developments in the synthesis of supported catalysts.* Chemical reviews, 2015. **115**(14): p. 6687-6718.
79. Perego, C. and P. Villa, *Catalyst preparation methods.* Catalysis Today, 1997. **34**(3-4): p. 281-305.
80. Ward, D.A. and E.I. Ko, *Preparing catalytic materials by the sol-gel method.* Industrial & engineering chemistry research, 1995. **34**(2): p. 421-433.
81. Atalay, S. and G. Ersöz, *Novel Catalysts in Advanced Oxidation of Organic Pollutants*. 2016: Springer.
82. Rytter, E. and A. Holmen, *Deactivation and regeneration of commercial type Fischer-Tropsch Co-catalysts—A mini-review.* Catalysts, 2015. **5**(2): p. 478-499.
83. De Klerk, A., *Fischer-Tropsch Refining*. 2012: John Wiley & Sons.
84. Bartholomew, C.H., *Mechanisms of catalyst deactivation.* Applied Catalysis A: General, 2001. **212**(1): p. 17-60.

85. Moulijn, J.A., A. Van Diepen, and F. Kapteijn, *Catalyst deactivation: is it predictable?: What to do?* Applied Catalysis A: General, 2001. **212**(1): p. 3-16.
86. Bian, G., et al., *Studies with a precipitated iron Fischer-Tropsch catalyst reduced by H 2 or CO.* Journal of Molecular Catalysis A: Chemical, 2002. **186**(1): p. 203-213.
87. Mai, K., *Effects of Different Preparation Methods on Structure and Catalytic Behavior of Iron-Based Catalyst via Fischer Trospch Synthesis of Biomass-Derived Syngas.* 2014.
88. Luo, M., H. Hamdeh, and B.H. Davis, *Fischer-Tropsch Synthesis: Catalyst activation of low alpha iron catalyst.* Catalysis today, 2009. **140**(3): p. 127-134.
89. Stevens, C., *Thermochemical processing of biomass: conversion into fuels, chemicals and power*. 2011: John Wiley & Sons.
90. Ernst, B., et al., *Study on a cobalt silica catalyst during reduction and Fischer–Tropsch reaction: in situ EXAFS compared to XPS and XRD.* Catalysis today, 1998. **39**(4): p. 329-341.
91. Ojeda, M. and S. Rojas, *Biofuels from Fischer-Tropsch Synthesis*. 2010: Nova Science Publishers.
92. Perego, C., *Development of a Fischer-Tropsch catalyst: From laboratory to commercial scale demonstration.* Rendiconti Lincei, 2007. **18**(4): p. 305-317.
93. Jacobs, G., et al., *Fischer–Tropsch synthesis: support, loading, and promoter effects on the reducibility of cobalt catalysts.* Applied Catalysis A: General, 2002. **233**(1): p. 263-281.
94. Bertole, C.J., C.A. Mims, and G. Kiss, *Support and rhenium effects on the intrinsic site activity and methane selectivity of cobalt Fischer–Tropsch catalysts.* Journal of Catalysis, 2004. **221**(1): p. 191-203.
95. Storsæter, S., et al., *Characterization of alumina-, silica-, and titania-supported cobalt Fischer–Tropsch catalysts.* Journal of catalysis, 2005. **236**(1): p. 139-152.
96. Luo, G., et al., *A novel nano fischer-tropsch catalyst for the production of hydrocarbons.* Environmental Progress & Sustainable Energy, 2014. **33**(3): p. 693-698.
97. Ahmadipour, M., M. Hatami, and K.V. Rao, *Preparation and characterization of nano-sized (Mg (x) Fe (1–x) O/SiO 2)(x= 0.1) core-shell nanoparticles by chemical precipitation method.* 2012.
98. Thyssen, V.V., T.A. Maia, and E.M. Assaf, *Cu and Ni Catalysts Supported on γ-Al2O3 and SiO2 Assessed in Glycerol Steam Reforming Reaction.* Journal of the Brazilian Chemical Society, 2015. **26**(1): p. 22-31.
99. Park, K., et al., *Structural and magnetic properties of gold and silica doubly coated γ-Fe2O3 nanoparticles.* The Journal of Physical Chemistry C, 2007. **111**(50): p. 18512-18519.
100. Kandula, S. and P. Jeevanandam, *A facile synthetic approach for SiO 2@ Co 3 O 4 core–shell nanorattles with enhanced peroxidase-like activity.* RSC Advances, 2015. **5**(7): p. 5295-5306.
101. Xie, R., et al., *Silylated Co 3 O 4-m-SiO 2 catalysts for Fischer–Tropsch synthesis.* Catalysis Communications, 2011. **12**(7): p. 589-592.
102. Li, Y., et al., *Surface molecular imprinting onto fluorescein-coated magnetic nanoparticles via reversible addition fragmentation chain transfer polymerization: a facile three-in-one system for recognition and separation of endocrine disrupting chemicals.* Nanoscale, 2011. **3**(1): p. 280-287.
103. Musić, S., N. Filipović-Vinceković, and L. Sekovanić, *Precipitation of amorphous SiO2 particles and their properties.* Brazilian journal of chemical engineering, 2011. **28**(1): p. 89-94.
104. Nabid, M.R., Y. Bide, and M. Abuali, *Copper core silver shell nanoparticle–yolk/shell Fe 3 O 4@ chitosan-derived carbon nanoparticle composite as an efficient catalyst for catalytic epoxidation in water.* RSC Advances, 2014. **4**(68): p. 35844-35851.
105. Moghanian, H., et al., *Sulfanilic acid-functionalized silica-coated magnetite nanoparticles as an efficient, reusable and magnetically separable catalyst for the solvent-free synthesis of 1-amido-and 1-aminoalkyl-2-naphthols.* RSC Advances, 2014. **4**(54): p. 28176-28185.

106. Rafiee, H.R., et al., *Preparation and Characterization of Promoted Fe-V/SiO 2 Nanocatalysts for Oxidation of Alcohols.* Journal of Chemistry, 2013. **2013**.
107. Andrew David Hix, M.M., Rachel Kendall, Rachel Svoboda, William Maningas *Gas to Liquids (GTL)* in *Process Design and Economic Analysis* 2012, University of Tennessee Honors
108. Wu, H., et al., *Effect of TiO2 promotion on the structure and performance of silica-supported cobalt-based catalysts for Fischer–Tropsch synthesis.* Journal of Molecular Catalysis A: Chemical, 2014. **390**: p. 52-62.
109. Liu, Y., et al., *Fischer-Tropsch Synthesis over Alumina- Supported Cobalt-Based Catalysts: Effect of Support Variables.* Journal of Materials Science and Chemical Engineering, 2014. **02**(12): p. 19-27.
110. Rytter, E., Holmen, Anders, *Deactivation and Regeneration of Commercial Type Fischer-Tropsch Co-Catalysts—A Mini-Review*, in *Catalysts*. 2015.
111. de la Osa, A.R., et al., *Influence of the catalytic support on the industrial Fischer–Tropsch synthetic diesel production.* Catalysis Today, 2011. **176**(1): p. 298-302.
112. Tasfy, S.F.H., N.A.M. Zabidi, and D. Subbarao, *Comparison of synthesis techniques for supported iron nanocatalysts.* Journal of Applied Sciences, 2011. **11**: p. 1150-1156.
113. van Steen, E. and F.F. Prinsloo, *Comparison of preparation methods for carbon nanotubes supported iron Fischer–Tropsch catalysts.* Catalysis Today, 2002. **71**(3): p. 327-334.
114. Kang, S.-H., et al., *Effect of preparation method of Fe–based Fischer–Tropsch catalyst on their light olefin production.* Catalysis letters, 2009. **130**(3-4): p. 630-636.
115. Branch, S. and S.Z. Oil, *Fisher-Tropsch Synthesis on Alumina Supported Iron-Nickel Catalysts: Effect of Preparation Methods.* 2011.
116. Sarkari, M., et al., *Fisher-Tropsch synthesis on alumina supported iron-nickel catalysts: Effect of preparation methods.* Chemical and Biochemical Engineering Quarterly, 2011. **25**(3): p. 289-297.
117. Nazari, M., et al., *Synthesis and characterization of maghemite nanopowders by chemical precipitation method.* Journal of Nanostructure in Chemistry, 2014. **4**(2): p. 1-5.
118. Abbaslou, R.M.M., A. Tavasoli, and A.K. Dalai, *Effect of pre-treatment on physico-chemical properties and stability of carbon nanotubes supported iron Fischer–Tropsch catalysts.* Applied Catalysis A: General, 2009. **355**(1): p. 33-41.
119. O'Brien, R.J., et al., *Activation Study of Precipitated Iron Fischer− Tropsch Catalysts.* Energy & Fuels, 1996. **10**(4): p. 921-926.
120. Aldossary, M.A.M., *Structure and reactivity of iron-based catalysis for Fischer-Tropsch synthesis.* 2015.
121. Ding, M., et al., *Effect of reducing agents on microstructure and catalytic performance of precipitated iron-manganese catalyst for Fischer–Tropsch synthesis.* Fuel processing technology, 2011. **92**(12): p. 2353-2359.
122. Abbasi, A., M. Ghasemi, and S. Sadighi, *Effect of Lanthanum as a Promoter on Fe-Co/SiO2 Catalyst for Fischer-Tropsch Synthesis.* Bulletin of Chemical Reaction Engineering & Catalysis, 2014. **9**(1): p. 23-27.
123. Aliahmad, M. and N. Nasiri Moghaddam, *Synthesis of maghemite (γ-Fe2O3) nanoparticles by thermal-decomposition of magnetite (Fe3O4) nanoparticles.* Materials Science-Poland, 2013. **31**(2): p. 264-268.
124. Zhang, X., et al., *Structural evolution and characteristics of the phase transformations between α-Fe 2 O 3, Fe 3 O 4 and γ-Fe 2 O 3 nanoparticles under reducing and oxidizing atmospheres.* CrystEngComm, 2013. **15**(40): p. 8166-8172.
125. Liu, S., et al., *Selective synthesis of Fe 3 O 4, γ-Fe 2 O 3, and α-Fe 2 O 3 using cellulose-based composites as precursors.* RSC Advances, 2016. **6**(3): p. 2135-2140.

126. Wu, W., et al., *One-pot reaction and subsequent annealing to synthesis hollow spherical magnetite and maghemite nanocages.* Nanoscale research letters, 2009. **4**(8): p. 926.
127. Dar, M.I. and S. Shivashankar, *Single crystalline magnetite, maghemite, and hematite nanoparticles with rich coercivity.* RSC Advances, 2014. **4**(8): p. 4105-4113.
128. Yun, S., Y.-C. Lee, and H.S. Park, *Phase-controlled iron oxide nanobox deposited on hierarchically structured graphene networks for lithium ion storage and photocatalysis.* Scientific reports, 2016. **6**.
129. Maiti, D., et al., *Phase evolution and growth of iron oxide nanoparticles: Effect of hydrazine addition during sonication.* Crystal Growth & Design, 2013. **13**(8): p. 3637-3644.
130. Feyzi, M., L. Norouzi, and H.R. Rafiee, *Kinetic Study on the CsXH3− X PW12O40/Fe-SiO2 Nanocatalyst for Biodiesel Production.* The Scientific World Journal, 2013. **2013**.
131. Hnilica, J., V. Kudrle, and O. Jašek, *Electrode-less plasma jet synthesis of core-shell iron/iron oxide nanoparticles.* 2013.
132. Xu, Z., J. Yu, and W. Xiao, *Microemulsion-Assisted Preparation of a Mesoporous Ferrihydrite/SiO2 Composite for the Efficient Removal of Formaldehyde from Air.* Chemistry–A European Journal, 2013. **19**(29): p. 9592-9598.
133. Zhou, J., et al., *Effects of oxidation and abnormal grain growth on the magnetic properties of thin Fe-SiO~ 2 granular films.* Journal of applied physics, 1999. **85**(8): p. 6151.
134. Jollet, V., et al., *Confinement of a bioinspired nonheme Fe (II) complex in 2D hexagonal mesoporous silica with metal site isolation.* Dalton Transactions, 2013. **42**(32): p. 11607-11613.
135. Yamashita, T. and P. Hayes, *Analysis of XPS spectra of Fe 2+ and Fe 3+ ions in oxide materials.* Applied Surface Science, 2008. **254**(8): p. 2441-2449.
136. Gunawan, P., et al., *One-dimensional fossil-like γ-Fe2O3@ carbon nanostructure: preparation, structural characterization and application as adsorbent for fast and selective recovery of gold ions from aqueous solution.* Nanotechnology, 2016. **27**(41): p. 415701.
137. Sun, W., et al., *Highly efficient catalytic reduction of bromate in water over a quasi-monodisperse, superparamagnetic Pd/Fe 3 O 4 catalyst.* Journal of Materials Chemistry A, 2013. **1**(32): p. 9215-9224.
138. Chen, L., et al., *Enhanced visible photocatalytic activity of hybrid Pt/α-Fe 2 O 3 nanorods.* RSC Advances, 2012. **2**(26): p. 10057-10063.
139. Wang, J., et al., *α-Fe 2 O 3 quantum dots: low-cost synthesis and photocatalytic oxygen evolution capabilities.* RSC Advances, 2016. **6**(47): p. 41060-41066.
140. Liu, Z., et al., *Monodisperse magnetic ion imprinted polymeric microparticles prepared by RAFT polymerization based on γ-Fe 2 O 3@ meso-SiO 2 nanospheres for selective solid-phase extraction of Cu (ii) in water samples.* RSC Advances, 2015. **5**(65): p. 52369-52381.
141. Maciel, J., et al., *Magnetic nanoparticles coated with polyaniline to stabilize immobilized trypsin.* Hyperfine Interactions, 2016. **237**(1): p. 1-13.
142. Trotte, N.S., M.T. Aben-Athar, and N.M. Carvalho, *Yerba Mate Tea Extract: a Green Approach for the Synthesis of Silica Supported Iron Nanoparticles for Dye Degradation.* Journal of the Brazilian Chemical Society, 2016. **27**(11): p. 2093-2104.
143. de Smit, E. and B.M. Weckhuysen, *The renaissance of iron-based Fischer-Tropsch synthesis: on the multifaceted catalyst deactivation behaviour.* Chem Soc Rev, 2008. **37**(12): p. 2758-81.
144. Aluha, J. and N. Abatzoglou, *Synthetic fuels from 3-φ Fischer-Tropsch synthesis using syngas feed and novel nanometric catalysts synthesised by plasma.* Biomass and Bioenergy, 2016.
145. Ali, S., N.A.M. Zabidi, and D. Subbarao, *Correlation between Fischer-Tropsch catalytic activity and composition of catalysts.* Chemistry Central Journal, 2011. **5**(1): p. 1-8.
146. Wan, H.-J., et al., *Study of an iron-based Fischer–Tropsch synthesis catalyst incorporated with SiO 2.* Journal of Molecular Catalysis A: Chemical, 2006. **260**(1): p. 255-263.

147. Pendyala, V.R.R., et al., *Fischer–Tropsch Synthesis: Morphology, Phase Transformation, and Carbon-Layer Growth of Iron-Based Catalysts.* ChemCatChem, 2014. **6**(7): p. 1952-1960.
148. Hayakawa, H., H. Tanaka, and K. Fujimoto, *Preparation of a new precipitated iron catalyst for Fischer–Tropsch synthesis.* Catalysis Communications, 2007. **8**(11): p. 1820-1824.
149. Pour, A.N., et al., *Fischer-Tropsch synthesis by nano-structured iron catalyst.* Journal of Natural Gas Chemistry, 2010. **19**(3): p. 284-292.
150. Luo, M. and B.H. Davis, *Fischer–Tropsch synthesis: activation of low-alpha potassium promoted iron catalysts.* Fuel processing technology, 2003. **83**(1): p. 49-65.
151. Chen, W., et al., *Effect of confinement in carbon nanotubes on the activity of Fischer− Tropsch iron catalyst.* Journal of the American Chemical Society, 2008. **130**(29): p. 9414-9419.
152. Yan, Q., et al., *Synthesis of aromatic-rich gasoline-range hydrocarbons from biomass-derived syngas over a Pd-promoted Fe/HZSM-5 catalyst.* Energy & Fuels, 2014. **28**(3): p. 2027-2034.
153. Sartipi, S., et al., *Catalysis engineering of bifunctional solids for the one-step synthesis of liquid fuels from syngas: a review.* Catalysis Science & Technology, 2014. **4**(4): p. 893-907.
154. Popok, E.V., et al., *Ultradispersed Electro-explosive Iron Powders as Catalysts for Synthesis of Liquid Hydrocarbons of CO and H2.* Procedia Chemistry, 2015. **15**: p. 225-230.
155. Qian, W., et al., *Activation Temperature Study of Precipitated Fe/SiO2 Catalyst for Fischer-Tropsch Synthesis.* Asian Journal of Chemistry, 2014. **26**(3): p. 869.
156. Liu, R.-J., et al., *Factors influencing the Fischer–Tropsch synthesis performance of iron-based catalyst: Iron oxide dispersion, distribution and reducibility.* Fuel Processing Technology, 2015. **139**: p. 25-32.
157. Alayat, A., D. Mcllroy, and A.G. McDonald, *Effect of synthesis and activation methods on the catalytic properties of silica nanospring (NS)-supported iron catalyst for Fischer-Tropsch synthesis.* Fuel Processing Technology, 2018. **169**: p. 132-141.
158. Cui, X., et al., *Effect of pretreatment on precipitated Fe–Mo Fischer–Tropsch catalysts: Morphology, carburization, and catalytic performance.* Journal of catalysis, 2011. **282**(1): p. 35-46.
159. de Smit, E. and B.M. Weckhuysen, *The renaissance of iron-based Fischer–Tropsch synthesis: on the multifaceted catalyst deactivation behaviour.* Chemical Society Reviews, 2008. **37**(12): p. 2758-2781.
160. Fraser, I., A.M. Rabiu, and E. van Steen, *Investigating the Stability of Ru-promoted Fe-based Fischer-tropsch Catalyst at high Synthesis Gas Conversion.* Energy Procedia, 2016. **100**: p. 210-216.
161. Feyzi, M., L. Norouzi, and Y. Zamani, *Preparation and Characterization of Fe–Co/SiO2 Nanocatalysts for Gasoline Range Hydrocarbons Production from Syngas.* Catalysis Letters, 2016. **146**(10): p. 1922-1933.
162. Ma, X., et al., *Effects of promoters on catalytic performance of Fe-Co/SiO2 catalyst for Fischer-Tropsch synthesis.* Journal of Natural Gas Chemistry, 2009. **18**(3): p. 354-358.
163. Liu, K., et al., *An active Fischer–Tropsch synthesis FeMo/SiO 2 catalyst prepared by a modified sol–gel technique.* Catalysis Communications, 2010. **12**(2): p. 137-141.
164. Wan, H., et al., *Promotional effects of Cu and K on precipitated iron-based catalysts for Fischer–Tropsch synthesis.* Journal of Molecular Catalysis A: Chemical, 2008. **283**(1): p. 33-42.
165. Tasfy, S.F.H., N.A. Mohd Zabidi, and D. Subbarao. *Effects of Cu and K Promoters on the Catalytic Performance of Iron-Based Nanocatalyst for Fischer-Tropsch Synthesis*. in *Advanced Materials Research*. 2014. Trans Tech Publ.
166. Bukur, D.B., D. Mukesh, and S.A. Patel, *Promoter effects on precipitated iron catalysts for Fischer-Tropsch synthesis.* Industrial & engineering chemistry research, 1990. **29**(2): p. 194-204.

167. Housaindokht, M.R. and A. Nakhaei Pour, *Size Control of Iron Oxide Nanoparticles Using Reverse Microemulsion Method: Morphology, Reduction, and Catalytic Activity in CO Hydrogenation.* Journal of Chemistry, 2013. **2013**.
168. Donner, J.T., *Xps Characterization of Supported Iron/Ruthenium Carbon Monoxide Hydrogenation Catalyst Systems.* 1983.
169. Jena, A. and K. Gupta, *A novel technique for surface area and particle size determination of components of fuel cells and batteries.* Porous Materials, Inc. Cornell Business & Technology Park, 2000. **83**.
170. Li, S., et al., *Effects of Zn, Cu, and K promoters on the structure and on the reduction, carburization, and catalytic behavior of iron-based Fischer–Tropsch synthesis catalysts.* Catalysis Letters, 2001. **77**(4): p. 197-205.
171. Laitao, L., et al., *Studies on the surface behavior of non-chromium type high temperature CO shift catalysts.* Reaction Kinetics and Catalysis Letters, 1998. **65**(1): p. 199-205.
172. Belhekar, A.A., S. Ayyappan, and A.V. Ramaswamy, *FT-IR studies on the evolution of different phases and their interaction in ferric molybdate—molybdenum trioxide catalysts.* Journal of Chemical Technology and Biotechnology, 1994. **59**(4): p. 395-402.
173. Shinde, S.K., et al., *Influence of Mn incorporation on the supercapacitive properties of hybrid CuO/Cu (OH) 2 electrodes.* RSC Advances, 2015. **5**(39): p. 30478-30484.
174. Shi, L., et al., *CH 3-modified Co/Ru/SiO 2 catalysts and the performances for Fischer–Tropsch synthesis.* Fuel, 2008. **87**(4): p. 521-526.
175. Li, W., et al., *Efficient Ru–Fe catalyzed selective hydrogenolysis of carboxylic acids to alcoholic chemicals.* RSC Advances, 2014. **4**(55): p. 29072-29082.
176. Veerakumar, P., A. Ramdass, and S. Rajagopal, *Ruthenium nanocatalysis on redox reactions.* Journal of nanoscience and nanotechnology, 2013. **13**(7): p. 4761-4786.
177. Manaenkov, O.V., et al., *Ru-containing magnetically recoverable catalysts: A sustainable pathway from cellulose to ethylene and propylene glycols.* ACS applied materials & interfaces, 2016. **8**(33): p. 21285-21293.
178. Qin, S., et al., *Effect of Mo addition on precipitated Fe catalysts for Fischer–Tropsch synthesis.* Journal of Molecular Catalysis A: Chemical, 2009. **304**(1): p. 128-134.
179. Qin, S., et al., *Fe–Mo interactions and their influence on Fischer–Tropsch synthesis performance.* Applied Catalysis A: General, 2011. **392**(1): p. 118-126.
180. Yang, W., et al., *MoO 3 nanorods/Fe 2 (MoO 4) 3 nanoparticles composite anode for solid oxide fuel cells.* international journal of hydrogen energy, 2014. **39**(26): p. 14411-14415.
181. YU, Y., et al., *Synthesis, Structure and Characterization of Three Metal Molybdate Hydrates: Fe (H 2 O) 2 (MoO 4) 2· H 3 O, NaCo 2 (MoO 4) 2 (H 3 O 2) and Mn 2 (MoO 4) 3· 2 H 3 O.* CHEMICAL RESEARCH IN CHINESE UNIVERSITES, 2012. **28**(2): p. 186-190.
182. Zhou, Q., et al., *Deep oxidative desulfurization of model oil catalyzed by magnetic MoO 3/Fe 3 O 4.* RSC Advances, 2015. **5**(85): p. 69388-69393.
183. Bowker, M., et al., *Evolution of active catalysts for the selective oxidative dehydrogenation of methanol on Fe 2 O 3 surface doped with Mo oxide.* Physical Chemistry Chemical Physics, 2013. **15**(29): p. 12056-12067.
184. Kondamudi, K., K.K. Pant, and S. Upadhyayula, *Synergistic Effect of Fe–Co Bimetallic Catalyst on FTS and WGS Activity in the Fischer–Tropsch Process: A Kinetic Study.* Industrial & Engineering Chemistry Research, 2017. **56**(16): p. 4659-4671.
185. Sun, C., et al., *Effect of preparation method on performance of Cu–Fe/SiO 2 catalysts for higher alcohols synthesis from syngas.* RSC Advances, 2016. **6**(60): p. 55233-55239.

186. Lu, Y., et al., *Fischer–Tropsch synthesis of olefin-rich liquid hydrocarbons from biomass-derived syngas over carbon-encapsulated iron carbide/iron nanoparticles catalyst.* Fuel, 2017. **193**: p. 369-384.
187. Zheng, J., et al., *Investigation of the highly tunable selectivity to linear α-olefins in Fischer–Tropsch synthesis over silica-supported Co and CoMn catalysts by carburization–reduction pretreatment.* Catalysis Science & Technology, 2017. **7**(20): p. 4736-4755.
188. Gupta, R., et al., *Highly Sensitive Detection of Arsenite Based on Its Affinity toward Ruthenium Nanoparticles Decorated on Glassy Carbon Electrode.* Analytical chemistry, 2016. **88**(4): p. 2459-2465.
189. Hu, L., et al., *Highly efficient degradation of high-loaded phenol over Ru–Cu/Al 2 O 3 catalyst at mild conditions.* RSC Advances, 2017. **7**(35): p. 21507-21517.
190. Basinska, A., et al., *Activity of Ru/Fe2O3 Catalysts in the Process of NO Reduction with Propane* Corresponding author.* Polish Journal of Environmental Studies, 2003. **12**(2).
191. Ye, T.-N., et al., *Electronic interactions between a stable electride and a nano-alloy control the chemoselective reduction reaction.* Chemical Science, 2016. **7**(9): p. 5969-5975.
192. SUZUKI, T. and S. TAJIMA, *Enhancement of Fischer-Tropsch Reaction on Silica Supported Cobalt Catalyst.* Transactions of the Materials Research Society of Japan, 2010. **35**(3): p. 635-638.
193. Romar, H., et al., *H2-TPR, XPS and TEM Study of the Reduction of Ru and Re promoted Co/γ-Al2O3, Co/TiO2 and Co/SiC Catalysts.* Journal of Materials Science Research, 2016. **5**(2): p. 39.
194. Kangvansura, P., et al., *Effects of Potassium and Manganese Promoters on Nitrogen-Doped Carbon Nanotube-Supported Iron Catalysts for CO2 Hydrogenation.* Engineering, 2017. **3**(3): p. 385-392.

APPENDICES

Appendix A. Facilities and Equipment -Catalyst preparation, characterization and testing

BET analyzer for measuring surface area

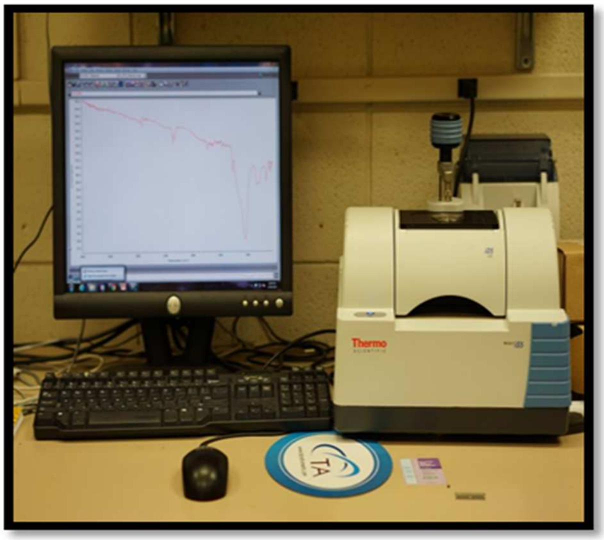

FT-IR for identifying organic materials

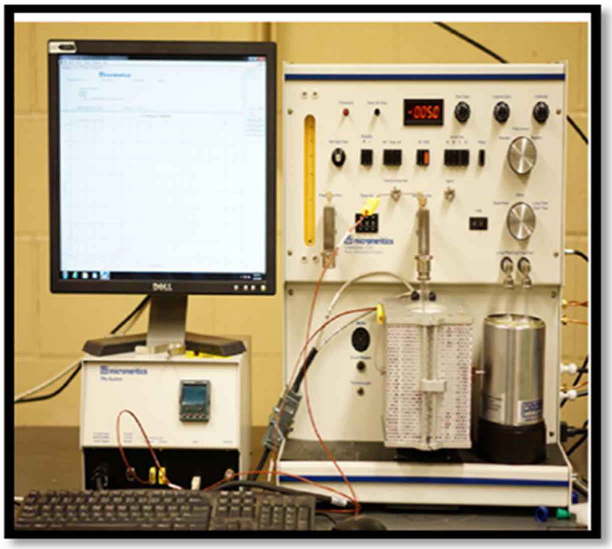

TRP for tasting reduction temperature

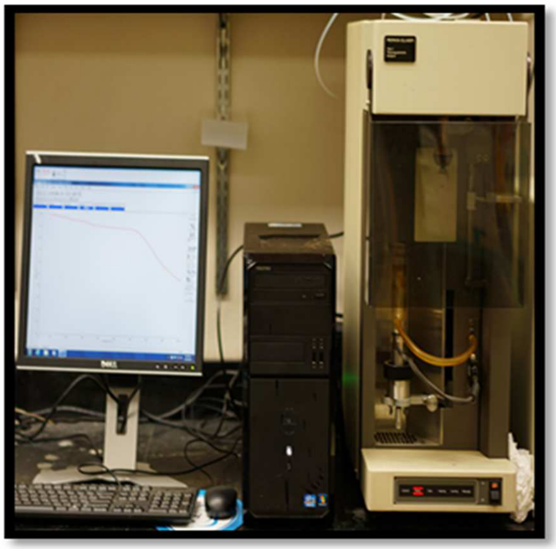

TGA for measuring thermal stability

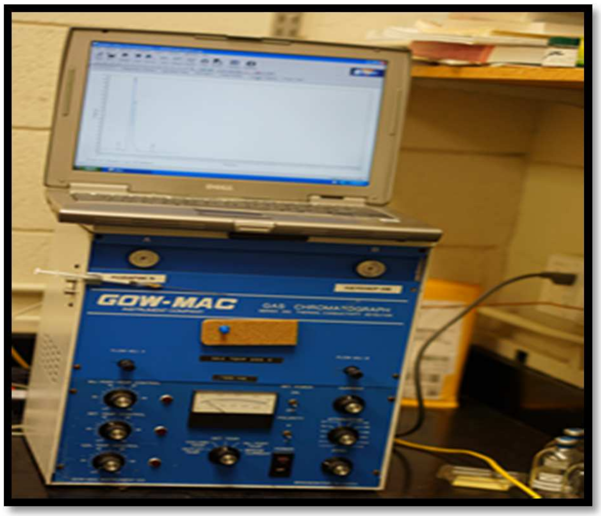

GC-TCD for identifying gaseous product

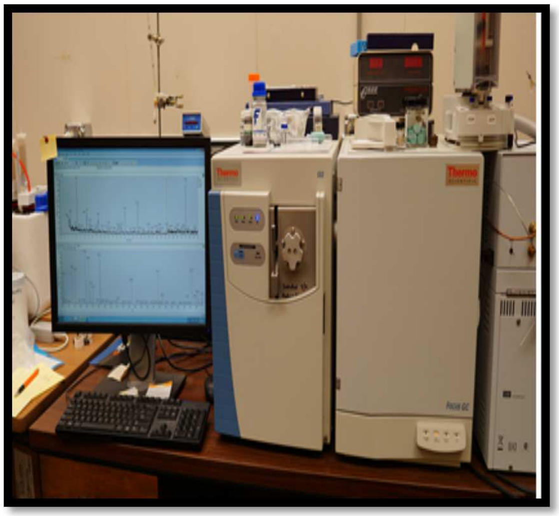

GC-MS for identifying liquid product

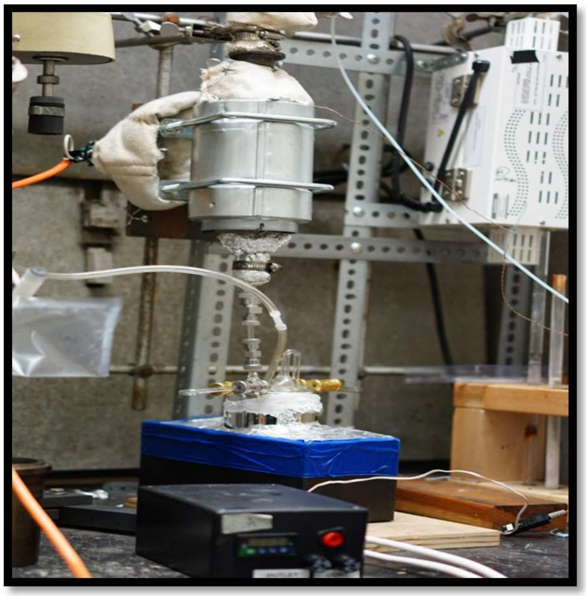

FTS reaction facilities

Appendix B. Publications, oral presentations and posters derived from this dissertation

Publications

1. Kengne, Blaise-Alexis Fouetio; **Alayat, Abdulbaset** M.; Luo, Guanqun; McDonald, Armando G.; Brown, Justin; Smotherman, Hayden; McIlroy, David N, *Preparation, surface characterization and performance of a Fischer-Tropsch catalyst of cobalt supported on silica nanosprings*. Applied Surface Science, 2015. 359: p. 508-514.
2. **Alayat, Abdulbaset** M., McIlroy, David N, and ; McDonald, Armando G, *Effect of synthesis and activation methods on the catalytic properties of silica nanospring (NS)-supported iron catalyst for Fischer-Tropsch synthesis*. Fuel Processing Technology, 2018. 169: p. 132-141.
3. **Alayat, Abdulbaset** M., McIlroy, David N, and ; McDonald, Armando G, Enhancement of the catalytic performance of silica nanosprings (NS)-supported iron catalyst with copper, molybdenum, cobalt and ruthenium promoters for Fischer-Tropsch synthesis. Fuel Processing Technology, 2018.
4. **Alayat, Abdulbaset** M., McIlroy, David N, and; McDonald, Armando G, *Characterization and catalytic Behavior of EDTA modified silica nanosprings (NS)-supported cobalt catalyst for Fischer-Tropsch synthesis.* (Will be submitted).

Oral presentations

1. **Alayat, Abdulbaset** M., McDonald A. G., and Mcllroy D. N., Activation Iron Nanospring Catalyst by H_2, CO and H_2/CO for Biofuel Production Via the Fischer -Tropsch Synthesis, (WSU,UI and OSU) Local Convention 2016 Annual Meeting, Pullman, Washington State University, USA, May 22-23, 2016.
2. **Alayat, Abdulbaset** M., McDonald A. G., and Mcllroy D. N., Effect of Preparation Methods on Catalytic Performance of Silica Nanospring-Supported Fischer-Tropsch Catalysts for Biofuel Production, 70st FPS International Convention 2016 Annual Meeting, Portland, Oregon, USA, June 27-29, 2016.
3. **Alayat, Abdulbaset** M., McDonald A. G., and Mcllroy D. N., Effect of Ruthenium Promoter on Silica Nanosprings (SN)-Supported Iron Catalyst for Fischer-Tropsch Synthesis, (WSU,UI and OSU) Local Convention 2017

Annual Meeting, Corvallis, Oregon State University, USA, October 22-23, 2017.

Posters

1. **Alayat, Abdulbaset M.,** McDonald A. G., and Mcllroy D. N., Enhancement of the Fischer-Tropsch synthesis catalytic performance of iron catalyst with copper, molybdenum, cobalt and ruthenium promoters on silica nanosprings (NS) support. Materials Research Society. Spring meeting &Exhibit, Phoenix, Arizona State, USA, April 2-6, 2018.